

Fabrication, Characterization, and Functionalization of Porous  
Nanocrystalline Silicon Membranes

by

David Z. Fang

In Partial Fulfillment of the Requirements

for the Degree of

Doctor of Philosophy

Supervised by

Professor Philippe M. Fauchet

Department of Electrical and Computer Engineering

Arts, Sciences and Engineering

Edmund A. Hajim School of Engineering and Applied Sciences

University of Rochester

Rochester, NY

2010

# Curriculum Vitae

The author was born in Guangzhou, China on October 17, 1983. He attended the University of Rochester and received his Bachelor of Science with high distinction in Electrical and Computer Engineering in 2005 and his Master of Science in Electrical Engineering in 2006 under the direction of Professor Philippe M. Fauchet. The author's research interests include the study of nanostructured materials and their applications.

# Acknowledgements

I am deeply indebted to my advisor, Philippe Fauchet, who has given me the encouragement and guidance to complete this work. Many thanks to Chris Striemer for mentoring me and for discovering this revolutionary material. A special thanks to James McGrath for all the work he has done in leading our group and making the day-to-day operations run smoothly. I am grateful to everyone in the Nanomembrane Research Group and Fauchet Group, for sharing their knowledge and keeping me sane. It has been a pleasure to work with everyone at SiMPore, Inc. I consider myself fortunate to not only work with the best people in academia, but also some of the brightest minds from industry. I am grateful to my committee members, Professors Mark Bocko and Thomas Hsiang, for their review of this thesis. This work would not have been possible without the assistance of the University staff; many thanks to Paul Osborne, Vicki Heberling, Audrey Pierce, Barbara Dick, Nancy Gronski, Brian McIntyre, and Karen Bentley. Thank you Professor Thomas Jones for overseeing the Hopeman Microfabrication Facility, where much of this work was performed. This work was completed with financial support from the National Institutes of Health (R21EB006149; R21EB007480), NYSTAR (TTIP C020040), ARO (DAAD19-03-1-0267), and the National Science Foundation (DMR0722653; ECCS 0707795).

Finally, I would not be here without the love and support of my family. I attribute my curiosity for science and engineering to the LEGO sets I received on my birthdays. Thank you for everything you have given me.

# Abstract

Porous nanocrystalline silicon (pnc-Si) membranes are promising for a wide range of applications from biofiltration to use as a platform for cell culture. It is an order of magnitude thinner than any commercially available or experimentally fabricated membrane. Because the thickness of a pnc-Si membrane is between 15 nm and 30 nm, comparable to the size of molecules to be separated, mass transport through the membrane is greatly enhanced. The first part of this work focuses on the fabrication of pnc-Si. For applications involving separation and concentration of molecular species, it is crucial that a membrane passes certain species while rejecting others. One manner in which this can be achieved is by tuning the size and density of the pores by changing key fabrication conditions. These parameters are identified and a systematic study was performed to determine their effect on pore morphology. In the second part of this work, a phenomenological model for pore formation is presented based on empirical observations and prior studies on polycrystalline materials. Next, the structural, optical, and mechanical properties of pnc-Si are examined using an array of characterization tools. In the final part of this thesis, post-production methods for pore size control and functionalization are discussed. It is demonstrated that the hydraulic permeability of pnc-Si, in both the unmodified and modified forms, follows theoretical predications for transport through an ultrathin porous material. Additionally, nanoparticle and protein separations are presented as a demonstration of the potential use of pnc-Si membranes in biomedical research and industry.

## List of Publications and Presentations

D. Z. Fang, C. C. Striemer, T. R. Gaborski, J. L. McGrath and P. M. Fauchet, *Methods for controlling the pore properties of ultra-thin nanocrystalline silicon membranes*, J. Phys. Condens. Mat. **22** (45) (2010).

D. Z. Fang, C. C. Striemer, T. R. Gaborski, J. L. McGrath and P. M. Fauchet, *Pore Size Control of Ultrathin Silicon Membranes by Rapid Thermal Carbonization*, Nano Lett. **10** (10), 3904-3908 (2010).

T. R. Gaborski, J. L. Snyder, C. C. Striemer, D. Z. Fang, M. Hoffman, P. M. Fauchet and J. L. McGrath, *High Performance Separation of Nanoparticles with Ultrathin Porous Nanocrystalline Silicon (pnc-Si) Membranes*, ACS Nano **4** (11). 6973-6981 (2010).

J. L. Snyder, A. Clark Jr., D. Z. Fang, T. R. Gaborski, C. C. Striemer, P. M. Fauchet and J. L. McGrath, *A theoretical and experimental analysis of molecular separations by diffusion through ultrathin nanoporous membranes*, J. Membrane Sci. (In Press).

M. N. Kavalenka, C. C. Striemer, D. Z. Fang, T. R. Gaborski, J. L. McGrath and P. M. Fauchet, *Ballistic and non-ballistic gas flow through ultrathin nanopores*, Phys. Rev. Lett. (In Review).

R. Ishimatsu, J. Kim, P. Jing, C. C. Striemer, D. Z. Fang, P. M. Fauchet, J. L. McGrath and S. Amemiya, *Ion-Selective Permeability of an Ultrathin Nanoporous Silicon Membrane as Probed by Scanning Electrochemical Microscopy Using Micropipet-Supported ITIES Tips*, Anal. Chem. **82** (17), 7127-7134 (2010).

A. A. Agrawal, B. J. Nehilla, K. V. Reisig, T. R. Gaborski, D. Z. Fang, C. C. Striemer, P. M. Fauchet and J. L. McGrath, *Porous nanocrystalline silicon membranes as highly permeable and molecularly thin substrates for cell culture*, *Biomaterials* **31** (20), 5408-5417 (2010).

D. Z. Fang, C. C. Striemer, J. L. McGrath and P. M. Fauchet, *Methods for Controlling the Morphology of Porous Nanocrystalline Silicon Membranes*, presented at the Materials Research Society Spring Meeting, San Francisco, 2010.

D. Z. Fang, C. C. Striemer, J. L. McGrath and P. M. Fauchet, *On Controlling the Morphology of Ultra-thin Porous Nanocrystalline Silicon Membranes*, presented at the Porous Semiconductors Science and Technology, Valencia, 2010.

K. Shome, M. N. Kavalenka, D. Z. Fang and P. M. Fauchet, *Metallized ultrathin porous silicon membranes for biological sensing using SERS*, *Proc. SPIE* **7553** (2010).

M. N. Kavalenka, C. C. Striemer, D. Z. Fang, T. R. Gaborski, J. L. McGrath and P. M. Fauchet, *Experimental Study of Molecule-Pore Wall Collisions in Carbonized Ultrathin Porous Membranes*, presented at Materials Research Society Fall Meeting, Boston, 2010.

E. Kim, H. Xiong, C. C. Striemer, D. Z. Fang, P. M. Fauchet, J. L. McGrath and S. Amemiya, *A Structure-Permeability Relationship of Ultrathin Nanoporous Silicon Membrane: A Comparison with the Nuclear Envelope*, *J. Am. Chem. Soc.* **130** (13), 4230-4231 (2008).

C. C. Striemer, T. R. Gaborski, D. Z. Fang, J. L. Snyder, J. L. McGrath, and P. M. Fauchet, *Porous Ultrathin Silicon for Nanoscale Membrane Applications*, presented at the Materials Research Society Fall Meeting, Boston, 2009.

D. Z. Fang, M. Kavalenka, J.-P. S. DesOrmeaux, L. Miao, C. C. Striemer, J. L. McGrath and P. M. Fauchet, *Fabrication and Characterization of Nanometer-Thick Silicon Membranes*, presented at the Porous Semiconductors Science and Technology, Mallorca, Spain, 2006.

# Table of Contents

Curriculum Vitae .....	ii
Acknowledgements.....	iii
Abstract.....	iv
List of Publications and Presentations .....	v
Table of Contents.....	viii
Table of Figures .....	xii
Foreword.....	1
Chapter 1. Introduction.....	2
1.1 A nano world .....	2
1.2 Membrane technology .....	3
1.2.1 Polymer track etched membranes .....	3
1.2.2 Carbon nanotube membranes.....	4
1.2.3 Solid-state nanopore membranes .....	6
1.3 Porous nanocrystalline silicon membranes.....	7
1.4 Conclusions.....	9
Chapter 2. Fabrication of porous nanocrystalline silicon membranes.....	10
2.1 Introduction.....	10
2.2 Process overview .....	10
2.3 Wafer preparation and patterning .....	12
2.4 Thin film deposition .....	14
2.4.1 Sputtering discharges .....	14
2.4.2 Sputter equipment .....	16
2.4.3 Deposition parameters.....	18



2.5	Formation of pores by rapid thermal annealing.....	19
2.6	Rapid thermal annealing.....	20
2.7	Anisotropic bulk silicon etching.....	22
2.8	Controlling pore morphology .....	25
2.8.1	Annealing temperature.....	25
2.8.2	Soak time.....	27
2.8.3	Annealing with a susceptor .....	29
2.8.4	Annealing ramp rate.....	32
2.8.5	Silicon thickness .....	35
2.8.6	Substrate bias .....	37
2.8.7	Deposition temperature.....	41
2.8.8	Alternative deposition techniques.....	43
2.9	Reproducibility .....	45
2.10	Variations in morphology .....	46
2.11	Membrane defects .....	48
2.11.1	Pinholes.....	48
2.12	Conclusions.....	50
Chapter 3.	Mechanisms of pore formation .....	51
3.1	Introduction.....	51
3.2	Pore formation during silicon crystallization .....	51
3.3	Crystallization of amorphous silicon .....	53
3.3.1	Nucleation and growth.....	53
3.3.2	Thermodynamic quantities.....	55
3.4	Pore formation activation energies .....	58
3.5	Factors influencing nucleation and growth.....	60
3.6	Stages of pore formation.....	65
3.6.1	Pore nucleation.....	65

3.6.2	Pore growth .....	66
3.7	The role of film stress and strain on pore formation .....	68
3.7.1	Crystallization of a free-standing silicon thin film .....	70
3.7.2	Crystallization of a SiO <sub>2</sub> /Si/SiO <sub>2</sub> free-standing membrane .....	71
3.8	Conclusions.....	73
Chapter 4.	Characterization of porous nanocrystalline silicon membranes .....	74
4.1	Introduction.....	74
4.2	Transmission electron microscopy .....	75
4.2.1	Pore size distribution calculations.....	78
4.2.2	Pore size distribution error analysis .....	81
4.3	Optical properties.....	83
4.3.1	Spectroscopic ellipsometry .....	83
4.3.2	Optical constants .....	85
4.3.3	Silicon dioxide .....	86
4.3.4	Nanocrystalline silicon.....	87
4.4	Surface morphology.....	89
4.5	Mechanical properties.....	91
4.5.1	Mechanical properties of thin films .....	91
4.5.2	Pressure-displacement measurements.....	93
4.6	Conclusions.....	100
Chapter 5.	Functionalization of porous nanocrystalline silicon membranes.....	101
5.1	Rapid thermal carbonization.....	101
5.1.1	Introduction .....	101
5.1.2	Carbonization in a rapid thermal processor .....	103
5.1.3	Temperature dependence .....	105
5.1.4	Time dependence .....	107
5.1.5	Self-ordering and x-ray spectroscopy .....	109

5.1.6	Chemical stability .....	110
5.1.7	Hydraulic permeability .....	111
5.1.8	Gold nanoparticle filtration .....	116
5.1.9	Protein filtration .....	118
5.1.10	Conclusions .....	121
5.2	Atomic layer deposition.....	122
5.2.1	Introduction .....	122
5.2.2	Atomic layer deposition of aluminum oxide.....	123
5.2.3	Pore size control using atomic layer deposition of aluminum oxide .	124
5.2.4	Gold nanoparticle filtration .....	127
5.2.5	Conclusions .....	128
5.3	Carbon growth on alumina-coated porous nanocrystalline silicon membranes .....	129
5.3.1	Introduction .....	129
5.3.2	Ordered carbon growth .....	129
5.3.3	Pore size dependent carbon growth on alumina-coated porous nanocrystalline silicon membranes .....	130
5.3.4	Conclusions .....	134
Chapter 6.	Future directions .....	135
6.1	Crystallization and pore formation .....	135
6.2	Porous nanocrystalline silicon for use in fuel cells .....	136
6.3	Multi-stage microfluidic separation systems .....	141
6.4	Conclusions.....	145
References.	.....	146

# Table of Figures

<b>Figure 1-1.</b> Scanning electron microscopy micrograph of a polycarbonate track etched membrane showing overlapping pores [39]. .....	<b>4</b>
<b>Figure 1-2. (a)</b> Vertically aligned carbon nanotubes [30] <b>(b)</b> Carbon nanotubes in a silicon nitride matrix supported by a silicon scaffold [28]. .....	<b>5</b>
<b>Figure 1-3.</b> Hundreds of membrane “chips” can be produced on a single 4-inch silicon wafer. The golden rectangular features are areas of free-standing pnc-Si. ....	<b>7</b>
<b>Figure 1-4.</b> Scanning electron microscopy image of a hanging sheet of pnc-Si demonstrating the material’s molecular thinness. ....	<b>8</b>
<b>Figure 2-1.</b> Process flow for the fabrication of porous nanocrystalline silicon membranes. ....	<b>12</b>
<b>Figure 2-2.</b> Simplified schematic of an rf sputter deposition system. ....	<b>15</b>
<b>Figure 2-3.</b> A planar magnetron configuration. The magnetic field lines are parallel to the target material. Electrons are “trapped” in the magnetic field, which increases ionization near the target surface. ....	<b>15</b>
<b>Figure 2-4.</b> Physical vapor deposition by rf magnetron sputtering using a confocal target arrangement. The substrate is suspended from the rotation stage at the top of the image. The substrate may be heated via tungsten-halogen lamps to temperatures between room temperature and 800°C. ....	<b>16</b>
<b>Figure 2-5.</b> Thickness profile of a silicon dioxide thin film obtained by spectroscopic ellipsometry. The uniformity is $\pm 0.6\%$ . Wafer position ‘0’ refers to the center of a	

4-inch wafer. The dip in the thickness profile is characteristic of magnetron sputtering and is a result of the plasma profile. .... 17

**Figure 2-6.** (a) Bright-field TEM micrograph of a 15 nm thick amorphous silicon membrane. The dark area represents the thick silicon support region and the white area represents the free-standing membrane area. (b) A partially crystallized 15 nm thick silicon film annealed at 700°C. The bright areas indicate through-pores and the dark areas are diffracting Si nanocrystals. Pores form preferentially at the amorphous-crystalline interface. (c) A fully crystallized 15 nm thick silicon film annealed at 1000°C. .... 19

**Figure 2-7.** Optical image in Nomarski mode of a 15 nm amorphous silicon membrane (a) and pnc-Si membrane (b). Both membranes are 200  $\mu\text{m}$  x 200  $\mu\text{m}$ . .... 20

**Figure 2-8.** (a) Schematic of the RTP chamber. The wafer can be placed inside a silicon carbide coated graphite susceptor to improve heating uniformity. (b) Wafer sitting on the quartz RTP tray. Two thermocouples attached to the tray monitor the temperature during the annealing process. .... 21

**Figure 2-9.** A typical temperature profile during the rapid thermal process. The ramp rate and soak temperature is precisely tuned using a PID controller. The first 30 seconds of the process is a purge in argon to flush out residual oxygen in the chamber. The slight temperature increase during this period is due to the warm chamber walls. .... 22

**Figure 2-10.** A trapezoidal cross-section results after bulk silicon micro-machining due to the anisotropic etch. .... 23

**Figure 2-11. (a)** Concept drawing of a custom-made silicon wet-etch cell. The wafer is sealed between the bottom glass disk and main etch cell body with an o-ring. **(b)** The fluid tight seal is made with four toggle clamps. A thermocouple submerged in the etchant monitors the temperature close to the wafer surface. A tube condenser captures any hazardous vapor. A quick drain allows for quick disposal of the etchant. **(c)** End point detection is achieved by illuminating the stir table. The light is transmitted through the released membrane and seen through a viewing window at the top of the etch cell..... **24**

**Figure 2-12.** Silicon micromachining techniques allow for different patterns to be transferred and etched into wafers resulting in various membrane geometries. Shown above are three membrane patterns that have been etched into 4-inch silicon wafers..... **25**

**Figure 2-13. (a) – (f)** TEM micrographs of 15 nm thick pnc-Si membranes annealed at 800°C, 850°C, 925°C, 950°C, 1000°C, and 1100°C. **(g)** The pore size distributions were calculated directly from TEM micrographs. **(h)** The average pore diameter and porosity is plotted for each annealing temperature. .... **27**

**Figure 2-14. (a)** Pore size distributions of 15 nm thick pnc-Si membranes annealed at 1000°C with a ramp rate of 100°C/s for 10, 60, and 300 s. **(b)** A plot of the average diameter and porosity of the membranes annealed for various times. Note the time scale is logarithmic. .... **28**

**Figure 2-15.** Cartoon showing Si atoms and a single pore for **(a)** short, **(b)** medium, **(c)** and long anneal durations. The population of amorphous silicon (disordered) decreases with time, while the nanocrystalline fraction (ordered) increases with

longer anneal times. As a consequence of increased crystallization, pore size increases..... **29**

**Figure 2-16.** 15 nm thick pnc-Si membrane deposited with 25 W of applied substrate bias annealed at 1000°C with a ramp rate of 50°C/s **(a)** using a susceptor and **(b)** without a susceptor. **(c)** The pore size distributions show that the density of pores greatly increases when membranes were annealed outside the susceptor..... **31**

**Figure 2-17.** Density of pores as a result of annealing at different temperatures with and without the susceptor. .... **31**

**Figure 2-18 (a)** A 15 nm thick pnc-Si membrane annealed at 1000°C with a ramp rate of 10°C/s **(b)** 50°C/s and **(c)** 100°C/s. **(d)** The pore size distribution becomes increasingly narrow at higher ramp rates..... **33**

**Figure 2-19 (a)** A 30 nm thick pnc-Si membrane annealed at 1000°C with a ramp rate of 10°C/s and **(b)** 100°C/s..... **33**

**Figure 2-20.** Plot showing three different simulated ramp rates (10°C/s, 50°C/s, 100°C/s). The cartoon insets show pores and nanocrystals in films annealed at low and high ramp rates. The purple and gray regions represent the nanocrystalline and amorphous phase, respectively. .... **34**

**Figure 2-21. (a) – (d)** TEM micrographs of 30 nm thick pnc-Si membranes that were annealed at 1000°C, 1050°C, 1100°C, and 1150°C. **(e)** The pore size distributions were calculated directly from TEM micrographs. **(f)** The average pore diameter and porosity is plotted for each annealing temperature..... **36**

**Figure 2-22. (a)** A TEM micrograph of a 9 nm thick pnc-Si membrane. No through pores are identifiable at this resolution. The small white features are crystalline

diffraction features. **(b)** A 15 nm thick pnc-Si membrane showing clearly defined through pores. **(c)** A 50 nm thick pnc-Si membrane exhibits larger pores at a lower density..... **37**

**Figure 2-23.** Pore size histogram and TEM micrographs of pnc-Si membranes deposited with various substrate biases. All membranes are 15 nm thick and annealed at 1000°C with a ramp rate of 100°C/s for 60 s. .... **38**

**Figure 2-24.** **(a)** Average pore diameter, **(b)** porosity, and **(c)** pore density of a 15 nm thick pnc-Si membrane deposited at various substrate biases and annealed at 1000°C with a ramp rate of 100°C/s for 60 s. .... **39**

**Figure 2-25.** Plots comparing the average diameter, porosity, and density of pores of pnc-Si membranes deposited with a substrate bias of 5 and 25 W versus annealing temperature. .... **40**

**Figure 2-26.** Average diameter and porosity of a 15 nm-thick pnc-Si membrane deposited at various temperatures and 25 W substrate bias. The membranes were all annealed at 1000°C with a ramp rate of 100°C/s. .... **42**

**Figure 2-27.** Index of refraction of amorphous silicon films deposited at different temperatures as measured by spectroscopic ellipsometry. .... **42**

**Figure 2-28.** Extinction coefficient amorphous silicon films deposited at different temperatures as measured by spectroscopic ellipsometry. .... **43**

**Figure 2-29.** **(a)** TEM micrograph of a PECVD deposited membrane film and a **(b)** PVD deposited 15 nm membrane film. .... **44**



- Figure 2-30.** Index of refraction and extinction coefficient versus photon energy of a PVD and PECVD deposited amorphous silicon film. Some energies were truncated in the PECVD measurement due to anomalous absorption in the infrared. .... **45**
- Figure 2-31.** Pore statistics of seven wafers that were processed identically. The standard deviation of the average diameter and porosity are 0.6 nm and 0.8%, respectively. .... **46**
- Figure 2-32.** (a) The average diameter and (b) porosity of pnc-Si membranes from nine different positions on a 4-inch wafer. (c) A pore size histogram comparing the maximum and minimum points on the wafer. .... **47**
- Figure 2-33.** (a) Bright-field optical image of a pnc-Si membrane with a high density of pinhole defects (black spots). (b) TEM image of a single pinhole defect. The small white dots in the gray background are nanopores. .... **49**
- Figure 2-34.** Dark field optical image of a film with a high density of particle contaminants. The particles act as scatterers, which appear as bright dots in the dark field imaging mode. .... **50**
- Figure 3-1.** High-resolution TEM image of a nanopore with an adjacent nanocrystal. The lattice spacing was measured to be 3.1 Å, consistent with a <111> oriented crystal. .... **52**
- Figure 3-2.** Nanocrystal growth occurs in a step-wise manner [80]. Si atoms migrate to form “kinks” (CD) and growth proceeds along the  $[\bar{1}00]$  direction indicated by the arrows. The nanocrystalline silicon facets are defined by the slowest growth direction, [111]. .... **54**

- Figure 3-3. (a)** A schematic depicting microtwin growth. Further nanocrystal growth can nucleate along the microtwin ledge with the addition of two atom clusters [81].
- (b)** TEM micrograph showing pores adjacent to Si nanocrystals and microtwin defects. .... **55**
- Figure 3-4.** Arrhenius plot of the growth rate of silicon crystallization [80]. .... **57**
- Figure 3-5.** Arrhenius plot of the pore nucleation rate,  $J_p$  for a 15 nm and 30 nm thick pnc-Si membrane. The activation energy for pore nucleation is calculated using Equation 3-4. The 15 nm membrane has a pore nucleation activation energy of 0.55 eV and the 30 nm membrane has an activation energy of 0.69 eV. .... **59**
- Figure 3-6.** Arrhenius plot of the pore growth rate,  $k_p$  for a 15 nm and 30 nm thick pnc-Si membrane. The activation energy for pore growth is calculated using Equation 3-4. The 15 nm membrane has a pore growth activation energy of 0.28 eV and the 30 nm membrane has an activation energy of 0.29 eV. .... **60**
- Figure 3-7.** Cartoon depiction of the SiO<sub>2</sub>-Si interface with different substrate bias powers during the silicon deposition and the associated TEM micrographs. **(a) - (b)** 0 W, **(c) - (d)** 5 W, and **(e) - (f)** 50 W. The red dots indicate the location of nanocrystal nucleation sites. .... **63**
- Figure 3-8.** Atomic force microscopy scans of a bare wafer and three amorphous silicon films deposited with different amounts of substrate bias. .... **64**
- Figure 3-9.** Simplified schematic of pore nucleation. The green and blue balls represent silicon and oxygen clusters, respectively. **(a)** Nanocrystal nucleation occurs at the Si/SiO<sub>2</sub> interface. **(b)** As the nanocrystal grows in size, Si atoms leave vacancies that become voids. **(c)** Voids that penetrate the film thickness become pores. .... **66**

- Figure 3-10.** TEM micrograph showing a pore at the amorphous-nanocrystalline interface. Pores nucleate and grow as atoms in the amorphous phase become mobile and are converted into nanocrystals..... **68**
- Figure 3-11.** Process flow showing the rapid thermal anneal of two free-standing membrane structures: one with protective oxide and one without protective oxide. .... **69**
- Figure 3-12.** TEM micrographs of 15 nm and 30 nm thick silicon membranes annealed at various temperatures..... **70**
- Figure 3-13.** TEM micrographs of 15 nm and 30 nm thick silicon membranes annealed with 20 nm of surrounding protective oxide at various temperatures. .... **72**
- Figure 4-1.** High-resolution TEM image showing a pore surrounded by nanocrystals of different orientation. The  $\langle 110 \rangle$  oriented Si nanocrystal has an atomic spacing of 1.9 Å. The  $\langle 111 \rangle$  oriented nanocrystal has an atomic plane spacing of 3.1 Å. The spacing was calculated from the TEM micrograph by averaging the distance between several atoms or planes..... **77**
- Figure 4-2.** (a) A threshold algorithm is applied to the TEM image to create a binary image. (b) Pores are identified and (c) a size distribution calculated. A Weibull probability density fit is applied to the histogram (blue dashed line)..... **79**
- Figure 4-3.** A light wave will change its polarization state after it reflects off the surface of a thin film. An ellipsometer measures this change and extracts thickness and optical constant information from it. [94]..... **83**
- Figure 4-4.** Index of refraction and extinction coefficient of a sputtered silicon dioxide film..... **87**

- Figure 4-5.** Comparison of the index of refraction for amorphous silicon, nanocrystalline silicon, and a reference single crystal silicon [96]. ..... **88**
- Figure 4-6.** Comparison of the extinction coefficient for amorphous silicon, nanocrystalline silicon, and a reference single crystal silicon [96]. ..... **89**
- Figure 4-7.** AFM scan of a pnc-Si film supported by the Si scaffold. Dark spots indicate the porous regions. RMS roughness of the non-porous background is 2.9 Å. .... **90**
- Figure 4-8. (a)** Membrane deflection experimental setup. A white light interferometer is used to measure the height of a membrane under pressure. **(b) – (d)** Deflection behavior of a 15 nm thick pnc-Si membrane 400  $\mu\text{m}$  x 400  $\mu\text{m}$  under 0.1, 0.3, and 0.5 PSI of pressure. .... **95**
- Figure 4-9. (a)** Bright-field optical image of a 50 nm thick porous silicon nitride membrane. The holes are 3  $\mu\text{m}$  in diameter with a pore pitch of 6  $\mu\text{m}$ . **(b)** Pressure-displacement behavior of the silicon nitride membrane. The Young's modulus and residual stress was extracted from a least-squares curve fit using Equation 4-15.. **97**
- Figure 4-10.** Pressure-displacement curve for three different pnc-Si membrane geometries. The solid line represents the least-squares fit to the generalized bulge equation. The inset shows a three-dimensional rendering of the membrane under pressure as measured by the white light interferometer. .... **99**
- Figure 5-1. (a)** Schematic of the rapid thermal processing unit used for carbonization. Membrane chips are placed inside a SiC coated graphite susceptor. A mixture of argon and acetylene is introduced into the chamber and heated to high temperatures. Two thermocouples monitor the temperature uniformity of the process. **(b)** (1)

Contact angles of an untreated ( $76^\circ$ ), (2) ozone treated ( $16^\circ$ ), (3) carbonized ( $60^\circ$ ), and (4) carbonized and ozone treated ( $22^\circ$ ) membrane. .... **104**

**Figure 5-2.** TEM images of carbonized membranes at different temperatures: (a) untreated, (b)  $600^\circ\text{C}$ , (c)  $700^\circ\text{C}$ , (d)  $750^\circ\text{C}$ . Scale bar is 20 nm. A 10% acetylene in argon mixture was used with a five minute soak time. (e) Pore size distribution as calculated from TEM images (f) Graph showing size (blue 'X') and porosity dependence (red 'O') with soak temperature. The standard deviation of porosity and diameter is 0.25% and 0.5 nm, respectively. .... **106**

**Figure 5-3.** Pore distribution of a membrane annealed for five minutes at  $800^\circ\text{C}$  in 10 slm of Ar. There is no change in pore structure before and after annealing. .... **106**

**Figure 5-4.** TEM images of carbonized membranes with 10% of  $\text{C}_2\text{H}_2$  at  $750^\circ\text{C}$  and various soak times: (a) untreated, (b) 5 minutes, (c) 10 minutes. A 15-minute soak time (d) occluded the majority of pores. Scale bar is 20 nm. (e) Pore size distribution as calculated from TEM images (f) Graph showing size (blue 'X') and porosity (red 'O') dependence with treatment time. The standard deviation of porosity and diameter is 0.3% and 0.7 nm, respectively. .... **108**

**Figure 5-5.** Width of carbon deposit width versus pore size. The growth rate of carbon is unaffected by pore size. .... **109**

**Figure 5-6.** High-resolution bright field TEM images of a carbonized pore. The inset shows an x-ray energy dispersive x-ray (EDX) scan of a single carbonized pore. The EDX scan highlights areas of Si (red) and C (blue) composition. Label 1 marks a  $\langle 111 \rangle$  oriented Si nanocrystal at the perimeter of the original pore wall. The carbon layer is highlighted by the arrow (2). Atomic ordering can be seen far from

the original pore wall consistent with the spacing ( $3.6 \text{ \AA}$ ) between sheets of graphite  
(3)..... 110

**Figure 5-7.** Carbonized and untreated pnc-Si membranes after 1 hour in 5% KOH at  $40^{\circ}\text{C}$ . The rectangular slits are free-standing pnc-Si. Untreated membranes are discolored indicating the dissolution of the silicon film [56]. ..... 111

**Figure 5-8.** Pore size distribution of a carbonized membrane before (blue solid) and after (red dashed) ozone treatment. The pores are slightly enlarged after treatment due to the removal of a few carbon layers..... 113

**Figure 5-9.** Aluminum pressure cell used for permeability and filtration experiments. A seal is created by a silicone gasket between the top of the aluminum cell and the plastic SepCon vial. A pnc-Si membrane chip rests at the bottom of the SepCon vial and is sealed with PDMS. Pressure is monitored by a gas manometer attached to the cell inlet. .... 114

**Figure 5-10.** Calculation of the theoretical hydraulic permeability from the size distribution of an actual membrane using the Dagan equation on a pore-by-pore basis. .... 115

**Figure 5-11.** Hydraulic permeability of untreated and carbonized pnc-Si membranes. The permeability of a carbonized membrane matches the theoretical prediction. The average pore diameter and porosity for each membrane are shown under each bar. The error bars represent the measurement error in flow. It does not include the variability in the pore size calculation from TEM micrographs..... 115

**Figure 5-12.** Raw absorbance scans of filtrate solutions and the 1:1 gold colloid stock dilutions. .... 117

- Figure 5-13.** Raw absorbance data and standard curves. The standard curves were generated by taking the absorbance peak at 280 nm for BSA and  $\beta$ -galactosidase and 410 nm for cytochrome c. .... **120**
- Figure 5-14.** Cartoon showing one cycle of aluminum oxide growth on silicon by atomic layer deposition. (a) Water vapor hydroxylates the silicon surface. (b) Trimethylaluminum is introduced and reacts of the surface hydroxyl groups. Unreacted precursor molecules are evacuated from the chamber before a second pulse of water is injected. (c) - (d) Water is pulsed and reacts with the surface to form hydroxylated aluminum oxide. Methane is produced as a byproduct gas. Unreacted water and methane is purged before step (b) is repeated. .... **123**
- Figure 5-15.** TEM micrographs of an (a) untreated and (b) – (d) alumina-coated pnc-Si membranes. The treated membranes were coated with (b) 5 nm, (c) 10 nm, and (d) 20 nm of  $\text{Al}_2\text{O}_3$ . (e) The pore size histogram shows that the distribution shifts by the thickness of deposition (multiplied by a factor of two because the coating is conformal along the pore wall). .... **125**
- Figure 5-16.** High-resolution TEM micrograph of an aluminum oxide coated nanopore. .... **125**
- Figure 5-17.** Atomic force microscopy scan of a pnc-Si membrane coated with 5 nm of aluminum oxide. RMS surface roughness was calculated to be 0.3 nm. .... **126**
- Figure 5-18.** Water contact angles of (from left to right) an untreated ( $83^\circ$ ), oxygen plasma treated ( $14^\circ$ ), alumina-coated ( $56^\circ$ ), and alumina and oxygen plasma treated ( $18^\circ$ ) pnc-Si membrane chip. .... **127**

- Figure 5-19.** High-resolution TEM micrograph of a pnc-Si nanopore coated with aluminum oxide and graphene..... **130**
- Figure 5-20.** High-resolution TEM micrograph of uncoated and alumina-coated membranes carbonized for different time periods. The scale bars are 5 nm ..... **131**
- Figure 5-21.** The thickness of carbon deposited on a bare silicon and alumina surface after carbonization versus process time. The 15-minute time point on the alumina surface could not be calculated since all the pores had been occluded after treatment. .... **132**
- Figure 5-22.** Pore size distributions after carbonization on a bare (top) and alumina-coated (bottom) membrane. The data is presented as a percent of total pore population. A Gaussian fit was applied to the histograms in order to visualize the increase in pore size cut-off sharpness in the carbonized alumina-coated membrane. .... **133**
- Figure 6-1.** Simplified hydrogen fuel cell structure. Oxidation occurs at the anode and creates protons, which are permeable through the ionic membrane. Electrons travel through an electronic conductor to generate current through a load. Reduction occurs at the cathode where hydrogen ions, electrons, and oxygen form water. .. **137**
- Figure 6-2.** A typical fuel cell current-voltage characteristic curve [135]. The linear region in the middle of the curve is due to resistive losses. By decreasing the resistance an increase in operating voltage is achieved as demonstrated by the dashed line. .... **140**
- Figure 6-3. (a)** Proposed microfluidic protein separation device. A pnc-Si membrane chip is sandwiched and sealed in between two PDMS serpentine channel pieces.



Inlet and outlet ports provide access to the pumping mechanism and fluid reservoir (not shown). **(b)** Top-down view showing alignment of the fluidic channel with the membrane area **(c)** A cross-sectional schematic showing separation in a cross-flow configuration..... **143**

**Figure 6-4.** This cartoon demonstrates the benefit of a multi-stage membrane scheme (left). A complex mixture is introduced in the top stage. Membrane A passes all species except for the largest. There is a slight loss of concentration in the membrane A filtrate due to diffusion limits. With each successive stage, larger species are retained while the smallest pass through. Membrane distributions (center) will be chosen for optimal transmission/retention. Each channel will be fed to a mass spectrometer for analysis. The ability to isolate a small species not resolvable in the unfiltered channel is demonstrated (right). ..... **145**

# Foreword

This thesis was a result of work performed in the Nanomembrane Research Group at the University of Rochester, led by Professors Philippe Fauchet and James McGrath. Consequently, many of the results presented in this work have been found with the assistance of others. Dr. Christopher Striemer originally discovered porous nanocrystalline silicon during his time as a doctoral student under the supervision of Prof. Philippe Fauchet. Dr. Striemer and Dr. Thomas Gaborski, who was at the time a Ph.D. candidate under Prof. James McGrath, first demonstrated the use of pnc-Si as a molecular sieve. Jon-Paul DesOrmeaux and Charles Chan of SiMPore, Inc. performed frontend processing of the porous nanocrystalline silicon membranes, including the cleaning of wafers and photolithographic patterning, as described in Chapter 2. The theories presented in Chapter 3 were developed after conversations with Dr. Christopher Striemer. The ellipsometric data presented in Chapter 4 was collected in part by Yijing Fu. Dr. Michael Bindschadler developed the pore processing routines. The atomic force microscopy work was performed with the assistance of Dr. Barrett Nehilla and Graham Marsh. The membrane deflection measurements were performed in part by Jon-Paul DesOrmeaux. The idea for rapid thermal carbonization of pnc-Si, described in Chapter 5, originated from conversations with Jessica Snyder and Dr. Christopher Striemer. X-ray spectroscopic scans were performed with the assistance of Brian McIntyre. Hydraulic permeability, gold nanoparticle and protein separations were done with assistance from Dr. Thomas Gaborski, Nakul Nataraj, and Jessica Snyder.

# Chapter 1. Introduction

## 1.1 A nano world

Nanoscience is the study of objects that are very small, between 1 and 100 nanometers, about 80,000 times smaller than the width of human hair [1]. Nanotechnology has been applied to numerous industries such as electronics, medicine, food, energy, and even in clothing [2]. A fundamental operation in nanoscience is the separation and concentration of nano-sized objects. For example, the development of drug proteins involves screening processes where denatured and/or aggregates are filtered from the eventual product [3]. Chromatography columns or sheet membranes are typically employed for this task. However, these conventional materials are unable to filter species *efficiently* due high losses and/or hindered mass transport. Advances in materials science and engineering have contributed greatly to the development of a new class of materials that enable interaction and manipulation of objects at the nano-scale in unprecedented ways. In the next sections, a review of state-of-the-art membrane materials that have been designed to address nanofiltration will be presented.

## 1.2 Membrane technology

Membrane use is ubiquitous in science. Their application ranges from separating and purifying biological products [4-10] to sequencing DNA [11-16] to use in fuel cells [17-21]. Recent breakthroughs in materials engineering has yielded a new class of membranes, such as solid-state nanopore devices [22-25], carbon nanotube (CNT) membranes [26-30], and polymeric track etched membranes [4, 31-34]. In the following sections, the basic manufacturing techniques and features of these devices will be examined as a prelude to the exploration of a novel membrane material: porous nanocrystalline silicon (pnc-Si).

### 1.2.1 Polymer track etched membranes

In general, track etched membranes are fabricated by irradiating a sheet of polymer material, such as polyethylene terephthalate (PET) [33] or polycarbonate (PC) [35], with heavy energetic ions that “drill” holes in the material. A subsequent chemical etch enlarges the “track” etched by the ion bombardment. These membranes are commercially available and can withstand high pressures approaching 3,000 PSI [36, 37]. They are typically 100  $\mu\text{m}$  – 1,000  $\mu\text{m}$  thick with average pore sizes ranging from 10 nm – 100 nm with porosities that approach 10%. Although polymer track etch membranes have high yield strengths and encompass a wide range of pore sizes, they have several disadvantages. First, they cannot withstand high temperature processes above 130°C. This limits their use in post-fabrication modification techniques, which

rely on high temperature deposition techniques such as atomic layer deposition (ALD). Second, the relatively large membrane thickness reduces the permeability of the membrane to diffusing and convecting species since transport is proportional to  $1/t$ , where  $t$  is the thickness of the membrane [38]. Third, limitations in manufacturing cause track etched pores to have irregularly shaped pore cross-sections [35, 39, 40] and “double” pore structures. That is, track etched membranes frequently have outlier pores many times larger than the average pore size due to overlapping pores (Figure 1-1) [39].

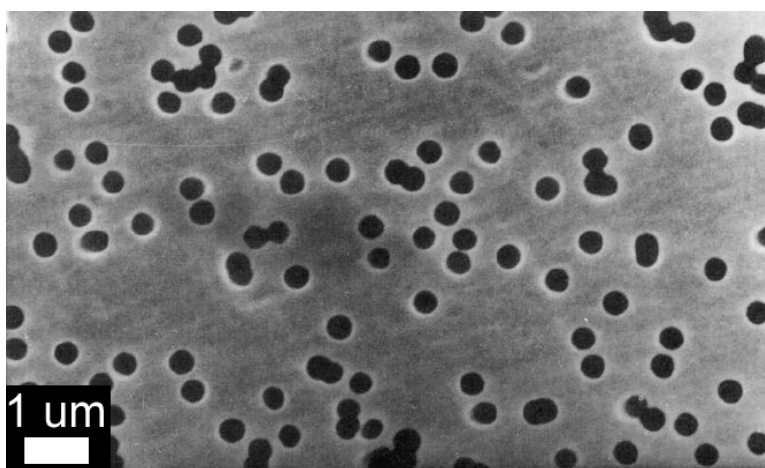


**Figure 1-1.** Scanning electron microscopy micrograph of a polycarbonate track etched membrane showing overlapping pores [39].

### 1.2.2 Carbon nanotube membranes

Carbon nanotubes are at the forefront of nanoscience research. Since their discovery, they have been presented as an ultra-strong building material [41], a superconductor [42], and as a nano-sieve [27, 28, 30]. The use of carbon nanotube

membranes as a filter is particularly attractive due to this enhanced permeability to water derived from the weak interaction between the water and hydrophobic ultra-smooth carbon walls [30, 43]. One disadvantage of CNT membranes is their complicated requirements for fabrication and limited availability in a wide range of pore sizes. Current state-of-the-art techniques to fabricate CNT membranes require the growth of vertically aligned carbon nanotubes (VA-CNT) followed by the deposition of a matrix material, such as polystyrene [30] or silicon nitride [28], in order to provide structural integrity to the membrane. Yu *et al.* demonstrated the fabrication of densely packed CNT membranes with an average diameter of 3 nm and porosity of 20% without the use of a “filler” material, but did not extend the technique to larger tube diameters [27]. Thus, it remains unclear whether CNT membranes can be used to separate species greater than a few nanometers in size.

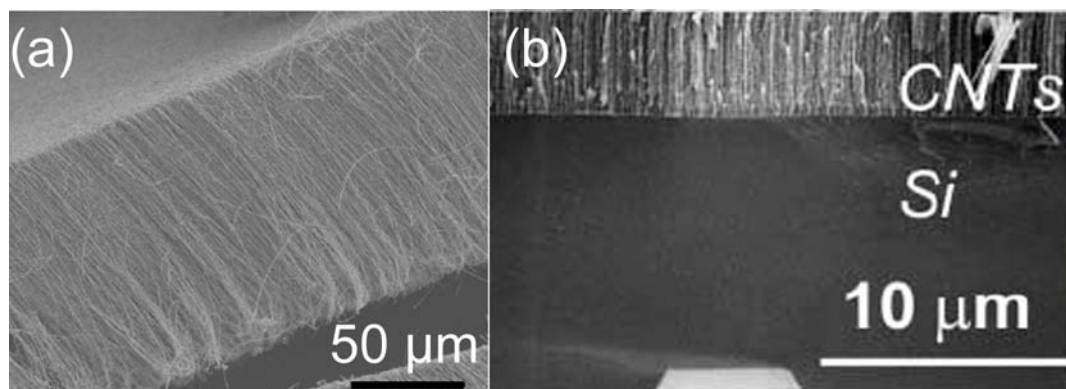


**Figure 1-2.** (a) Vertically aligned carbon nanotubes [30] (b) Carbon nanotubes in a silicon nitride matrix supported by a silicon scaffold [28].

### 1.2.3 Solid-state nanopore membranes

Recent work in micro and nanofabrication has not only benefited the electronics industry but also other areas such as membrane science. The introduction of solid-state nanoporous membranes opens the possibility for the manufacturing of devices on a scalable platform, such as silicon, that is compatible with micro-electric-mechanical systems (MEMS) technology [6, 22-24, 34, 44-49]. This is particularly attractive for lab-on-chip and microfluidic applications where the separation of species without convective mixing is an important problem. Solid-state membranes have many features that carbon nanotube membranes and polymer membranes lack. They are robust and can withstand high temperatures, can be fabricated using established semiconductor processing techniques, and are compatible with scale-up materials such as a silicon wafer. Additionally, advanced photolithography can be employed to define feature sizes from a few nanometers to several microns.

Recent progress in the development of solid-state nanoporous membranes have relied primarily on a top-down fabrication approach, employing photolithography, thin film deposition, and ion milling to define the nanopores [22, 50, 51]. This top-down approach is often resource intensive and requires long processing times. In this thesis, a systematic study of porous nanocrystalline silicon (pnc-Si), first introduced by Striemer *et al.* in 2004 [52], will be carried out. One of the many advantages of pnc-Si membranes is that they are fabricated using a bottom-up approach. Thus, they inherit all the benefits of solid-state nanoporous membranes with the additional feature of ease of manufacturing (Figure 1-3).

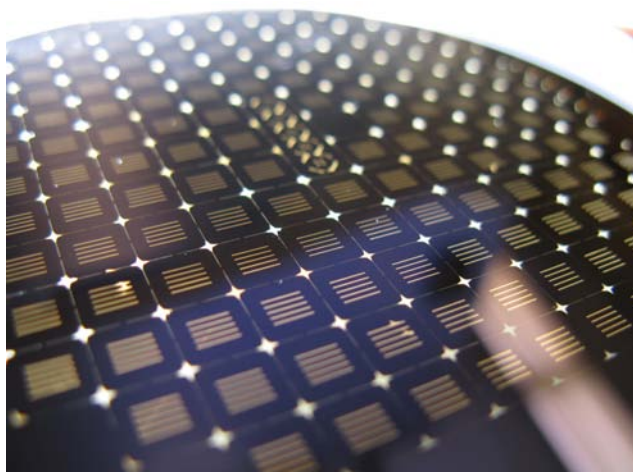


**Figure 1-3.** Hundreds of membrane “chips” can be produced on a single 4-inch silicon wafer. The golden rectangular features are areas of free-standing pnc-Si.

## 1.3 Porous nanocrystalline silicon membranes

Porous nanocrystalline silicon (pnc-Si) membranes are a new class of solid state membranes that have been shown to demonstrate efficient selectivity of macromolecular species based on size and charge [53], precise separation with minimal loss of nanoparticles [54, 55], and viability as a cell culture substrate [56]. As described in the previous sections, current state-of-the-art membranes suffer from low transport rates due to large thicknesses (see Table 1-1) or are difficult manufacture [23, 57]. Pnc-Si membranes do not suffer from any of these disadvantages and they have been demonstrated to have very fast transmission of diffusing molecular species because they



are at least an order of magnitude thinner than any reported micro-machined membrane [58, 59].

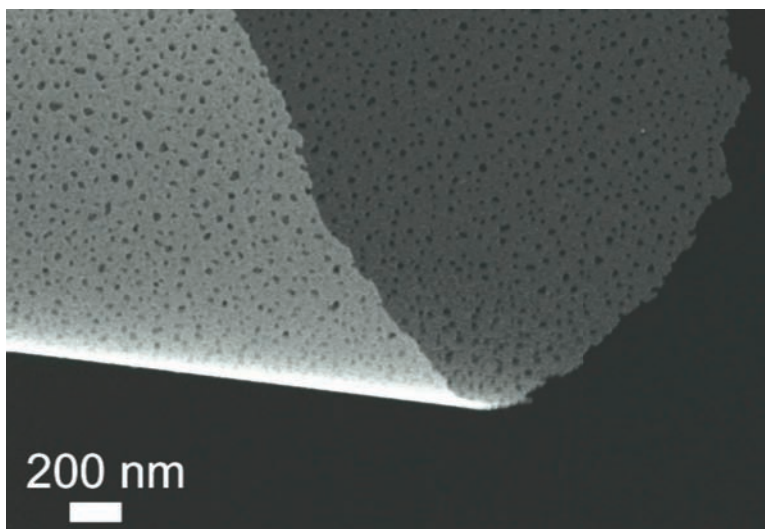


**Figure 1-4.** Scanning electron microscopy image of a hanging sheet of pnc-Si demonstrating the material's molecular thinness.

The sieving properties of a membrane are heavily reliant on the size, density, and shape of the pores. Thus, it is imperative that methods for controlling these characteristics of pore morphology are determined. Chapter 2 will be devoted to developing an understanding of the morphological changes associated with different fabrication conditions, which is essential for fabricating membranes that are suitable for the separation of a variety of species of interest. Chapter 3 will focus on establishing an empirical model for the pore formation process. The stages of pore nucleation and growth will be examined and the relationship between silicon crystallization and pore formation will be formalized. In Chapter 4, the basic physical properties of pnc-Si using a variety of characterization tools will be presented. Next, post-production pore size

tuning and functionalization techniques will be discussed in Chapter 5. Additionally, the hydraulic permeability of pnc-Si and their ability to separate nanoparticles and proteins will be evaluated. Finally, in Chapter 6 future research directions will be proposed.

**Table 1-1.** Pore size and thickness range of nanopore membranes

Material	Pore sizes (nm)	Thickness (nm)	References
Carbon nanotube	1 – 5	750,000	[27]
PC track etch	10 – 100	10,000 – 20,000	[31]
Silicon nano-slit	10	4,000	[25, 51, 60]
Porous aluminum oxide	60	80,000	[49]
Pnc-Si	< 5 – 80	15 – 30	[52, 53]

## 1.4 Conclusions

The separation and concentration of nanoscale objects is an important operation in science. New membrane materials have been created to meet this challenging problem. The purpose of this thesis is to understand porous nanocrystalline silicon as a revolutionary material that can be applied to basic scientific research as well as many areas of industry. Methods for controlling the pore properties of pnc-Si, mechanisms of pore formation, basic physical properties, methods for functionalization of pnc-Si, and applications involving high permeability and filtration will be presented.

# **Chapter 2. Fabrication of porous nanocrystalline silicon membranes**

## **2.1 Introduction**

In this chapter, a review of the fabrication of porous nanocrystalline silicon membranes will be presented. Important manufacturing techniques such as thin film deposition, thermal annealing, and wet chemical etching will be reviewed. Key parameters that affect the pore properties such as the thin film deposition and thermal annealing conditions will be explored. Lastly, some practical considerations in the fabrication of pnc-Si will be discussed.

## **2.2 Process overview**

The fabrication of porous nanocrystalline silicon membranes is straightforward and takes advantage of common semiconductor practices (Figure 2-1) [53]. By utilizing a silicon platform, several hundred-membrane devices can be fabricated simultaneously on a single 4-inch wafer, much like microprocessors in modern day computers. First, a 1000 Å thermal silicon dioxide layer is grown on a <100> oriented N-type wafer (1 – 5 Ω•cm). The oxide is patterned using standard lithographic techniques, which define the

active area of the final membrane as well as the outer dimension of the chip. The unpatterned oxide is then stripped leaving a bare silicon surface on one side of the wafer. A three-layer stack of silicon dioxide (20 nm) / amorphous silicon (15 – 30 nm) / silicon dioxide (20 nm) is deposited on the bare wafer surface using rf magnetron sputtering (ATC-2000V, AJA International, Inc., North Scituate, MA). The SiO<sub>2</sub> (99.995%, Kurt J. Lesker Co., Pittsburgh, PA) is directly sputtered and used as an etch stop for a subsequent bulk silicon etch step. Intrinsic amorphous silicon (99.999%, Kurt J. Lesker Co., Pittsburgh, PA) is sputtered from a crystalline silicon target with a well-optimized recipe yielding high quality silicon films as verified by AFM and spectroscopic ellipsometry (see section 4.3.4). After the thin film deposition, a rapid thermal anneal is performed which induces solid phase crystallization (SPC) of the amorphous silicon layer (Solaris 150, Surface Science Integration, El Mirage, AZ). During this phase transformation, the formation of nanopores in the silicon film is observed. The ramp rate, final annealing temperature, silicon thickness, and application of substrate bias are important controls for the size, shape, and density of the pores, which will be discussed in the following sections. After the thermal treatment, the patterned wafer surface is subjected to a single-sided wet anisotropic etchant, Ethylene Diamine Pyrocatechol with Pyrazine (EDP-300F, Transene Company, Inc., Danvers, MA), which has a high silicon-to-oxide etch ratio. After the bulk silicon etch is complete and the membrane is released over the silicon chip scaffold, the protective SiO<sub>2</sub> layers are removed with buffered oxide etchant (10:1 with surfactant, Mallinckrodt Baker, Phillipsburg, NJ).

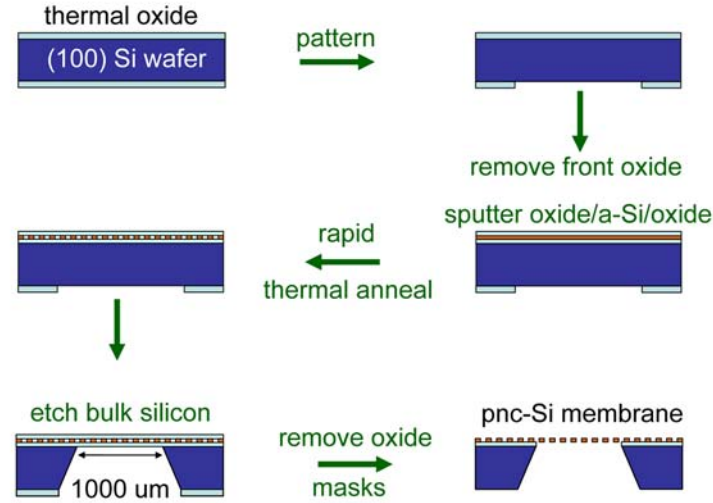


**Figure 2-1.** Process flow for the fabrication of porous nanocrystalline silicon membranes.

## 2.3 Wafer preparation and patterning

Fabrication begins with a RCA clean of a bare 4-inch, <100>, 200 μm, N-type (phosphorus), > 1 Ω-cm, double-side polished silicon wafer. It is imperative that the wafer surface be free of defects before further film growth and deposition. The first stage of the RCA clean, i.e. standard clean 1 (SC-1), consists of soaking the wafer in a bath of de-ionized (DI) water, hydrogen peroxide (H<sub>2</sub>O<sub>2</sub>, 30% wt), and ammonium hydroxide (NH<sub>4</sub>OH, 29% wt NH<sub>3</sub>) at a ratio of 15:5:1 heated to 75°C for 10 minutes. The SC-1 clean removes organic contaminants by taking advantage of the strong oxidizer H<sub>2</sub>O<sub>2</sub>, which forms a thin chemical oxide layer on the surface. The chemical oxide is etched by the NH<sub>4</sub>OH and this cycle of growth/etch is repeated until the H<sub>2</sub>O<sub>2</sub> is exhausted. The

under-cutting of oxide dislodges many of the particulates on the wafer leaving a clean surface. Any chemical oxide remaining on the wafer after the SC-1 clean is removed by dipping the wafer in a dilute 20:1 DI water/Hydrofluoric acid (HF, 49% wt) solution. The next step in the RCA clean is the standard clean 2 (SC-2), which involves soaking the wafer in a 15:5:1 mixture of DI water,  $\text{H}_2\text{O}_2$ , and hydrochloric acid (HCl, 37% wt) at  $75^\circ\text{C}$  for 10 minutes. The SC-2 clean removes metal contaminants by forming complexes between the metal ions and chloride [61]. The resulting ion has a higher solubility, which can then be readily removed from the wafer surface.

After the RCA clean,  $1000 \text{ \AA}$  of dry thermal oxide is grown on the wafer in a furnace oven. The silicon dioxide serves as a masking layer that will be patterned in a subsequent step. It also protects the front-side surface (device side) during the patterning step. The non-uniformity of the film is nominally  $< 5\%$ . The backside surface is patterned using standard photolithography techniques. Hexamethyldisilazane (HMDS) is applied to the backside of the wafer to help photoresist adhesion. Approximately  $1 \mu\text{m}$  of positive photoresist (Shipley 1813) is then spun onto the backside of the wafer. A mask transparency is used to expose the pattern onto the photoresist using UV excitation. The pattern is developed and etched into the silicon dioxide using 10:1 HF for 3 minutes 30 seconds. The front-side oxide is also removed in this step. The photoresist is removed using a Piranha solution consisting of a 50:1 mixture of concentrated sulfuric acid ( $\text{H}_2\text{SO}_4$ ) and  $\text{H}_2\text{O}_2$  (30% wt) at  $140^\circ\text{C}$  for 10 minutes. The wafer is then subjected to a final RCA clean before the thin film deposition.

## 2.4 Thin film deposition

Rf magnetron sputtering is a physical vapor deposition (PVD) technique used to deposit highly uniform films on substrates. Film quality is determined by density, purity, and uniformity of the film. These properties are carefully optimized by tuning several deposition conditions such as deposition temperature, rf bias on the substrate, base vacuum pressure, and working process pressure. It will be shown that the aforementioned film characteristics contribute greatly to the final membrane morphology.

### 2.4.1 Sputtering discharges

Sputtering is the process by which energetic ions (argon) in a plasma are accelerated by an electric field towards a target (cathode). The word *plasma*, Greek for “to mold”, was coined by Irving Langmuir after he discovered that a “glow discharge” could be contained between the anode and cathode in a high DC field [62]. As the ions strike the target surface they transfer energy to the target atoms, which are subsequently ejected as neutral particles. Because this process takes place in vacuum (a few millitorr), the mean free path of the target atom is long and deposition on a substrate several inches away from the source material is possible.

A simplified schematic of an rf sputtering system is shown in Figure 2-2. By using rf energy to bias the target, both conductive and insulating materials may be sputtered. Additionally, by placing magnets behind our targets, the ionization probability of the

argon is increased due to the electron trapping by the magnetic field (Figure 2-3). This results in a more efficient sputter yield and higher deposition rate.

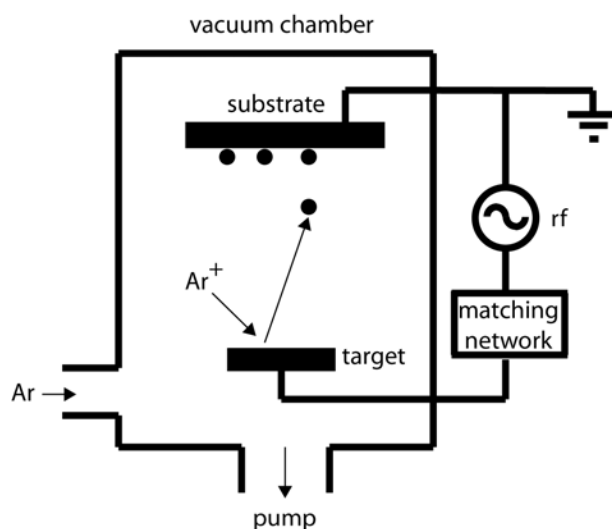


**Figure 2-2.** Simplified schematic of an rf sputter deposition system.

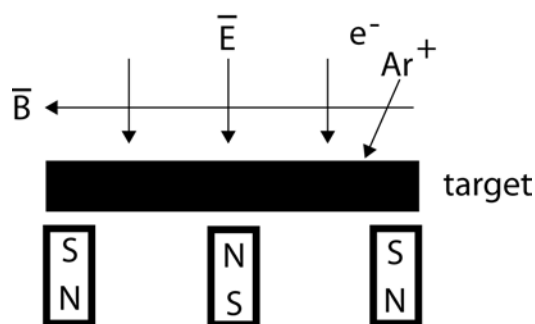


**Figure 2-3.** A planar magnetron configuration. The magnetic field lines are parallel to the target material. Electrons are “trapped” in the magnetic field, which increases ionization near the target surface.



### 2.4.2 Sputter equipment

The thin films deposited in this work were produced using an AJA International (Scituate, MA) ATC-2000-V magnetron confocal sputtering system. The substrate is mounted and rotated on a central axis with the sputtering sources arranged radially about the axis (Figure 2-4). In this system, the angle of the targets can also be adjusted to achieve exceptionally high uniformity of  $\sim 1\%$  across substrates as large as 6 inches (Figure 2-5).



**Figure 2-4.** Physical vapor deposition by rf magnetron sputtering using a confocal target arrangement. The substrate is suspended from the rotation stage at the top of the image. The substrate may be heated via tungsten-halogen lamps to temperatures between room temperature and 800°C.

The ATC 2000-V is capable of sputter depositing nearly any metal, semiconductor, or insulator. In addition to supporting multiple target materials, this tool is able to drive two power supplies simultaneously thus allowing for co-sputtering for composite films or increased deposition rates. This system has a dedicated supply for generating an rf plasma around the substrate, as well i.e. substrate bias. This plasma will densify and smooth the depositing film by constantly bombarding the surface with high-energy ions.

The substrate is heated with an array of quartz halogen lamps capable of reaching 800°C. This system has a load lock so that samples can be loaded/exchanged while keeping the main chamber at ultra high vacuum ( $< 5\text{e-}9$  torr). This not only reduces the time required to reach the base pressure but enables much lower base pressures to be achieved.

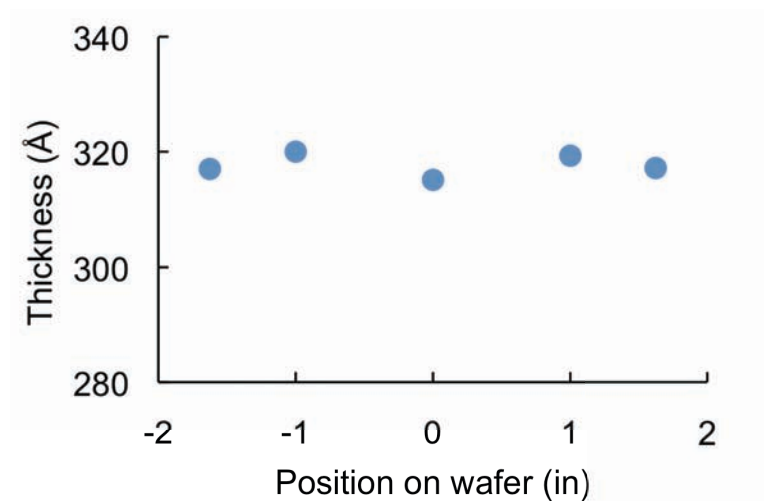


**Figure 2-5.** Thickness profile of a silicon dioxide thin film obtained by spectroscopic ellipsometry. The uniformity is  $\pm 0.6\%$ . Wafer position '0' refers to the center of a 4-inch wafer. The dip in the thickness profile is characteristic of magnetron sputtering and is a result of the plasma profile.

In this work, direct sputtering of silicon and silicon dioxide is utilized to form the three-layer membrane film stack. Typical deposition powers for the Si and SiO<sub>2</sub> are 300 W and 350 W, respectively. The DC bias voltage that develops across the target and ground is approximately 300 V for silicon and 200 V for oxide. The working pressure is maintained between at 3 mTorr and 5 mTorr for the silicon and oxide deposition, respectively. Under these conditions, the deposition rate is approximately 1.8 nm/min for silicon and 1 nm/min for silicon dioxide.

### 2.4.3 Deposition parameters

The deposited thin film structure consists of a three-layer silicon dioxide/amorphous silicon/silicon dioxide stack. The oxide thickness for this work was fixed at 20 nm. This thickness was chosen because it was found to provide adequate protection for the a-Si thin film during the silicon wafer through-etch step. Because the thin film deposition process greatly affects the ultimate membrane nano-structure, a systematic study was carried out focusing on several key parameters:

- a-Si film thickness
- Deposition temperature
- Substrate bias

In section 2.8, it will be shown that the above conditions all contribute in varying degrees to the film quality and final pore morphology.

## 2.5 Formation of pores by rapid thermal annealing

The crystallization of the amorphous silicon film is a crucial step in the pore formation process. As-deposited amorphous silicon film yields no visible pores in the membrane. However, if the thin film is crystallized, nanopores form concurrently with silicon nanocrystals (Figure 2-6). This is attributed to stress relaxation in the silicon film as thermal energy is used to arrange the Si atoms into ordered nanocrystals. The re-ordering of material involves a volume contraction in the film that facilitates the formation of pores [63, 64]. A detailed theory on the mechanisms of pore formation is presented in Chapter 3.

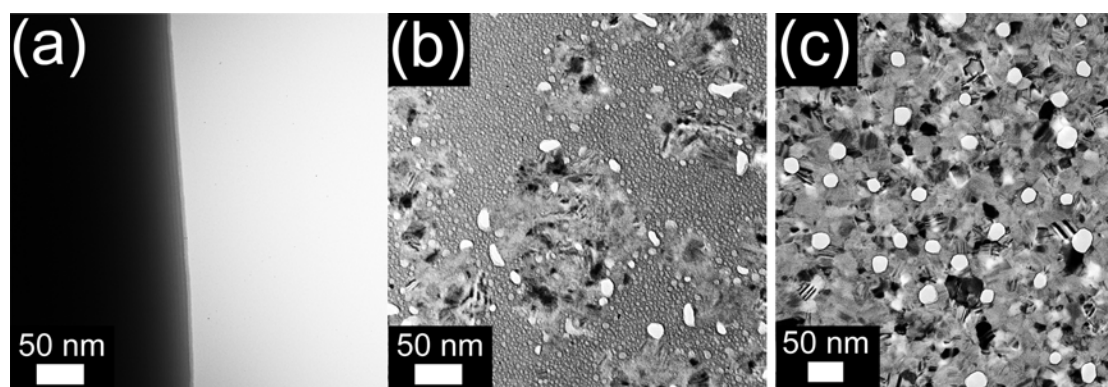


**Figure 2-6.** (a) Bright-field TEM micrograph of a 15 nm thick amorphous silicon membrane. The dark area represents the thick silicon support region and the white area represents the free-standing membrane area. (b) A partially crystallized 15 nm thick silicon film annealed at 700°C. The bright areas indicate through-pores and the dark areas are diffracting Si nanocrystals. Pores form preferentially at the amorphous-crystalline interface. (c) A fully crystallized 15 nm thick silicon film annealed at 1000°C.

During the anneal, the silicon film undergoes a phase transition from amorphous to nanocrystalline and changes from a compressive to tensile state [65]. This change is demonstrated by comparing a freestanding amorphous membrane to a freestanding crystallized silicon membrane. An amorphous membrane is slightly wrinkled due to the film's compressive nature [66]. A crystallized film will appear flat (tensile) due to stress relaxation after the thermal annealing process (Figure 2-7).

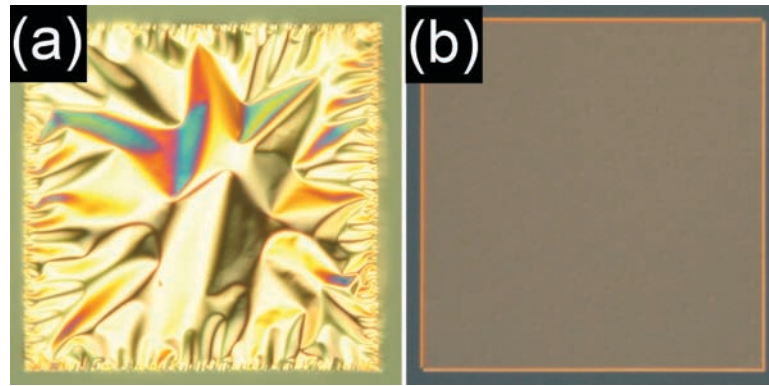


**Figure 2-7.** Optical image in Nomarski mode of a 15 nm amorphous silicon membrane (a) and pnc-Si membrane (b). Both membranes are 200  $\mu\text{m}$  x 200  $\mu\text{m}$ .

## 2.6 Rapid thermal annealing

It has been demonstrated that rapid thermal annealing (RTA) can crystallize thin amorphous silicon films in a few seconds and yield high quality polycrystalline structures [67]. Rapid thermal processing offers many advantages over traditional furnace annealing[68]. The two most attractive features of this technology are the tight

temperature control and short processing time. A typical RTA takes less than ten minutes. The Solaris 150 rapid thermal processor is capable of reaching 1300°C with ramp rates approaching 200°C/s using 21 tungsten-halogen lamps arranged above and below a quartz chamber. The wafer sits on a quartz tray and makes contact with the substrate via three small prongs (Figure 2-8). Temperature stability and accuracy is maintained by two silicon cap thermocouples inside the chamber and a proportional-integral-derivative (PID) controller (Figure 2-9). The thermocouples are in direct contact with the wafer during the annealing process. In addition to argon, a second process gas may be plumbed to the tool depending on the application.

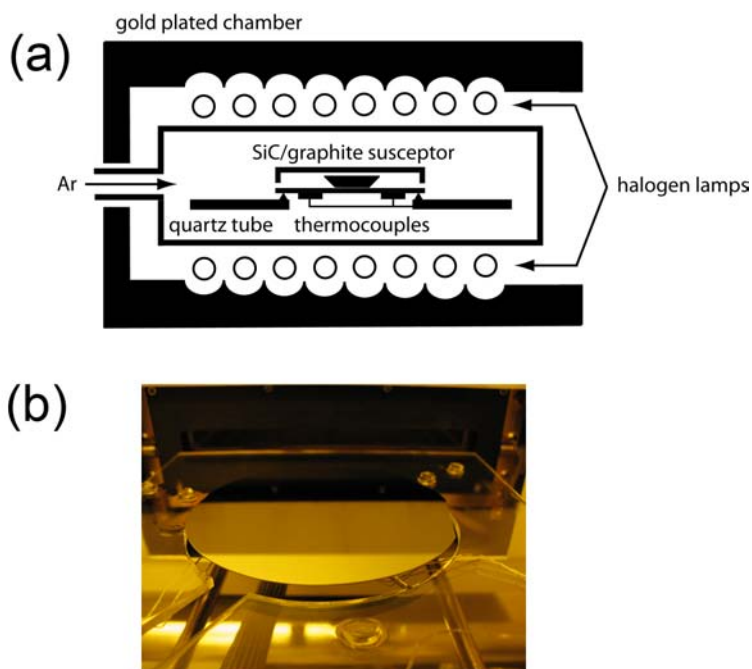


**Figure 2-8.** (a) Schematic of the RTP chamber. The wafer can be placed inside a silicon carbide coated graphite susceptor to improve heating uniformity. (b) Wafer sitting on the quartz RTP tray. Two thermocouples attached to the tray monitor the temperature during the annealing process.

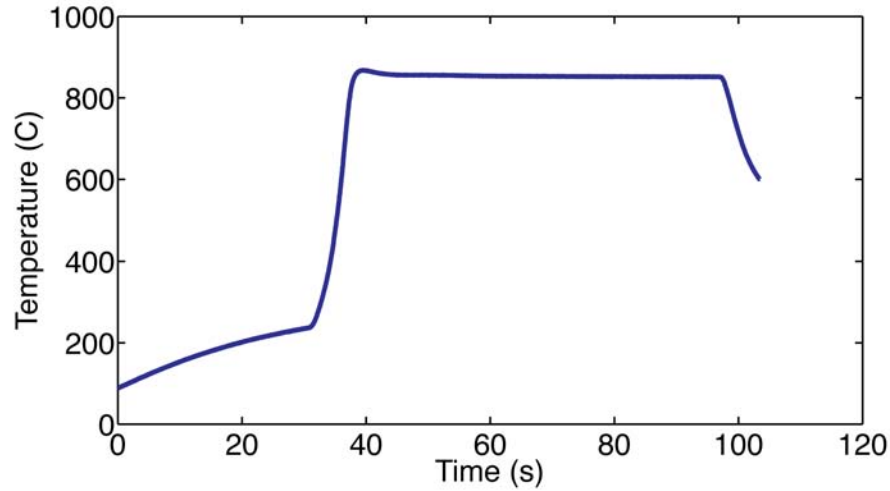
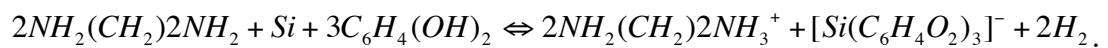


**Figure 2-9.** A typical temperature profile during the rapid thermal process. The ramp rate and soak temperature is precisely tuned using a PID controller. The first 30 seconds of the process is a purge in argon to flush out residual oxygen in the chamber. The slight temperature increase during this period is due to the warm chamber walls.

## 2.7 Anisotropic bulk silicon etching

An anisotropic etchant, Ethylenediamine Pyrocatechol (EDP), is used to release the membrane film stack from the bulk silicon substrate. The ethylenediamine oxidizes surface silicon atoms, which are then chelated by pyrocatechol to form a compound,  $[Si(C_6H_4O_2)_3]^-$ , that is soluble in ethylenediamine. The overall reaction is written as [69]:



**Equation 2-1**

EDP is highly selective and exhibits a 4000:1 Si:SiO<sub>2</sub> etch ratio at 110°C., thus making silicon dioxide a very effective etch-stop. EDP etches the (100) plane the fastest and the (111) plane approximately 20-times slower [69]. This anisotropy stems from the difference in binding energies of the different crystal orientations. As a result, the trenches formed after etching have a trapezoidal cross-section (Figure 2-10). With the addition of a catalyst, Pyrazine, EDP type 'F' (Transene, Danvers, MA) etches in the  $\langle 100 \rangle$  direction at a rate of approximately 1.5  $\mu\text{m}/\text{min}$  at 110°C.

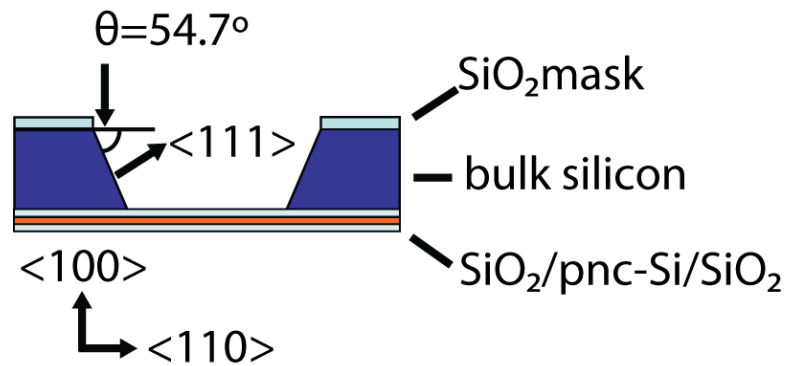


**Figure 2-10.** A trapezoidal cross-section results after bulk silicon micro-machining due to the anisotropic etch.

Etching is performed in a custom silicon wet-etch cell built by New York Manufacturing (Rochester, NY) after several prototypes were designed and built in-house (Figure 2-11). All surfaces in contact with the EDP etchant are made of grade 316 stainless steel. It was determined that a lesser grade of stainless steel is attacked by the etchant forming iron silicide precipitates that hinder the etch process. A thermocouple submerged in the etchant close to the wafer surface provides feedback to the



proportional-integral-derivative (PID) temperature controller (Omega CN8201). A magnetic stir bar suspended above the wafer stirs the solution generating a uniformly heated etchant. By taking advantage of bulk silicon micromachining, membranes in a variety of formats and geometries can be fabricated (Figure 2-12).

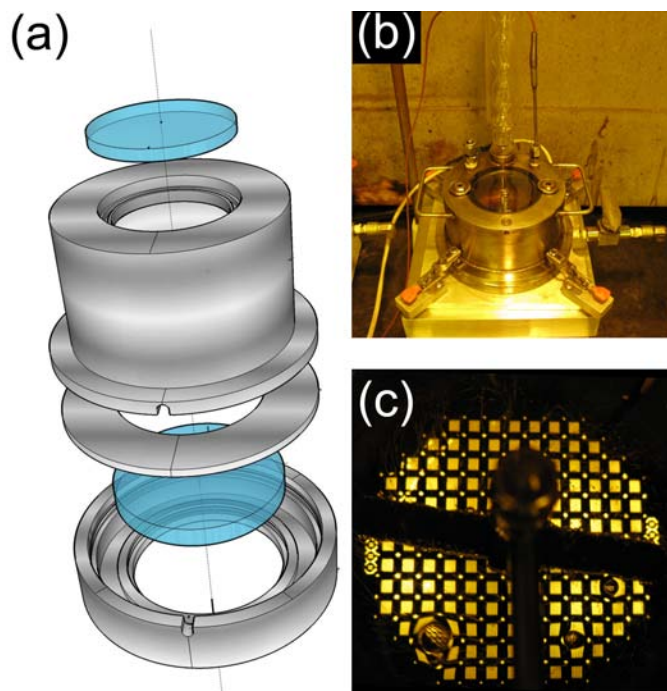


**Figure 2-11.** (a) Concept drawing of a custom-made silicon wet-etch cell. The wafer is sealed between the bottom glass disk and main etch cell body with an o-ring. (b) The fluid tight seal is made with four toggle clamps. A thermocouple submerged in the etchant monitors the temperature close to the wafer surface. A tube condenser captures any hazardous vapor. A quick drain allows for quick disposal of the etchant. (c) End point detection is achieved by illuminating the stir table. The light is transmitted through the released membrane and seen through a viewing window at the top of the etch cell.

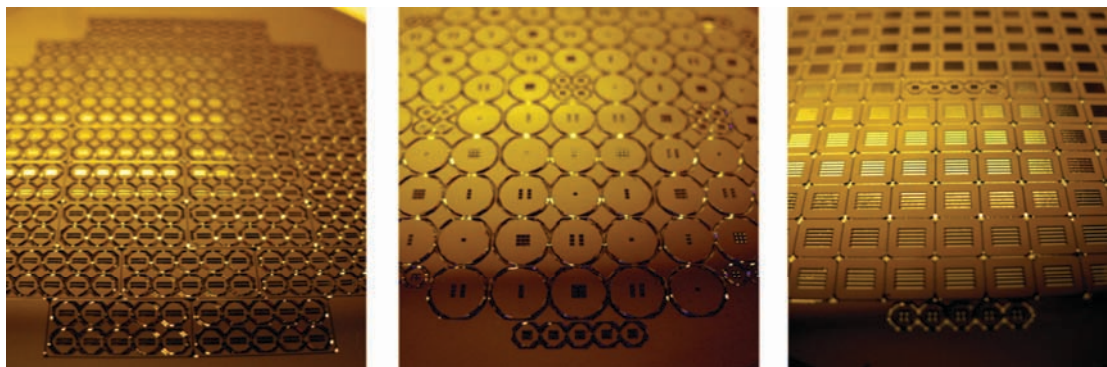


**Figure 2-12.** Silicon micromachining techniques allow for different patterns to be transferred and etched into wafers resulting in various membrane geometries. Shown above are three membrane patterns that have been etched into 4-inch silicon wafers.

## 2.8 Controlling pore morphology

### 2.8.1 Annealing temperature

As previously reported by Striemer *et al.* [53] and Fang *et al.* [70], the annealing temperature is an important determinant of pore size and density. This is most likely due to an increase in dynamic strain and atomic mobility during SPC at higher temperatures, which allows for the formation of larger pores in the crystallized film. Figure 2-13 shows a series of 15 nm thick membranes deposited with 25 W of applied substrate bias that were annealed at temperatures between 800°C and 1100°C. (Note that the pore size distributions are shown as continuous curves. See section 4.2.1 for a detailed description on the acquisition of pore size and density statistics.) The ramp rate was fixed at 100°C/s and the steady-state temperature was held for 60 s. Comparing membranes that were

annealed at 800°C and 850°C, the density of pores nearly doubled and the average pore size increased by 50% at the higher temperature. Pore density and size continue to increase with annealing temperature up to 1100°C. Beyond 1100°C a large number of thin-film delamination features appear causing a high pinhole defect density in the resulting membrane. By changing the annealing temperature between 700°C and 1000°C, the average pore diameter could be varied between 9.4 nm and 22.2 nm and the porosity between 0.5% and 6.6% in defect-free material\*.

---

\* The temperatures reported here for pore formation are higher than those originally published in Striemer *et al.* [53]. This discrepancy can be attributed to the fact that the membranes in this work were manufactured using a better-calibrated rapid thermal processor.

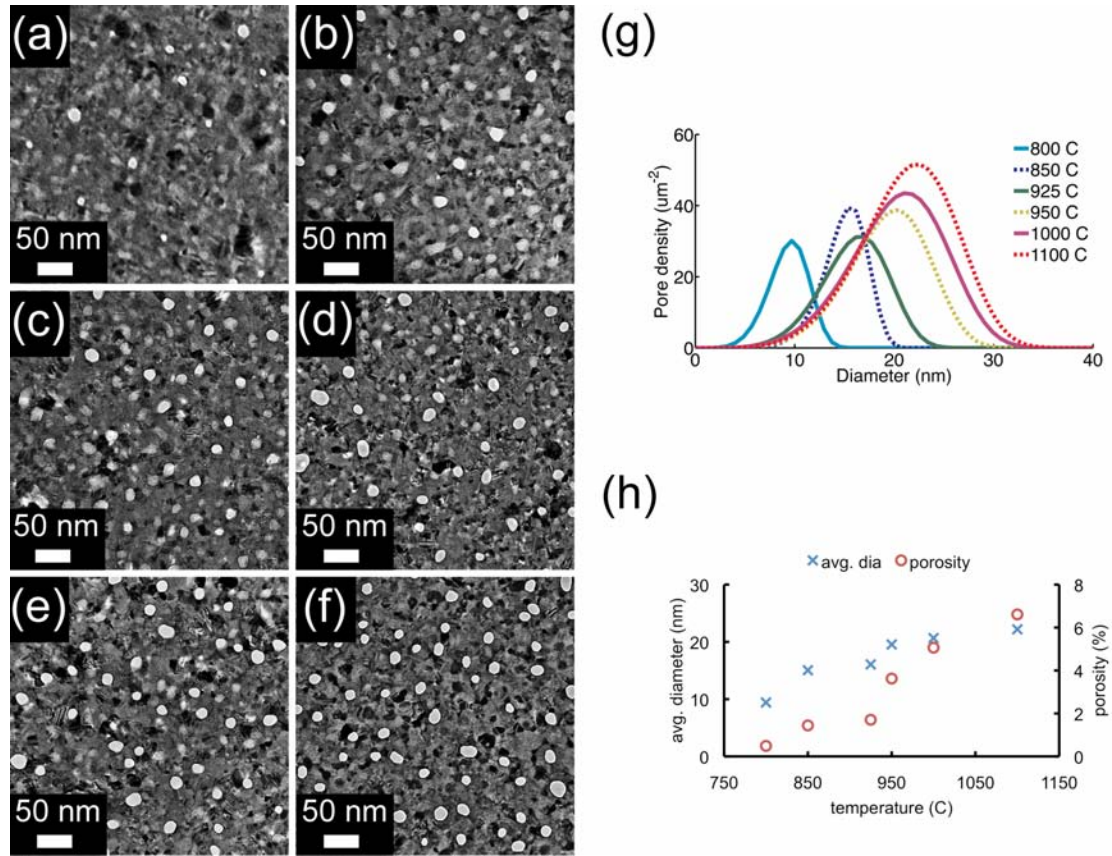


**Figure 2-13.** (a) – (f) TEM micrographs of 15 nm thick pnc-Si membranes annealed at 800°C, 850°C, 925°C, 950°C, 1000°C, and 1100°C. (g) The pore size distributions were calculated directly from TEM micrographs. (h) The average pore diameter and porosity is plotted for each annealing temperature.

### 2.8.2 Soak time

To investigate the effect of annealing time on pore size, a set of 15 nm thick silicon membranes deposited with 25 W of applied substrate bias were annealed for 10, 60, and 300 s in the RTP at 1000°C with a ramp rate of 100°C/s. Figure 2-14 shows that pore sizes and density increase with longer annealing times. While the average porosity only increased from 21.1 nm to 23.1 nm from a 10 s to 300 s anneal, the porosity changed

from 4.3% to 6.1%. This increase in porosity stems from the increase in pore density:  $120 \mu\text{m}^{-2}$  to  $140 \mu\text{m}^{-2}$  for a 10 s and 300 s anneal, respectively, as well as an increase in average pore diameter. It is worth noting that even with a very short anneal time of 10 s it is possible to produce a nanoporous membrane. These results indicate that the ramp-to-temperature step is critical in the pore formation process because the crystallization process takes place over very short timescales.

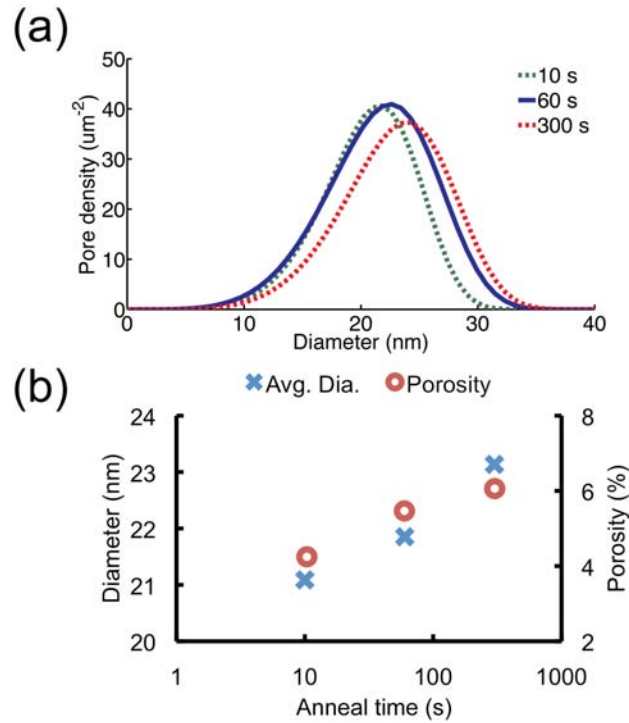


**Figure 2-14.** (a) Pore size distributions of 15 nm thick pnc-Si membranes annealed at 1000°C with a ramp rate of 100°C/s for 10, 60, and 300 s. (b) A plot of the average diameter and porosity of the membranes annealed for various times. Note the time scale is logarithmic.

An increase in pore diameter due to longer anneal times is evidence that there is a certain population of amorphous silicon remaining in between the nanocrystalline grains for short thermal treatments. For longer anneal durations, this amorphous volume decreases due to an increase in nanocrystal formation. Consequently, pore size increases due to the volume contraction associated with crystallization. This effect is shown in Figure 2-15.

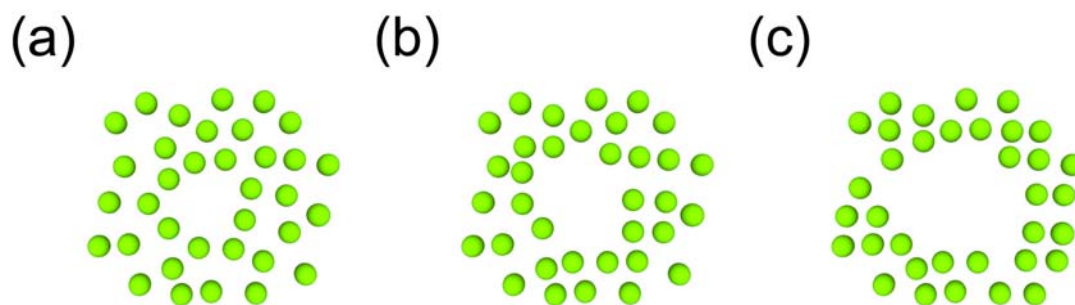


**Figure 2-15.** Cartoon showing Si atoms and a single pore for (a) short, (b) medium, (c) and long anneal durations. The population of amorphous silicon (disordered) decreases with time, while the nanocrystalline fraction (ordered) increases with longer anneal times. As a consequence of increased crystallization, pore size increases.

### 2.8.3 Annealing with a susceptor

Earlier, it was shown that the annealing temperature was an important determinant in a membrane's pore characteristics. Thus, it is hypothesized that the manner in which heat is transferred to the membrane film would have a significant effect on pore morphology. To explore this phenomenon, membranes were annealed inside a silicon

carbide coated graphite susceptor and compared to those that were annealed directly in the RTP chamber. Inside the susceptor, the films are heated by blackbody re-radiation from the susceptor walls and conduction across the narrow air gap inside the susceptor rather than the direct absorption of optical energy (primarily visible and infrared) from the halogen lamps inside the RTP. A ramp rate of 50°C/s was used due to the increased thermal load and damage threshold of the susceptor. The annealing time was fixed at 60 s. In Figure 2-16 and Figure 2-17, there is indeed a large difference in pore density between these two annealing schemes. Although the maximum pore sizes were similar, the density of the middle and lower pore sizes of the membranes annealed without the susceptor were almost three times that of the membranes annealed using the susceptor. Since amorphous silicon is a strong absorber of visible and near-IR radiation, there is likely to be some additional transient heating of this film when it is directly exposed to the lamp radiation during the annealing process.



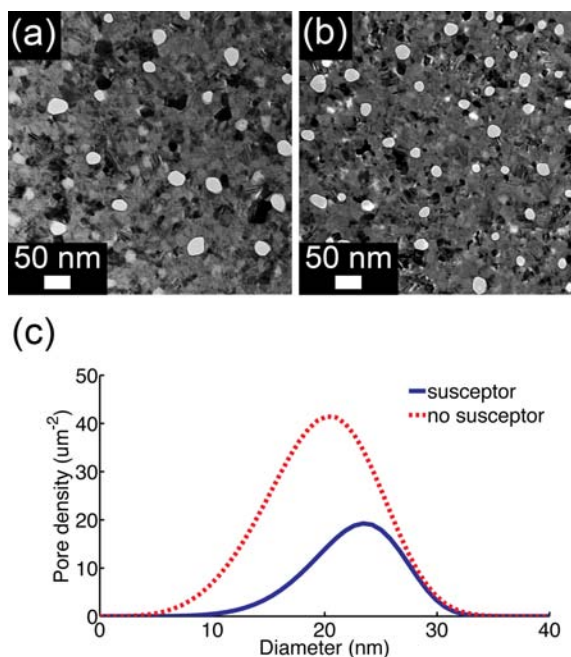


**Figure 2-16.** 15 nm thick pnc-Si membrane deposited with 25 W of applied substrate bias annealed at 1000°C with a ramp rate of 50°C/s (a) using a susceptor and (b) without a susceptor. (c) The pore size distributions show that the density of pores greatly increases when membranes were annealed outside the susceptor.

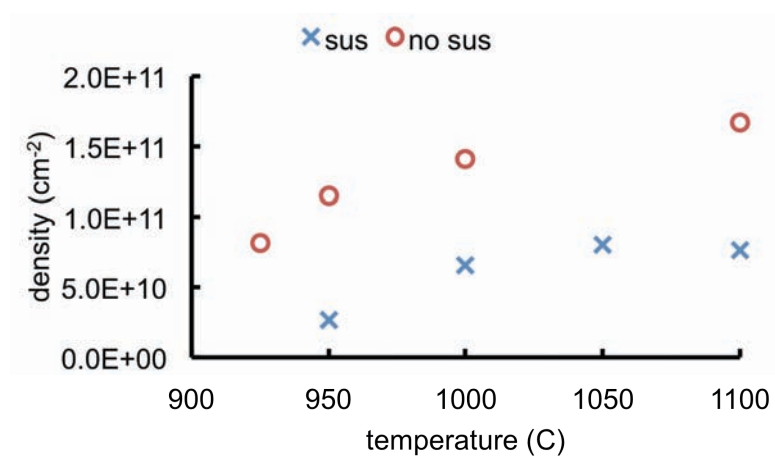


**Figure 2-17.** Density of pores as a result of annealing at different temperatures with and without the susceptor.



### 2.8.4 Annealing ramp rate

For many applications, such as filtration, it is desirable to have a membrane with pores that are round and have smooth edges. This morphology tends to be favored during pnc-Si formation when the ramp rate of the rapid thermal annealing process is at 50°C /s and above. Figure 2-18 shows a 15 nm thick pnc-Si membrane with 25 W of applied substrate bias and annealed at 1000°C with a ramp rate of 10°C/s, 50°C/s, and 100°C/s. At lower ramp rates, a wider pore size distribution is observed and many of the pores are irregularly shaped. At high ramp rates, such as 100°C/s, the width of the pore size distribution is reduced by nearly 50% due to the elimination of irregularly sized pores. A roundness index was calculated by estimating the pores as ellipses and the ratio of minor to major axis for each pore was taken and averaged over all pores. The ratio increases from 0.81 to 0.83 to 0.85 for ramp rates of 10°C/s, 50°C/s, and 100°C/s, respectively. Although these changes in ratio may seem small, they represent a significant shift in pore morphology as observed in the TEM micrographs. These results indicate that the majority of pore growth occurs during the ramp-to-temperature step, as discussed in the section on the effect of annealing time on morphology, so it is not surprising the ramp rate would have such a dramatic effect on pore morphology. This effect is also observed in a 30 nm thick membrane (Figure 2-19). Pore elongation at lower ramp rates is more apparent in a thicker film due to the increase in pore size due to the larger silicon volume.

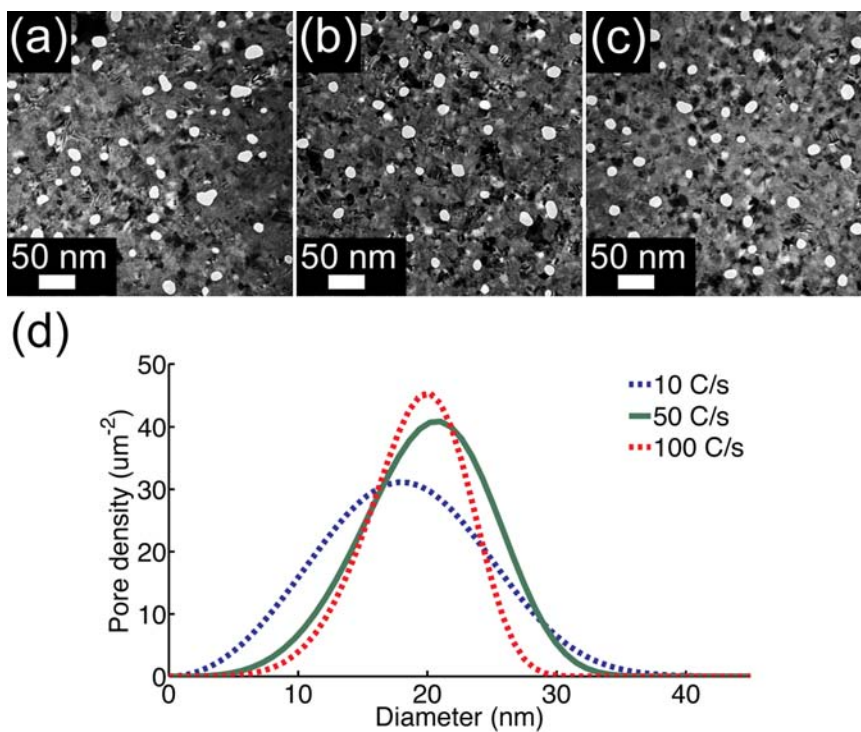


**Figure 2-18** (a) A 15 nm thick pnc-Si membrane annealed at 1000°C with a ramp rate of 10°C/s (b) 50°C/s and (c) 100°C/s. (d) The pore size distribution becomes increasingly narrow at higher ramp rates.

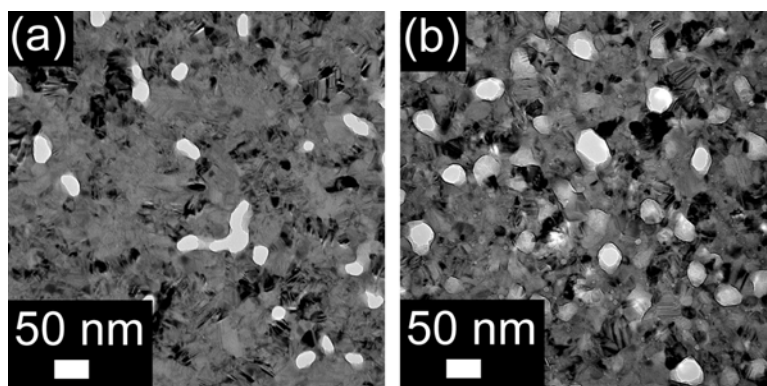


**Figure 2-19** (a) A 30 nm thick pnc-Si membrane annealed at 1000°C with a ramp rate of 10°C/s and (b) 100°C/s.

In order to explain why the ramp rate has such a dramatic effect on pore morphology, it is instructive to graph a simulated temperature versus time plot for several ramp rates (Figure 2-22). Nanocrystal silicon formation occurs between 600°C and 700°C. For lower ramp rates, the time spent in this temperature range is five to ten times longer as highlighted by the dashed lines. This leads to larger nanocrystalline silicon grain sizes. Consequently, the amorphous areas in between nanocrystals are much smaller in films annealed at a low ramp rate. As pores form at the amorphous/nanocrystalline interface, it is more likely that adjacent pores will merge, thus leading to irregularly shaped pores. In contrast, films that are annealed at a high ramp rate will have smaller initial grain boundaries, which allows for less pore merging and more regularly shaped pores.

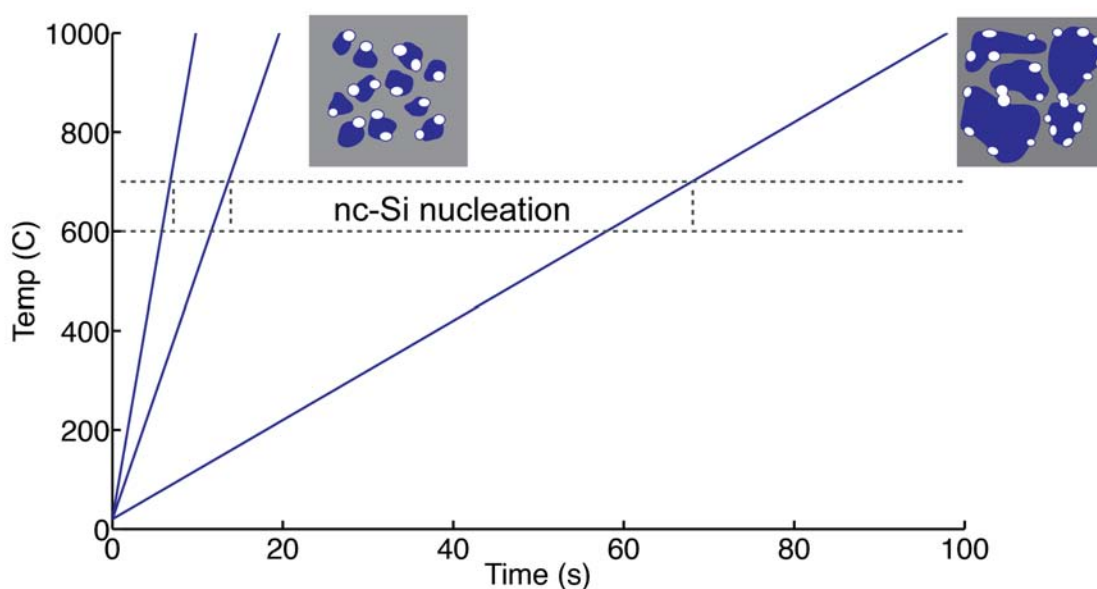


**Figure 2-20.** Plot showing three different simulated ramp rates (10°C/s, 50°C/s, 100°C/s). The cartoon insets show pores and nanocrystals in films annealed at low and high ramp rates. The purple and gray regions represent the nanocrystalline and

amorphous phase, respectively.

### 2.8.5 Silicon thickness

In an attempt to further increase the pore size, a 30 nm layer of silicon with 25 W of applied substrate bias was annealed using a susceptor inside the RTP. The hypothesis was that by increasing the silicon film thickness, crystal growth would be less confined between the Si/SiO<sub>2</sub> interfaces, allowing for larger grains and pores to form during crystallization. Figure 2-21 shows four 30 nm thick pnc-Si membranes that were annealed at temperatures between 1000°C and 1150°C for 60 s, with a ramp rate of 50°C/s. Indeed, by increasing the thickness of the silicon membrane an increase in average pore size was observed. Over the annealing temperatures studied, the average pore diameter and porosity ranged from 24 nm to 39 nm and from 0.7% to 3.9%, respectively. From these results, it is clear that increasing the film thickness yields larger pores, but the annealing temperatures required to induce pore formation also increase. RTP treatment below 1000°C did not produce through pores in 30 nm thick silicon and the nanocrystal size and density were small. Interestingly, the pore walls in a 30 nm thick membrane appear to consist of nanocrystalline facets, which are most apparent at the highest RTP temperature Figure 2-21 (d).

There is, however, an upper limit in the relationship of increasing pore size with silicon film thickness. As Figure 2-22 demonstrates, a silicon film thickness of 50 nm produces pores approaching 50 nm, but the pore density is much lower as compared to a

15 nm thick pnc-Si film. This effect originates from the fact that in thicker films, multilayers of nanocrystals begin forming thus increasing the probability that a pore will be occluded by a nanocrystal during the growth stage.

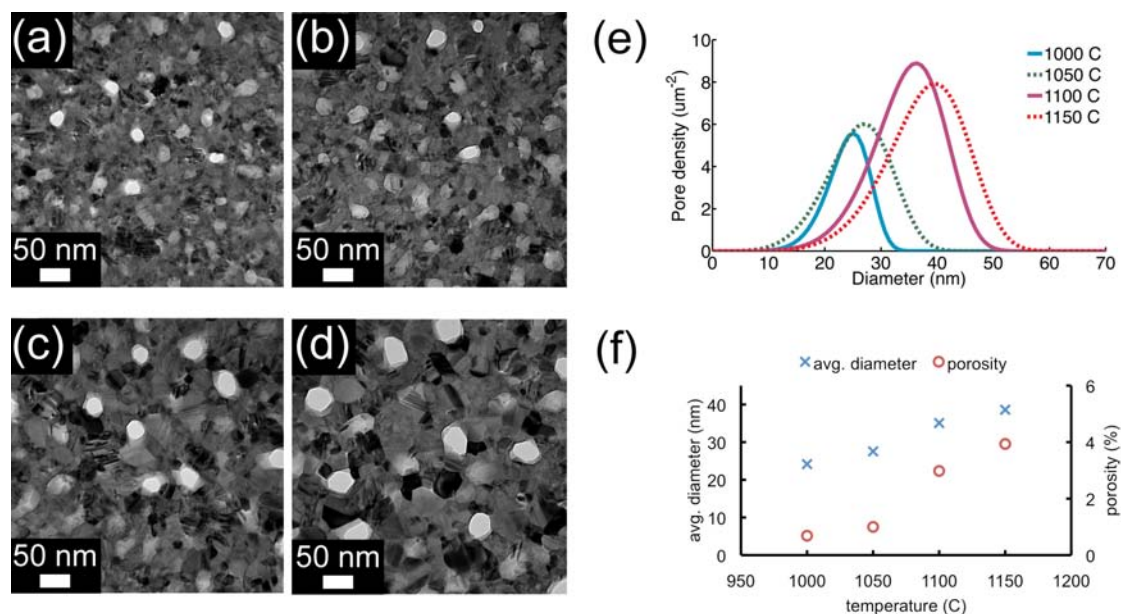


**Figure 2-21.** (a) – (d) TEM micrographs of 30 nm thick pnc-Si membranes that were annealed at 1000°C, 1050°C, 1100°C, and 1150°C. (e) The pore size distributions were calculated directly from TEM micrographs. (f) The average pore diameter and porosity is plotted for each annealing temperature.

Studies have shown that thin layers (< 10 nm) of amorphous silicon are highly stressed and difficult to crystallize [71, 72]. To investigate pore formation in very thin layers of silicon, a 9 nm a-Si film was deposited and annealed at 1000°C. TEM micrographs show that there are no detectable through pores at the resolution the images were taken (Figure 2-22). The crystal grain size in the image background is also small. In contrast, a 15 nm thick film shows clear pores with larger grain sizes (Figure 2-22(b)).

Based on these results, it would seem that the mechanism for pore formation is very closely related to the crystallization dynamics. That is, atoms are less mobile when confined by the closely spaced oxide layers causing an inhibition of pore formation.

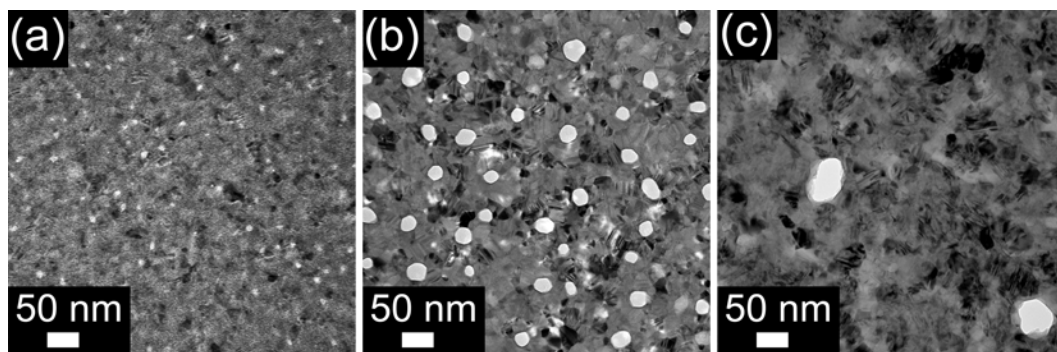


**Figure 2-22.** (a) A TEM micrograph of a 9 nm thick pnc-Si membrane. No through pores are identifiable at this resolution. The small white features are crystalline diffraction features. (b) A 15 nm thick pnc-Si membrane showing clearly defined through pores. (c) A 50 nm thick pnc-Si membrane exhibits larger pores at a lower density.

### 2.8.6 Substrate bias

During the deposition process, an rf bias may be applied to the substrate. By applying energy to the surface, incident atoms become more mobile and can re-arrange themselves in a lower stress state [73, 74]. Surface roughness is also reduced since high points in the film are redistributed. A large difference in morphology can be observed in samples deposited with and without substrate bias (Figure 2-23). Very few pores nucleate without the application of substrate bias. A 2 W substrate bias yields an order of magnitude increase in pore density (Figure 2-24). At 5 W of bias the average pore

diameter increases by 6 nm and the pore density decreases by 33%. A further increase in the substrate bias beyond 5 W decreases the pore size by 9 nm while the density remains constant. Beyond 5 W of bias, there are relatively small variations in the size and density of pores as compared to lower bias pnc-Si membranes. At 50 W of bias, the average pore size increases by approximately 2 nm while the pore density remains fixed.

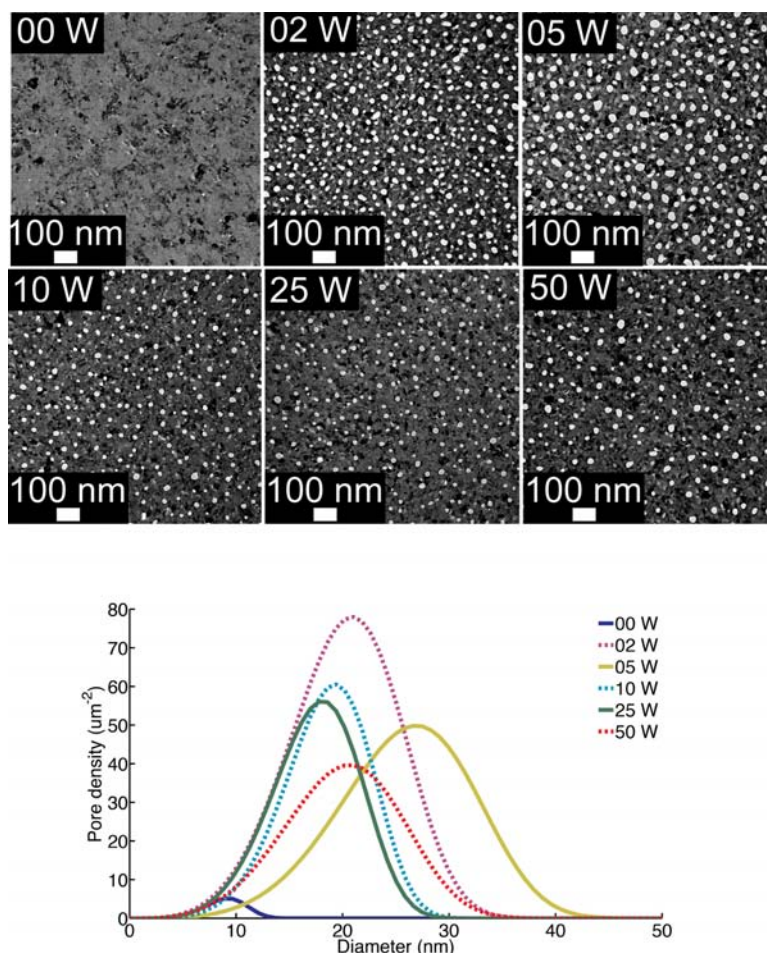


**Figure 2-23.** Pore size histogram and TEM micrographs of pnc-Si membranes deposited with various substrate biases. All membranes are 15 nm thick and annealed at 1000°C with a ramp rate of 100°C/s for 60 s.

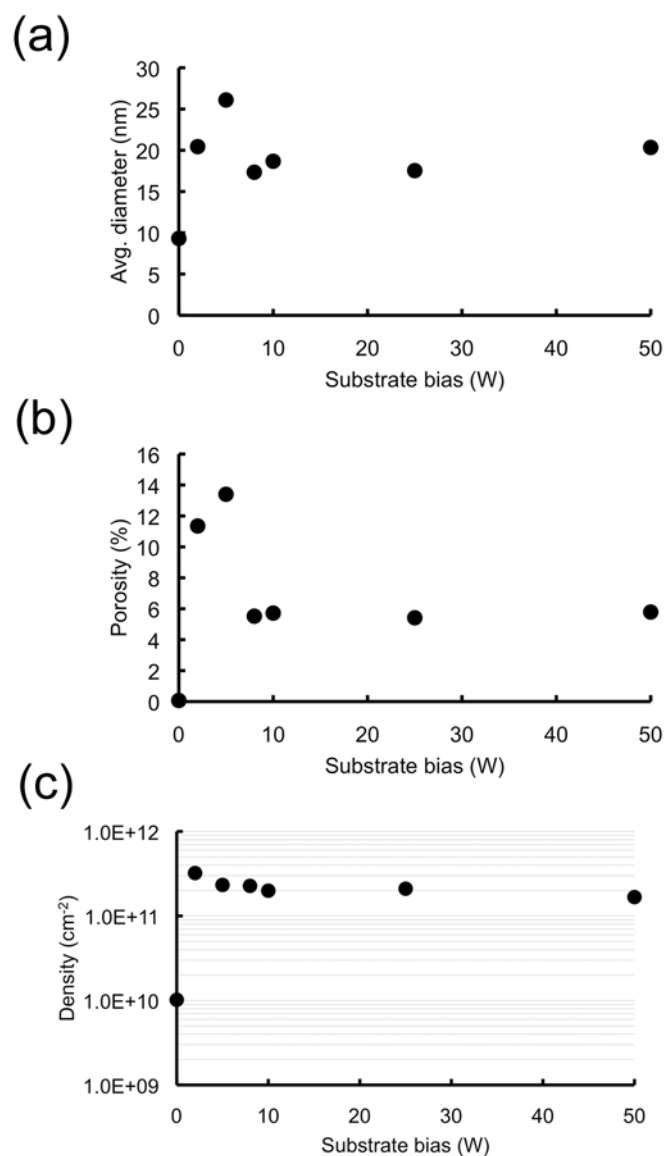


**Figure 2-24.** (a) Average pore diameter, (b) porosity, and (c) pore density of a 15 nm thick pnc-Si membrane deposited at various substrate biases and annealed at 1000°C with a ramp rate of 100°C/s for 60 s.

In comparing an annealing temperature series between films deposited with 5 and 25 W substrate bias, it is apparent that the low bias film yields larger pores along with higher porosities (Figure 2-25).



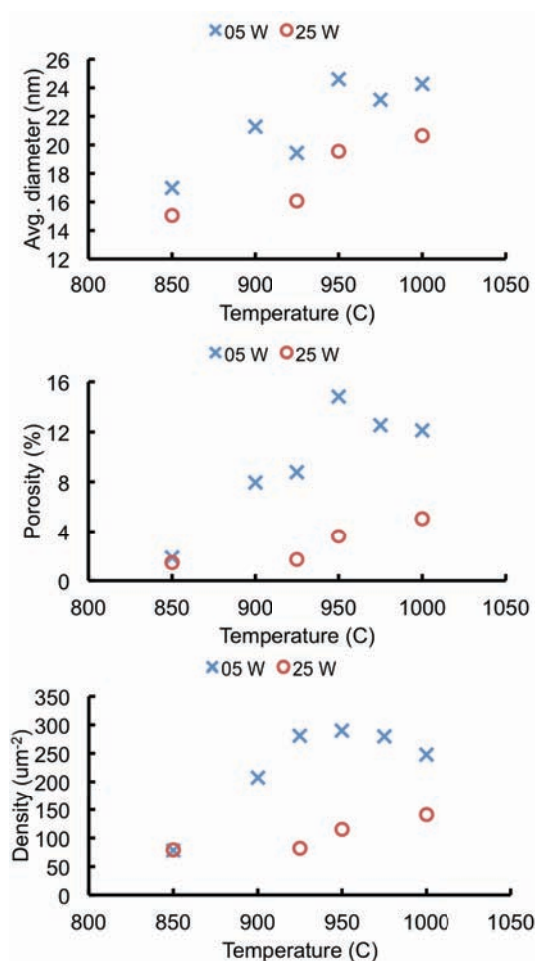


**Figure 2-25.** Plots comparing the average diameter, porosity, and density of pores of pnc-Si membranes deposited with a substrate bias of 5 and 25 W versus annealing temperature.

The increase in porosity stems from a higher pore density in the 5 W substrate bias sample.

From these results, it is clear that pore morphology is very sensitive to the application of a substrate bias. This is not surprising considering the density of the amorphous silicon and quality of the silicon-silicon dioxide interface are both affected

by the substrate bias. This will have strong consequences during the crystallization and pore formation process, which will be discussed in section 3.5.

### 2.8.7 Deposition temperature

Deposition temperature can greatly affect the microstructure of a thin film. 15 nm thick pnc-Si membranes deposited with 25 W of applied substrate bias at various temperatures from room temperature to 300°C were investigated (Figure 2-26). The morphology of these membranes was very similar with the exception of the film deposited at 300°C. The average pore diameter of this particular membrane was significantly lower than the other samples. A likely explanation is that at 300°C, there is enough surface energy to form nanocrystals *in situ* which inhibits the pore formation process during the subsequent annealing step. Although 300°C is much lower than the crystallization of silicon, it should be noted that this is the reading on the thermocouple controller and does not reflect the true temperature at the film surface. In reality, the effective temperature on the wafer can be much higher. Spectroscopic ellipsometry of the amorphous silicon deposited at these various temperatures shows that the 300°C film has a lower index of refraction than the other samples (Figure 2-27, Figure 2-28).

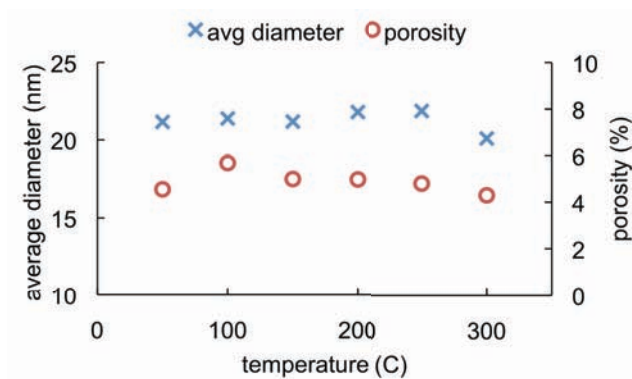


**Figure 2-26.** Average diameter and porosity of a 15 nm-thick pnc-Si membrane deposited at various temperatures and 25 W substrate bias. The membranes were all annealed at 1000°C with a ramp rate of 100°C/s.

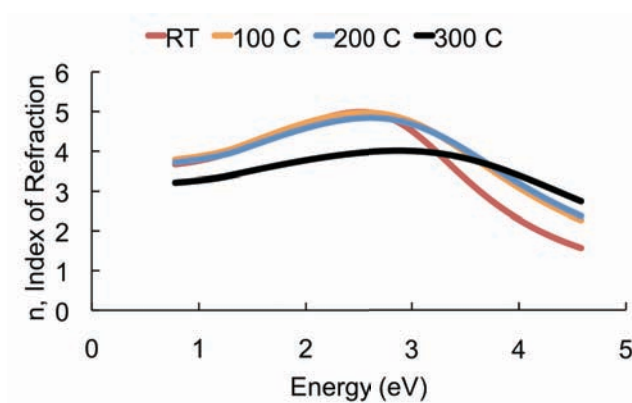


**Figure 2-27.** Index of refraction of amorphous silicon films deposited at different temperatures as measured by spectroscopic ellipsometry.

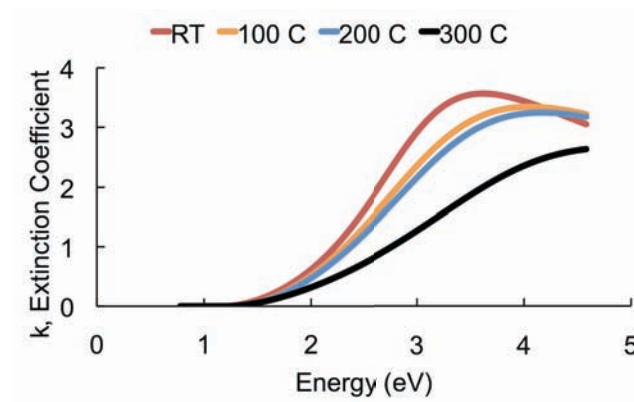


**Figure 2-28.** Extinction coefficient amorphous silicon films deposited at different temperatures as measured by spectroscopic ellipsometry.

### 2.8.8 Alternative deposition techniques

In addition to physical vapor deposition (PVD) of silicon and silicon dioxide, alternative methods for thin film deposition have been explored, such as plasma enhanced chemical vapor deposition (PECVD). Pre-patterned wafers were shipped to Rogue Valley Microdevices (Medford, OR) where 20 nm / 15 nm / 20 nm of  $\text{SiO}_2$  / a-Si:H /  $\text{SiO}_2$  were deposited by PECVD on substrates described in section 2.3. The wafers were annealed at 1000°C with a ramp rate of 100°C/s. Interestingly, the PECVD deposited membrane film did not exhibit any void formation, whereas the PVD deposited membrane film showed open pores when processed identically (Figure 2-29).

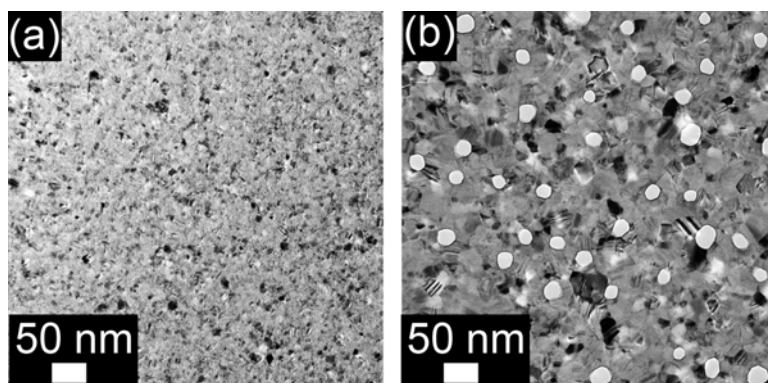


**Figure 2-29.** (a) TEM micrograph of a PECVD deposited membrane film and a (b) PVD deposited 15 nm membrane film.

Spectroscopic ellipsometry revealed that the PECVD films had a lower refractive index than their PVD counterpart (Figure 2-30). The suppressed index is an indication of a difference in the a-Si composition and density that affects the pore formation kinetics. The influence of hydrogen bonding to the silicon is also likely to play a role in the difference in morphology due to structural relaxation differences during annealing of hydrogenated films [75].

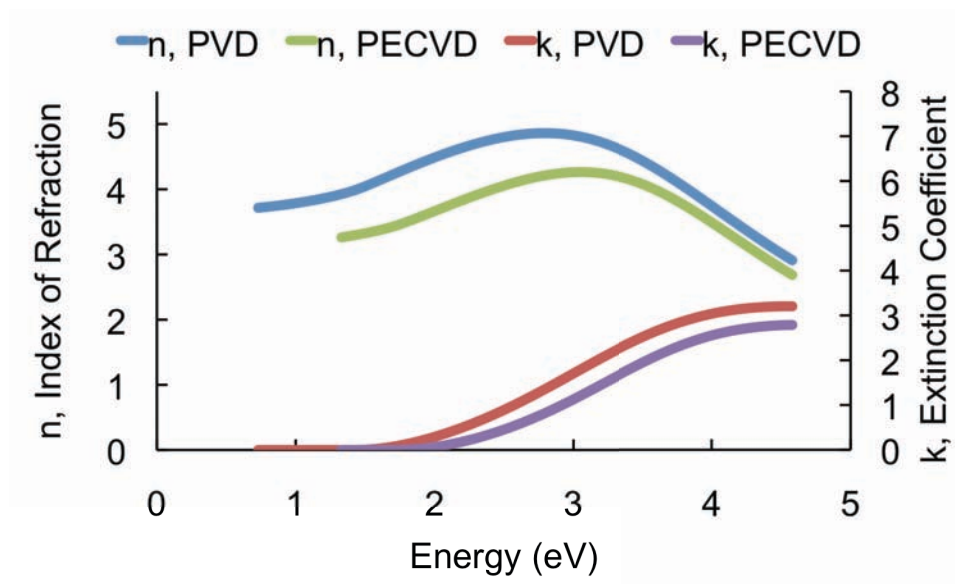


**Figure 2-30.** Index of refraction and extinction coefficient versus photon energy of a PVD and PECVD deposited amorphous silicon film. Some energies were truncated in the PECVD measurement due to anomalous absorption in the infrared.

## 2.9 Reproducibility

The membrane fabrication process is highly reproducible. A set of wafers that were deposited and annealed under identical conditions yielded very similar morphologies (Figure 2-31). From a manufacturing standpoint, this is reassuring and confirms that there are no unstable parameters that affect the pore formation mechanism.

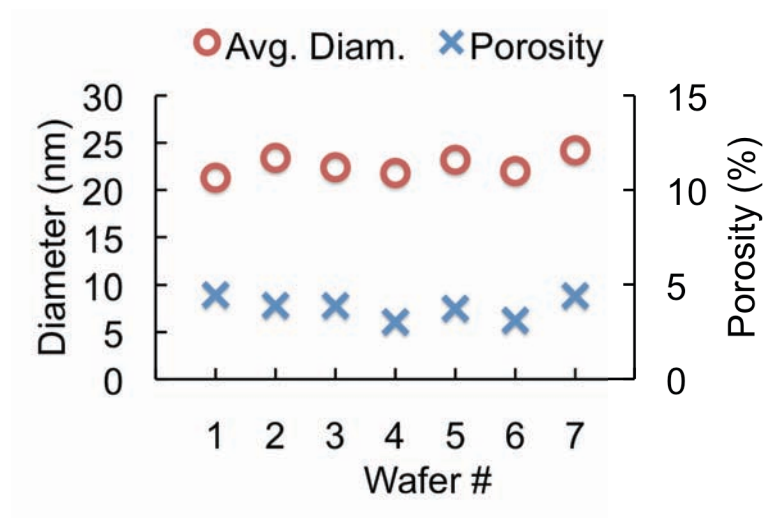


**Figure 2-31.** Pore statistics of seven wafers that were processed identically. The standard deviation of the average diameter and porosity are 0.6 nm and 0.8%, respectively.

## 2.10 Variations in morphology

There are inevitably variations in membrane morphology across a wafer due to small non-uniformities in the film thickness as well as fluctuations in the thermal processing (i.e. rapid thermal anneal). Nine samples across the wafer were analyzed using TEM and pore processing routines. The average diameter, porosity, and density of each membrane were calculated (Figure 2-32).

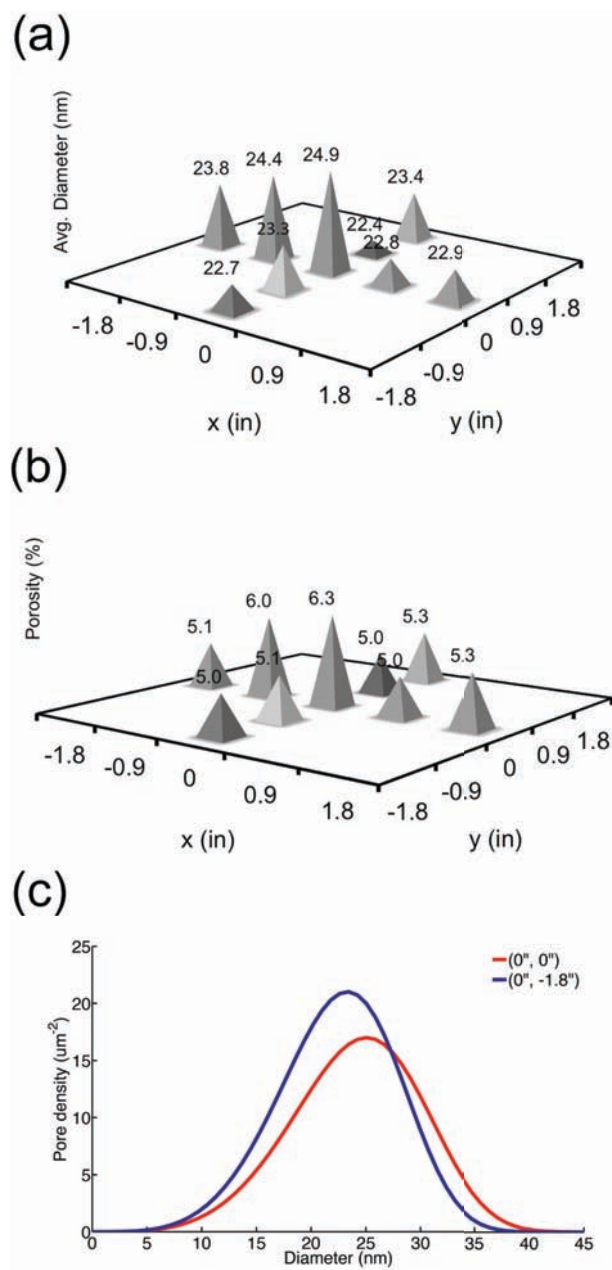


**Figure 2-32.** (a) The average diameter and (b) porosity of pnc-Si membranes from nine different positions on a 4-inch wafer. (c) A pore size histogram comparing the maximum and minimum points on the wafer.

It would seem that the center of the wafer yields slightly larger pores, which results in a higher porosity. This is most likely due to a slower rate of thermal dissipation at the



center of the wafer during the rapid thermal annealing process as compared to the membranes near the edge. The effective temperature at the center of the wafer may in fact be significantly higher thus leading to larger pores. The standard deviation of the average diameter and porosity are 0.8 nm and 0.5%, respectively.

## **2.11 Membrane defects**

### **2.11.1 Pinholes**

Because pnc-Si membranes are a promising material for molecular separation, it is essential that pinhole defects (typically 1  $\mu\text{m}$  – 10  $\mu\text{m}$  in size) be eliminated or at least minimized (Figure 2-33). These defects stem from several sources during fabrication process. First, it is imperative that the wafer surface be clean (see section 2.3) of particulates before the thin film deposition step. Any particles that remain on the surface will penetrate the thin protective oxide layer (20 nm) and allow the EDP etchant to readily attack the silicon film creating large micron-sized holes in the free-standing membrane.

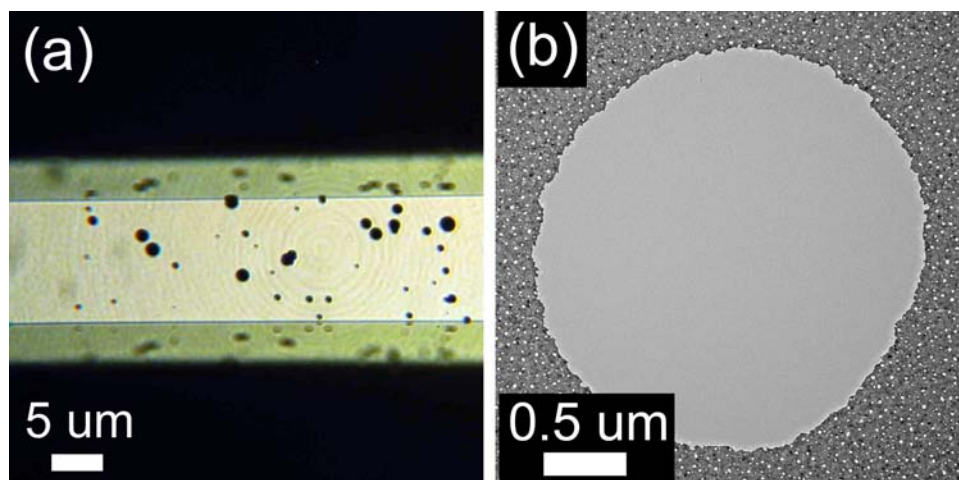


**Figure 2-33.** (a) Bright-field optical image of a pnc-Si membrane with a high density of pinhole defects (black spots). (b) TEM image of a single pinhole defect. The small white dots in the gray background are nanopores.

A second source of particle contamination originates from the sputter deposition tool. Although the tool is in a “sputter up” configuration where the wafer surface to be deposited on faces the bottom of the chamber, stray contaminants may become charged in the plasma and accelerated towards the substrate. These particles can be observed in dark field optical microscopy (Figure 2-34). Particle counts tend to increase as layers of film build-up on the parts that are in line of sight of the plasma. This is because flaking eventually takes place, which releases a large amount of particles into the chamber. In order to combat this effect, rigorous cleaning of all the parts that “see” plasma is performed after a series of depositions. The metal parts are subjected to a bead blast to remove film buildup followed by an ultrasonic bath and bake out in a vacuum oven.



**Figure 2-34.** Dark field optical image of a film with a high density of particle contaminants. The particles act as scatterers, which appear as bright dots in the dark field imaging mode.

## 2.12 Conclusions

In this chapter, a review of the fabrication of porous nanocrystalline silicon has been performed and it has been determined that the manufacturing process is robust and scalable. By changing the silicon thin film deposition conditions, such as thickness and substrate bias, the pore size and density can be modified. It has been demonstrated that the thermal treatment conditions such as soak temperature, time, and ramp rate have important consequences on the pore morphology. By tuning these fabrication parameters, pore size cut-offs from 10 nm to 80 nm may be manufactured with membrane porosities approaching 15%. In the next chapter, the kinetics of pore formation as a consequence of silicon crystallization will be studied in order to better understand why the parameters discussed in this chapter affect pore properties.

## Chapter 3. Mechanisms of pore formation

### 3.1 Introduction

A basic understanding of the physics of pore formation in porous nanocrystalline silicon is crucial to tailoring the pore properties for specific membrane applications. In this chapter, pore formation as a consequence of the thermal crystallization of a thin film of amorphous silicon will be explored. Key factors that drive the pore formation process will be identified. Lastly, a phenomenological model of pore formation based on prior observations on phase transformations in polycrystalline materials will be developed.

### 3.2 Pore formation during silicon crystallization

It has been reported that amorphous silicon makes the phase transition to polycrystalline at annealing temperatures as low as 500°C [76]. The majority of prior work has focused on much thicker films (50 nm – 200 nm) since much of the field has been driven by the potential use of *polycrystalline* silicon in semiconductor devices [77, 78]. By limiting the silicon thickness to < 30 nm, crystal growth is confined to a single layer. As a result, the crystals that emerge are *nanocrystalline* (< 50 nm). The onset of crystallization in a 15 nm thick silicon film occurs at approximately 700°C using a rapid thermal process. At this temperature the formation of nanocrystalline “islands”

surrounded by an amorphous matrix is observed (Figure 2-6). Pores preferentially form along the amorphous/crystalline interfaces creating a “necklace” pattern of pores. As silicon atoms migrate to form nanocrystals, they leave vacancies behind. A critical number of vacancies will result in a “pore”. Annealing at a higher temperature (1000°C) completely crystallizes the film and a high density of pores can be achieved. The same necklace pattern is also observed in the fully crystallized film. A range of nanocrystal orientations has been observed in pnc-Si membranes, but  $\langle 111 \rangle$  oriented crystals seem to appear most frequently (Figure 3-1). This observation has also been documented in a previous independent study on polycrystalline films formed by rapid thermal annealing of amorphous silicon [79].

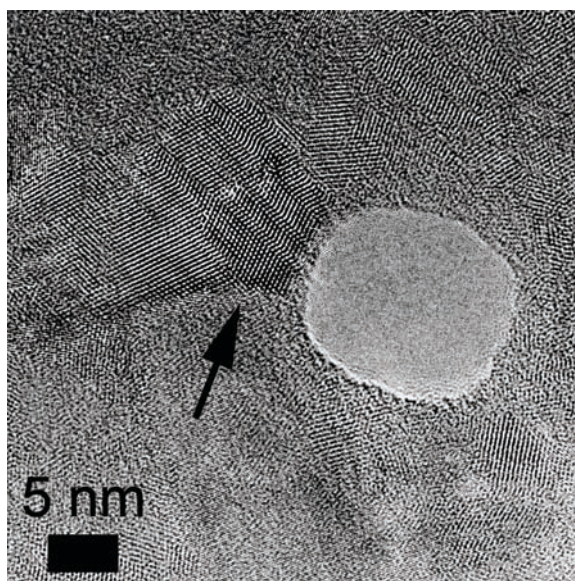


**Figure 3-1.** High-resolution TEM image of a nanopore with an adjacent nanocrystal. The lattice spacing was measured to be 3.1 Å, consistent with a  $\langle 111 \rangle$  oriented crystal.

Just as the crystallization of amorphous silicon can be described in two stages, nucleation and growth, so too can pore formation in pnc-Si. In the following sections, the mechanisms by which pore nucleation and growth is perturbed will be considered.

### **3.3 Crystallization of amorphous silicon**

#### **3.3.1 Nucleation and growth**

The solid phase crystallization (SPC) of amorphous silicon begins with the nucleation of crystallites followed by a subsequent growth stage. As deposited amorphous silicon is in a metastable state. It is modeled as a continuous random network (CRN) in which each atom has four other silicon atoms covalently bonded to it. Previous studies have shown that as-deposited amorphous silicon contains defects in the structure such as point defects and dangling bonds [75]. These defects are sites for nanocrystal nucleation during a high temperature annealing process [80]. Once a nanocrystal nucleates, growth proceeds in a step-like manner as depicted in Figure 3-2. Growth is fastest in the  $\langle 100 \rangle$  direction and slower in the  $\langle 110 \rangle$  and  $\langle 111 \rangle$  directions by a factor 2.5 and 25, respectively [81]. The difference in growth rates is derived from the fact that only one Si atom is required to form the two bonds necessary for incorporation onto the (100) nanocrystal plane. In contrast, clusters of two Si atoms are required for growth on the (110) plane and three atom clusters for the (111) plane.

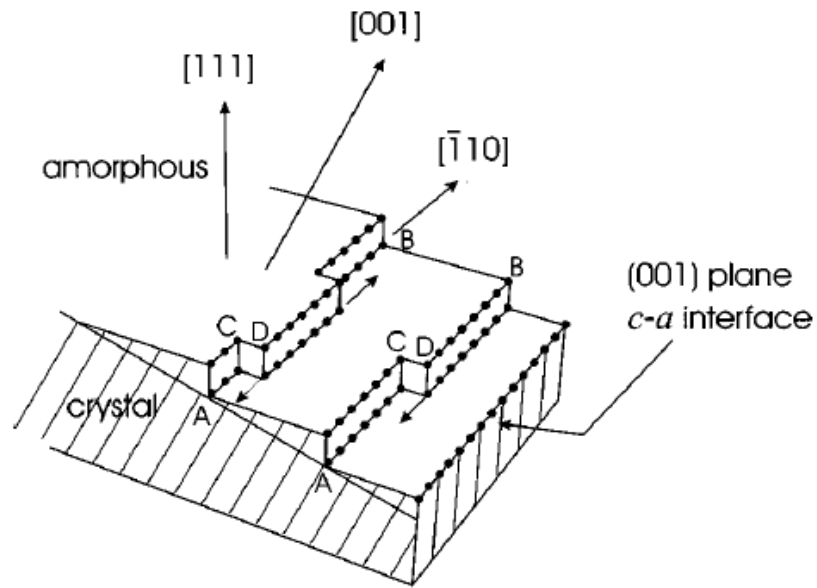


**Figure 3-2.** Nanocrystal growth occurs in a step-wise manner [80]. Si atoms migrate to form “kinks” (CD) and growth proceeds along the  $[1\bar{1}0]$  direction indicated by the arrows. The nanocrystalline silicon facets are defined by the slowest growth direction,  $[111]$ .

An important defect structure that results during crystallization is a microtwin (Figure 3-1). These features form at the amorphous-nanocrystalline interface on the  $(111)$  surface [81]. Because three-atom clusters are required for growth on this plane, two bonding configurations are possible. Microtwins develop when a three-atom cluster forms on the  $(111)$  plane with a stacking order that is the reverse of the base nanocrystal. Growth along a microtwin ledge is also enhanced due to the decreased number of atoms (from three atoms to two) required to “join” the nanocrystal (Figure 3-3).

Although no literature exists documenting void formation in silicon, voids have been observed near these defect structures in polycrystalline copper [82]. Interestingly, pores are frequently accompanied by microtwin features in TEM micrographs of pnc-Si as well (Figure 3-3). In section 3.5, a detailed description of the pore formation process will be presented.

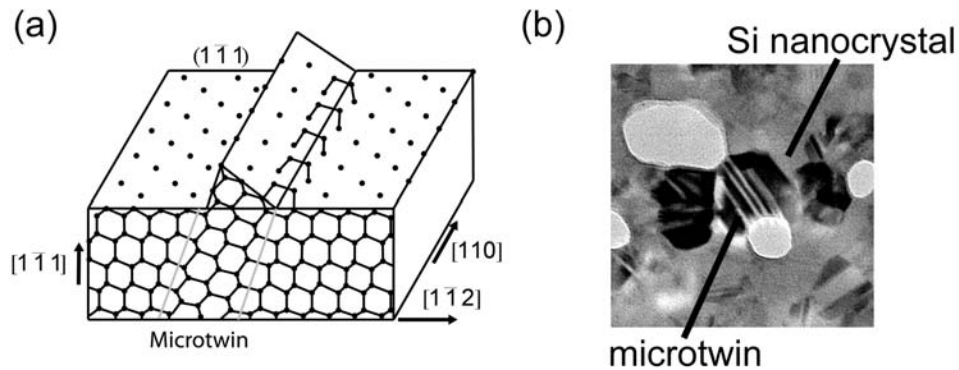


**Figure 3-3.** (a) A schematic depicting microtwin growth. Further nanocrystal growth can nucleate along the microtwin ledge with the addition of two atom clusters [81]. (b) TEM micrograph showing pores adjacent to Si nanocrystals and microtwin defects.

### 3.3.2 Thermodynamic quantities

Silicon nanocrystal nucleation and growth can be described by rate equations using thermodynamic quantities [83]:



$$v_g = \delta v \exp\left(\frac{\Delta S_m}{K}\right) \exp\left(-\frac{\Delta h_m}{KT}\right) \left[1 - \exp\left(\frac{\Delta g'}{KT}\right)\right],$$

**Equation 3-1**

$$n = Nv \exp\left(-\frac{\Delta S_m}{K}\right) \exp\left(-\frac{\Delta G_c}{KT}\right) \left[1 - \exp\left(\frac{\Delta g'}{KT}\right)\right].$$

**Equation 3-2**

The growth rate,  $v_g$  and nucleation rate,  $n$ , are written in terms of the difference in Gibbs energy per atom in the crystalline and amorphous phases:  $\Delta g' = \Delta h' - T\Delta S'$ , where  $\Delta h'$  and  $\Delta S'$  are the change in enthalpy and entropy, respectively, and  $T$  is the temperature of the system, and  $K$  is Boltzmann's constant. The barrier an atom must overcome to transition from the amorphous to crystalline phase can be written as a migration energy term:  $\Delta g_m = \Delta h_m - T\Delta S_m$ . In the rate equations,  $\delta$  represents the atomic jump distance,  $v$  is the atomic vibrational frequency, and  $N$  is the number of atoms. The energy  $\Delta G_c$  is the amount needed for the formation of a crystal with the critical number of atoms:

$$m_c = \left(\frac{2\Delta G_c}{\Delta g'}\right)^{2/3}.$$

**Equation 3-3**

Zellama *et al.* studied the crystallite growth rate by annealing amorphous silicon at different temperatures and determined the crystalline fraction using conductivity measurements. It was confirmed that the growth rate of crystals is an Arrhenius process, that is, the logarithm of the crystallization rate is linearly related to the inverse of temperature (Figure 3-4).

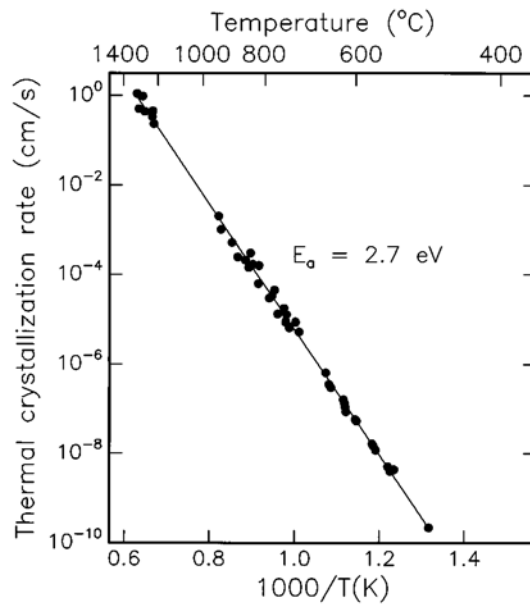


**Figure 3-4.** Arrhenius plot of the growth rate of silicon crystallization [80].

Applying the Arrhenius equation, which describes the rate of a reaction as a function of temperature, to a plot such as Figure 3-4 will lead to the activation energy of the reaction,  $E_a$ :

$$k = Ae^{-\frac{E_a}{k_B T}},$$

**Equation 3-4**

where  $A$  is a constant of proportionality,  $k_B$  is the Boltzmann constant, and  $T$  is the temperature.

### 3.4 Pore formation activation energies

By applying a similar analysis introduced in section 3.3, the activation energy needed for pore nucleation and growth can be found. A pore nucleation rate was calculated by looking at the density of pores in 15 nm and 30 nm thick pnc-Si membranes that were annealed at temperatures between 700°C and 1100°C for 60 s. Figure 3-5 shows that pore nucleation is indeed an Arrhenius process, similar to silicon crystallization. By applying Equation 3-4, an activation energy for pore nucleation can be extracted. The activation energy for pore nucleation in a 15 nm and 30 nm film is 0.55 eV and 0.69 eV, respectively. It is not surprising that the thicker film has a higher activation energy since a void must grow twice as large before it forms a pore in the 30 nm membrane when compared to a 15 nm membrane.

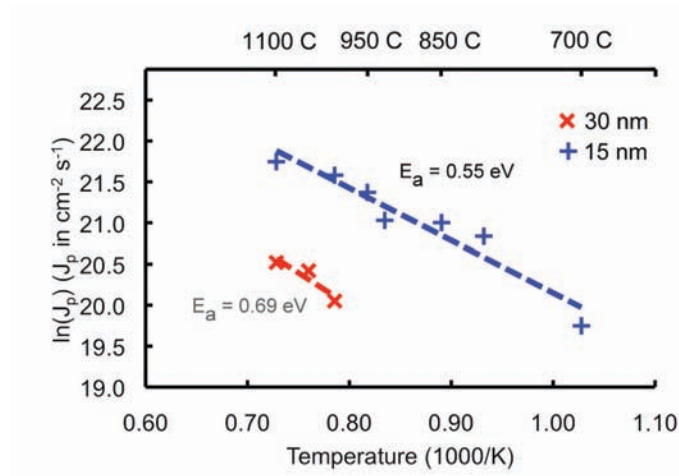


**Figure 3-5.** Arrhenius plot of the pore nucleation rate,  $J_p$  for a 15 nm and 30 nm thick pnc-Si membrane. The activation energy for pore nucleation is calculated using Equation 3-4. The 15 nm membrane has a pore nucleation activation energy of 0.55 eV and the 30 nm membrane has an activation energy of 0.69 eV.

A similar analysis was performed to calculate the pore growth velocity. The average diameter of several 15 nm and 30 nm pnc-Si membranes annealed at temperatures between 700°C and 1100°C for 60 s were recorded. The growth rates were calculated from taking the average diameter and dividing it by the duration of anneal. Both the 15 nm and 30 nm membrane had very similar pore growth activation energies of approximately 0.28 eV. This is to be expected since the material composition between the two thicknesses is identical. Thus, as expected the pore growth mechanism is independent of membrane thickness.

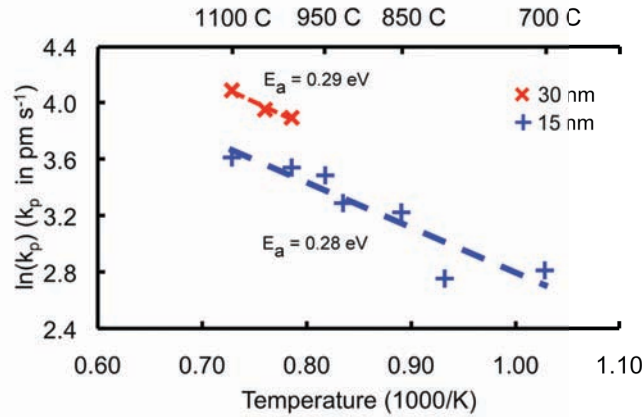


**Figure 3-6.** Arrhenius plot of the pore growth rate,  $k_p$  for a 15 nm and 30 nm thick pnc-Si membrane. The activation energy for pore growth is calculated using Equation 3-4. The 15 nm membrane has a pore growth activation energy of 0.28 eV and the 30 nm membrane has an activation energy of 0.29 eV.

From these empirical calculations of pore nucleation and growth activation energies, a better understanding of the thermodynamic requirements for pore formation has been achieved.

### 3.5 Factors influencing nucleation and growth

Nucleation of nanocrystals occurs mostly at the amorphous silicon-silicon dioxide interface [80, 84]. It is then reasonable to assume that pore nucleation occurs at the interface shortly after nanocrystals begin to form. As was noted in section 2.8.6, application of a substrate bias during the amorphous silicon deposition step greatly affects the resulting pnc-Si morphology. Without a substrate bias, the a-Si/SiO<sub>2</sub> film interface is rough with intermixed areas of silicon and silicon dioxide. This hinders

nanocrystal nucleation at the interface and thus severely limits pore formation. Additionally, the presence of dangling bonds in the bulk amorphous layer serves as nanocrystal nucleation sites which quickly grows into one another eliminating the possibility of pores to penetrate through the entire silicon layer.

One important consequence of a substrate bias is that “high points” created by impinging Si atoms become mobile and they are able to rearrange into a lower free energy state. Prior studies have also shown that a substrate bias reduces the dangling bond density and oxygen contamination in an amorphous silicon film deposited by physical vapor deposition, thus yielding a higher quality material [85]. Therefore, applying a substrate bias will create a smoother interface between layers and reduce the number of point defects in the bulk of the film. Table 3-1 shows the dc voltage measured across the substrate as a function of applied substrate bias power.

**Table 3-1.** Voltage across substrate as a function of substrate bias power

Power	Voltage
0 W	0 V
2 W	20 V
10 W	37 V
25 W	64 V
50 W	100 V

The data presented in section 2.8.6 showed that substrate bias produces a large non-linear response in pore size and density (Figure 2-24). The low pore population with no applied substrate bias is attributed to the rough Si-SiO<sub>2</sub> interface and large defect

density in the bulk of the film, which inhibits pore nucleation (Figure 3-7). The high defect density leads to Si nanocrystal nucleation throughout the film thickness, thus the likelihood of a void spanning the entire thickness of the film is greatly reduced as grains very rapidly grow into one another. A low substrate bias (2 W) reduces the bulk defects but still leaves a finite amount of point defects at the interface such that void nucleation can proceed. Higher biases (> 5 W – 50 W) produce low defect densities in both the bulk and interface regions. The reduction in point defects at the interface reduces void nucleation sites, which supports the observation of a sudden decrease in pore density at biases greater than 2 W. Interestingly, the largest pore sizes are seen at a 5 W bias and decrease with increasing bias. It is possible that higher power biasing over-densifies the amorphous silicon, which impedes the mobility of Si atoms during crystallization and subsequently slows pore growth. At 50 W however, there is a significant increase in average pore diameter. This may be due to a finite amount of argon implantation into the silicon layer, which adds an additional growth mechanism. Interestingly, a prior study has shown amorphous Si films that were implanted with Ar showed an increase in microtwin density after crystallization [86]. A higher population of microtwins would provide Si atoms with an increased number of “paths” to move and create more vacancies and therefore increase pore sizes.

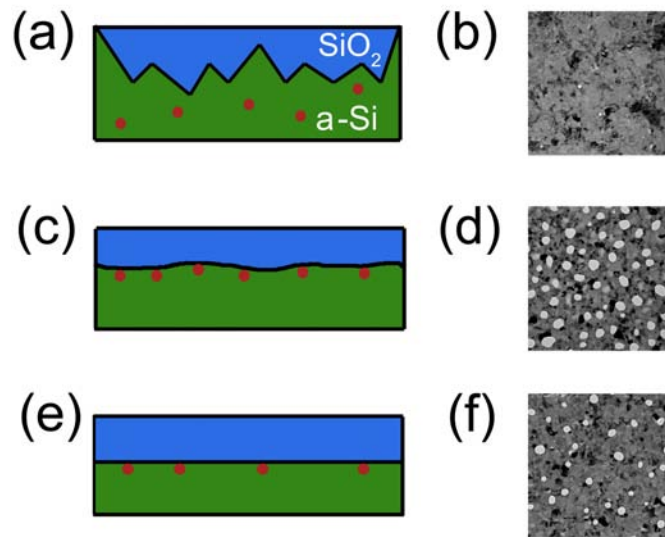


**Figure 3-7.** Cartoon depiction of the SiO<sub>2</sub>-Si interface with different substrate bias powers during the silicon deposition and the associated TEM micrographs. (a) - (b) 0 W, (c) - (d) 5 W, and (e) - (f) 50 W. The red dots indicate the location of nanocrystal nucleation sites.

In order to confirm the reduction in interface roughness with the application of a substrate bias during deposition, atomic force microscopy was performed on three samples of amorphous silicon with different amounts of bias: 0 W, 5 W, and 50 W. The amorphous silicon samples were prepared by depositing a three-layer stack of silicon dioxide-amorphous silicon-silicon dioxide with thickness of 15 nm, 20 nm, and 15 nm respectively. The top oxide layer was removed with buffered oxide etchant prior to the AFM measurement.



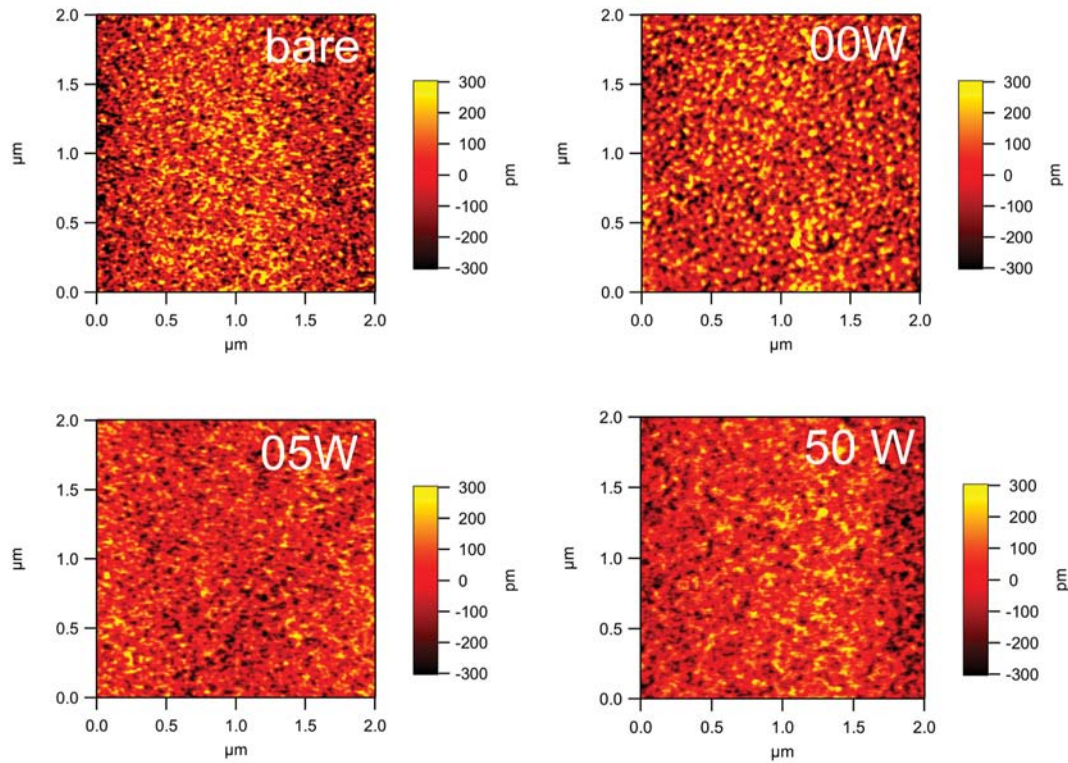


**Figure 3-8.** Atomic force microscopy scans of a bare wafer and three amorphous silicon films deposited with different amounts of substrate bias.

The zero bias amorphous silicon has an RMS roughness similar to that of a bare wafer ( $1.3 \text{ \AA}$ ). The 5 W and 50 W amorphous silicon samples have a lower RMS roughness, as expected, of  $1.0 \text{ \AA}$ . These results support the claim that a rough interface will suppress nucleation, which is why low porosity is observed with zero bias. The 5 W condition decreases the interface roughness while maintaining a critical level of point defects in the Si, which nucleates pore growth. High bias maintains the smooth interface, but reduces the point defects.

## 3.6 Stages of pore formation

To date, there have been only a few instances in literature that discuss void formation in polycrystalline materials [82, 87, 88]. In these studies, void formation is described as a result of stress relaxation from a thermal annealing process in which point defects in a material migrate along twin boundaries to grain boundaries [89]. Because prior work has focused mainly on thicker films ( $> 100$  nm), multilayers of grains form and the probability of observing a through pore is low. In the case of pnc-Si, if Si atoms are mobile enough during crystallization process and the nanocrystal growth is restricted to a single layer, it is possible for voids to span the entire thickness of the film leading to a through pore.

### 3.6.1 Pore nucleation

The location of nanocrystal nucleation is critical to the pore formation process. If the majority of nucleation occurs in the bulk of the amorphous silicon, crystal grains will quickly grow into each other thus reducing the probability of a pore extending through the entire thickness of the film. On the other hand, if the majority of nanocrystal nucleation occurs at the amorphous silicon-silicon dioxide interface, void formation may initiate at the Si-SiO<sub>2</sub> interface (Figure 3-9). A similar dewetting phenomena has been observed in silicon-on-insulator systems [87]. In the case of pnc-Si, the silicon layer is confined by two silicon dioxide interfaces. As Si atoms continue move to form nanocrystals, they leave more vacancies behind and eventually a void will span both Si-

$\text{SiO}_2$  interfaces creating a through pore. The nanocrystal-pore structure is maintained due to a reduction in the stress and overall free energy of the system.

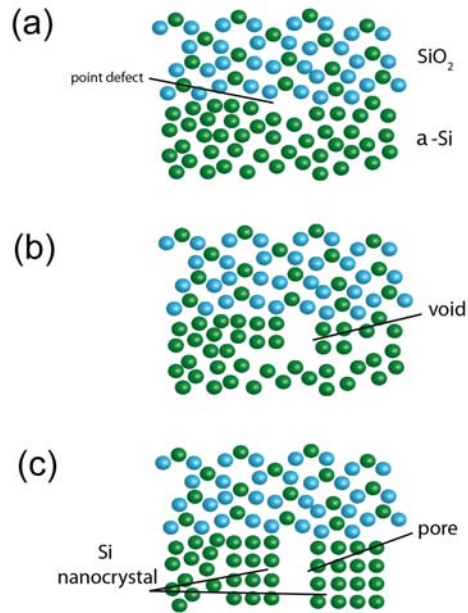


**Figure 3-9.** Simplified schematic of pore nucleation. The green and blue balls represent silicon and oxygen clusters, respectively. **(a)** Nanocrystal nucleation occurs at the  $\text{Si}/\text{SiO}_2$  interface. **(b)** As the nanocrystal grows in size, Si atoms leave vacancies that become voids. **(c)** Voids that penetrate the film thickness become pores.

### 3.6.2 Pore growth

Once a pore nucleates, growth proceeds in conjunction with Si nanocrystal formation. As the Si atoms move to join adjacent nanocrystals, they leave more vacancies behind thus enlarging a pore (Figure 3-10). Pore growth stops when all the amorphous silicon is converted to a nanocrystalline state. The size of a pore is ultimately determined by how mobile a Si atom is during the crystallization process. This is affected by the energy made available during the annealing step and the silicon thin film

quality and composition. In section 2.8, it was shown that pore size increases with higher annealing temperatures and longer annealing time due the increased energy made available for nanocrystal and pore growth. At lower temperatures, only a few small pores nucleate. This is because the Si atom mobility is restricted during low temperature anneals. It is also speculated that the concentration of amorphous material at the nanocrystalline silicon grain boundaries is higher for membranes with lower porosity. As more energy is made available at higher annealing temperatures, Si mobility increases and pores start to grow in size and the amorphous content is converted into nanocrystalline grains. The density of microtwins surrounding a pore will also affect growth, as these features increase the Si atom mobility during crystallization.

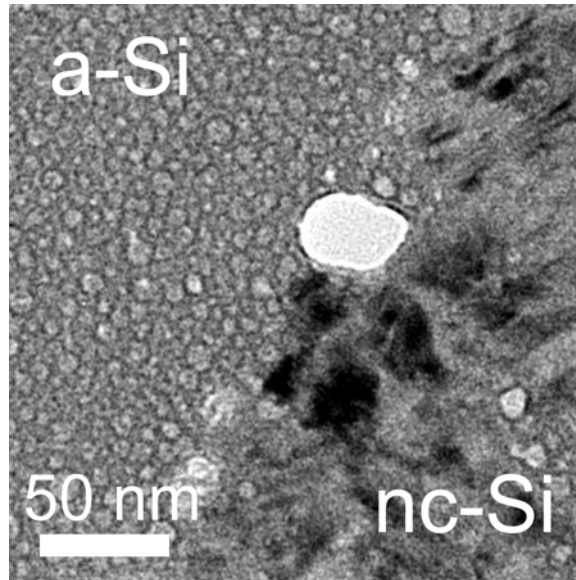


**Figure 3-10.** TEM micrograph showing a pore at the amorphous-nanocrystalline interface. Pores nucleate and grow as atoms in the amorphous phase become mobile and are converted into nanocrystals.

### 3.7 The role of film stress and strain on pore formation

Film stress and strain has been shown to greatly affect the crystallization of amorphous silicon [71, 90]. Consequently, it is reasonable to assume that it plays a role in the formation of pores in pnc-Si. The majority of strain in a thin film is caused by the thick bulk substrate it is anchored to. In this section, the importance of the substrate in aiding the pore formation process will be shown. That is, the strain induced by the bulk silicon is a necessary condition for pore nucleation and growth. Up to this point, only

films crystallized when still anchored to a thick substrate have been investigated. Here, the resulting membrane morphology under two cases will be explored: 1) annealing a free-standing membrane with no protective oxide and 2) annealing a free-standing membrane with the protective oxide. The process flow for these two conditions is illustrated in Figure 3-11.

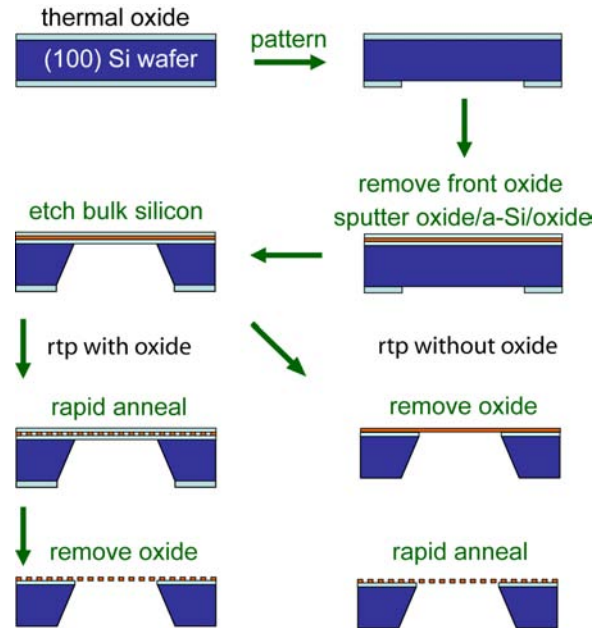


**Figure 3-11.** Process flow showing the rapid thermal anneal of two free-standing membrane structures: one with protective oxide and one without protective oxide.

By annealing a free-standing structure, the dominant source of strain in the thin film(s) is removed. Therefore, it is hypothesized that the resulting morphology will differ greatly from those presented in section 2.8.

### 3.7.1 Crystallization of a free-standing silicon thin film

15 nm and 30 nm films were deposited on a silicon substrate and then released from the bulk using an anisotropic etch process as described in section 2.7. The 20 nm of protective oxide was removed using a buffered oxide etchant. The free-standing amorphous silicon membrane was then placed inside a susceptor and subjected to a rapid thermal process at temperatures between 600°C and 1000°C at a ramp rate of 50°C/s with a 60 s steady-state soak time.

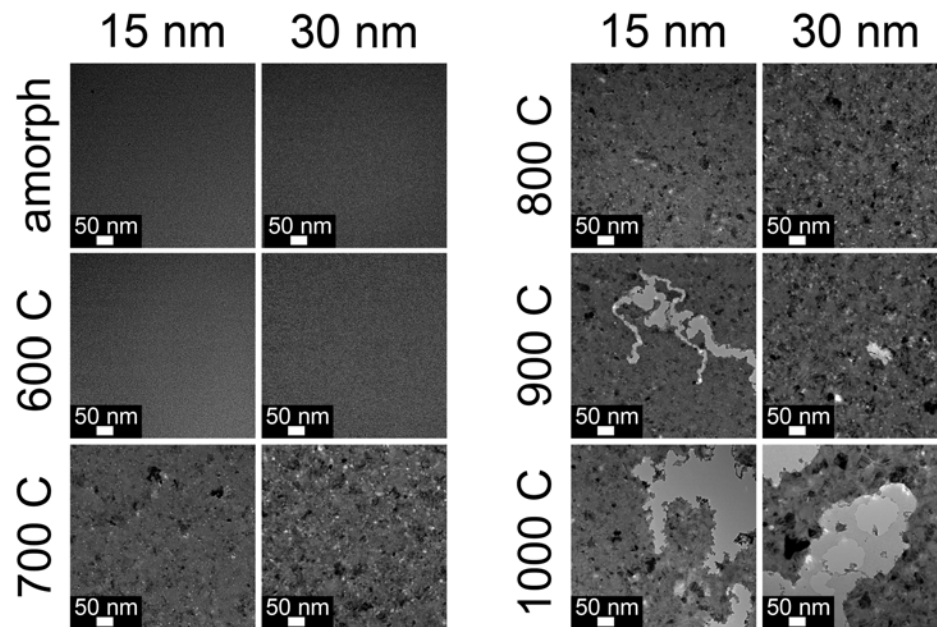


**Figure 3-12.** TEM micrographs of 15 nm and 30 nm thick silicon membranes annealed at various temperatures.

Figure 3-12 shows TEM micrographs of the resulting membrane morphologies. The 600°C sample is featureless and appears identical to the amorphous control sample.

Between 600°C and 700°C, the film crystallizes evidenced by the nanocrystalline grains and diffracting crystals. The small gray features are areas of lower material density. No through pores are discernable at this TEM magnification. Beyond 900°C, “tears” began to form in the film indicative of a violent kinetic process. From these results it would appear that the lack of a source of strain, i.e. a protective oxide and bulk substrate, during the crystallization process removes the driving force necessary for pore formation.

### **3.7.2 Crystallization of a SiO<sub>2</sub>/Si/SiO<sub>2</sub> free-standing membrane**

In the previous section, the removal of the bulk silicon support and protective oxide before crystallization eliminated the formation of pores. Here, the effect of annealing a free-standing silicon membrane surrounded by 20 nm of oxide will be examined. The difference in thermal expansion of silicon and silicon dioxide will induce a strain in the silicon thin film, although it is much less than that generated by a thick bulk substrate. The hypothesis was that by leaving the protective oxide on during the rapid thermal anneal there is a finite amount of strain to drive the pore formation process.



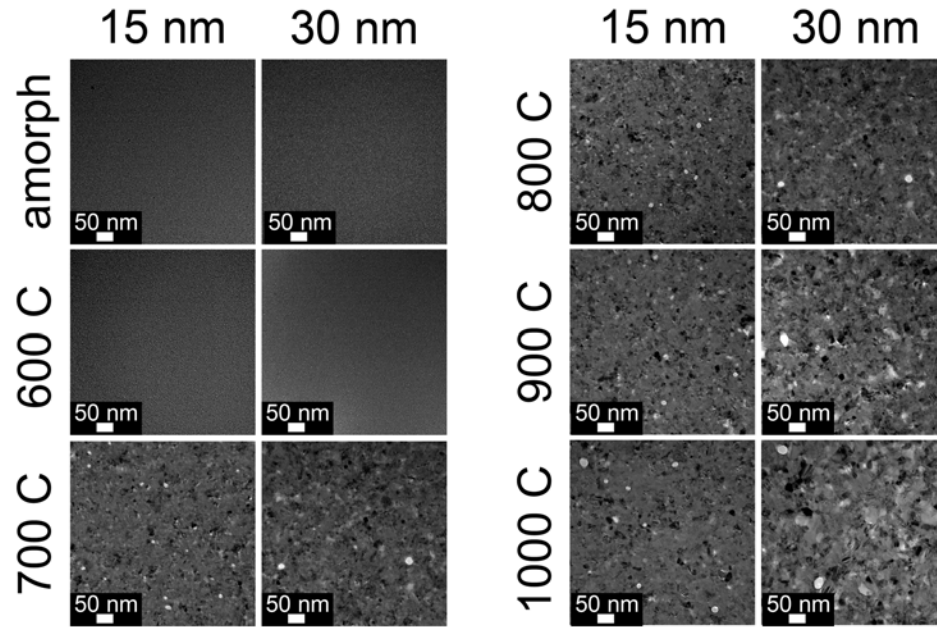


**Figure 3-13.** TEM micrographs of 15 nm and 30 nm thick silicon membranes annealed with 20 nm of surrounding protective oxide at various temperatures.

Figure 3-13 shows a series of TEM micrographs of 15 nm and 30 nm thick silicon membranes that were annealed with 20 nm of surrounding oxide. The oxide was removed before electron imaging. Between 600°C and 700°C, a low density of pores starts to form. Unlike the series presented in section 2.8.1, there is no trend of increasing pore size and density with increasing temperature. Although a small number of pores form, increasing the thermal energy budget during crystallization without an adequate strain driving force provided by a bulk layer prevents further pore growth. Hence, it has been demonstrated that strain induced by the bulk substrate is necessary during the crystallization process to facilitate high-density pore formation.

### 3.8 Conclusions

In this chapter, a phenomenological model for the formation of pores in pnc-Si has been presented. It is clear that pore formation occurs as a consequence of solid phase crystallization of very thin amorphous silicon confined by two silicon dioxide interfaces. Pores form as a result of nanocrystal growth and can be understood in the context of vacancy generation. The silicon atomic mobility is enhanced along nanocrystal microtwin features that in turn increases the vacancy generation rate and pore growth velocity. Finally, the quality of the silicon-silicon dioxide interface and defect density is shown to be pivotal in determining the ultimate pore density.

## **Chapter 4. Characterization of porous nanocrystalline silicon membranes**

### **4.1 Introduction**

A number of tools have been employed to study the properties of porous nanocrystalline silicon membranes. The most important characterization method used in the study of pnc-Si was transmission electron microscopy (TEM). Because pnc-Si membranes are transparent to an electron beam, pore properties such as pore size, porosity, and density can be calculated directly from the TEM micrographs. The fundamental optical properties of pnc-Si were investigated using spectroscopic ellipsometry (SE). SE was also routinely employed to confirm the quality and thickness of as-deposited thin films. Next, atomic force microscopy (AFM) of pnc-Si membranes was performed to extract information on surface topology and roughness. Finally, thin film bulge experiments were carried out in order to calculate the basic mechanical quantities of pnc-Si, such as the Young's modulus and intrinsic stress.

## 4.2 Transmission electron microscopy

Transmission electron microscopy (TEM) is a power tool for interrogating nanostructures. Due to its thinness, the morphology of pnc-Si can be investigated using TEM. In principle, a transmission electron microscope accelerates electrons emitted from a filament, typically made of lanthanum hexaboride ( $\text{LaB}_6$ ) or tungsten, through an electron column. The electrons are focused through several electron lenses, made of electromagnets that generate a magnetic field and manipulate the path of electrons. The electron beam may also be “shifted” by employing electrostatic fields. The beam passes through the specimen and an image is displayed on a phosphor screen or recorded using a charge-coupled device (CCD) camera.

The resolution limit of TEM is determined by the acceleration voltage used to generate the electron beam. In other words, the ability to discern two features is determined by the electron wavelength. More formally, Abbe’s equation can be used to calculate the spatial resolution of a system by:

$$d = \frac{0.612 * \lambda}{n \sin \alpha} ,$$

**Equation 4-1**

where  $d$  is the distance between two resolvable objects,  $\lambda$  is the wavelength of radiation,  $n$  is the index of refraction of the medium between the radiation source and lens, and  $a$  is the half angle of the cone of radiation accepted by the objective .

Using the de Broglie equation, which describes the wave-particle duality, the wavelength of an electron can be determined by:

$$\lambda = \frac{h}{mv},$$

**Equation 4-2**

where  $\lambda$  is the wavelength of electrons,  $h$  is Planck's constant,  $m$  is the mass of the electron, and  $v$  is the electron velocity. Solving Equation 4-1 and Equation 4-2 for an acceleration voltage of 100 kV, the limit of resolution is calculated to be 0.14 nm for a system free of aberrations and distortions, which is rarely the case. Also note that in the calculation of the mass of the electron, relativistic effects, where the effective mass of an electron increases as the velocity of a particle approaches the speed of light, have not been taken into account. Practical limits of resolution at acceleration voltages of 100 kV are closer to 2 nm. For voltages of 200 kV the resolution limit approaches 0.1 nm, providing the capability to image lattice planes and even individual atoms (Figure 4-1).

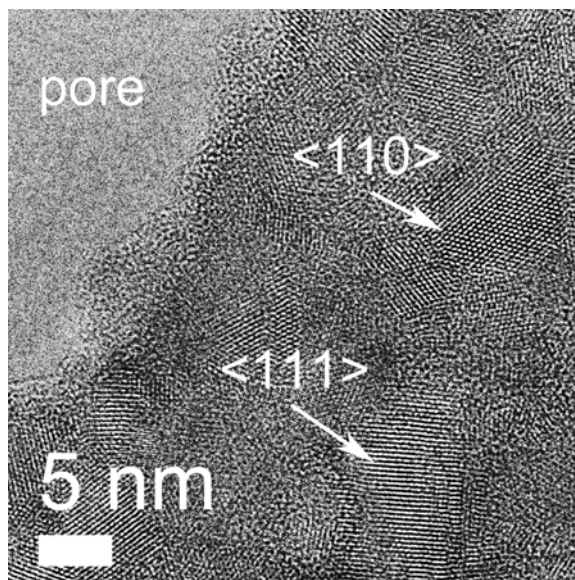


**Figure 4-1.** High-resolution TEM image showing a pore surrounded by nanocrystals of different orientation. The  $\langle 110 \rangle$  oriented Si nanocrystal has an atomic spacing of  $1.9 \text{ \AA}$ . The  $\langle 111 \rangle$  oriented nanocrystal has an atomic plane spacing of  $3.1 \text{ \AA}$ . The spacing was calculated from the TEM micrograph by averaging the distance between several atoms or planes.

The contrast in a TEM micrograph is determined by the interaction between incident electrons and variations in the atomic structure of the specimen. A heavy atom will scatter an electron more strongly than a light atom. Thus, in bright-field TEM a heavy atom will appear darker than a light atom. Similarly, electrons traveling through many atoms will have multiple scattering events and appear darker than thin areas where there are only a few scattering events. In addition to the mass-thickness contrast principle, crystalline specimens that have an atomic spacing that obeys the Bragg diffraction condition will scatter electrons and undergo destructive interference. These structures will appear black under bright-field imaging.

Two transmission electron microscopes were employed in studying pnc-Si. The first was a Hitachi 7650 (Schaumburg, IL) operated at 100 kV. The relatively low acceleration voltage allowed for high-throughput, lower resolution imaging of pnc-Si membranes to study pore morphology. The majority of TEM micrographs in this thesis were taken on this tool. Images were acquired digitally with an Olympus Cantega 11 megapixel CCD camera. An 11  $\mu\text{m}$  x 17  $\mu\text{m}$  micrograph was used to calculate the pore size distribution of pnc-Si membranes. The second TEM utilized in characterization was a FEI Technai F20 field emission microscope (Hillsboro, OR). This TEM was operated at 200 kV, which allowed for high-resolution imaging of individual pores and silicon nanocrystal lattices (Figure 4-1).

#### **4.2.1 Pore size distribution calculations**

Pnc-Si has the distinct advantage over other porous membranes of being amenable to characterization by transmission electron microscopy (TEM) due to its small thickness (15 – 30 nm). As such, pore distributions can be directly calculated from TEM micrographs using custom MATLAB scripts (Figure 4-2). Samples compatible with a TEM specimen holder were integrated on each wafer in several radial positions.

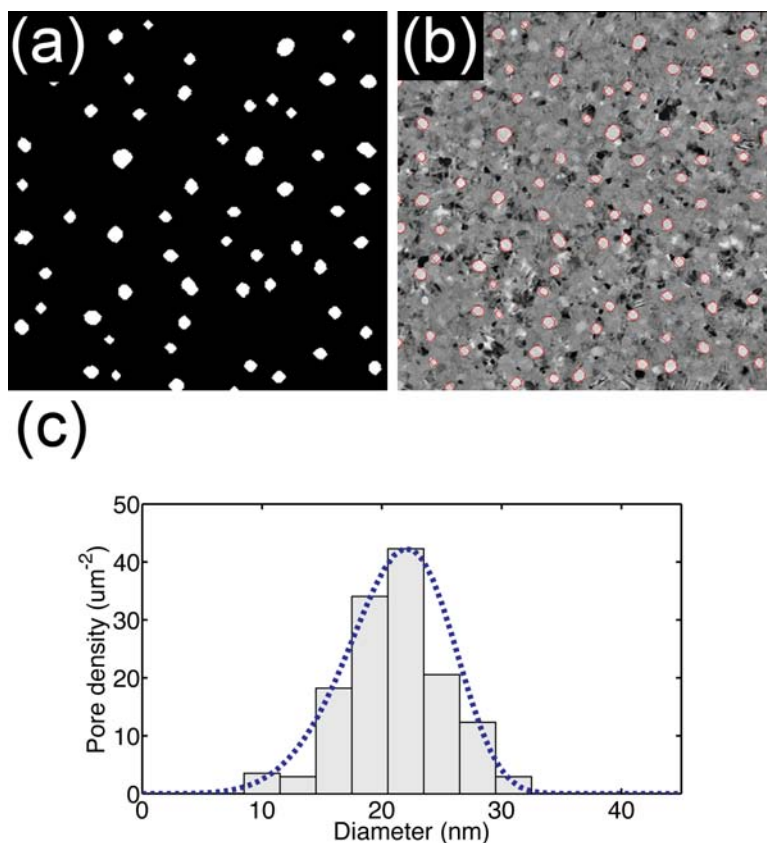


**Figure 4-2.** (a) A threshold algorithm is applied to the TEM image to create a binary image. (b) Pores are identified and (c) a size distribution calculated. A Weibull probability density fit is applied to the histogram (blue dashed line).

The MATLAB routine (available at [nanomembranes.org/resources/software](http://nanomembranes.org/resources/software)) inputs a digital TEM micrograph of pnc-Si. The first operations performed on the image involve removing “salt and pepper” or speckle noise using a median filter and a background correction algorithm, which uses a nearest-neighbor averaging algorithm to “smooth out” any variations in the lighting due to non-uniformity in the electron beam. Next, a threshold value is specified to separate the pores (high intensity pixels) from background features (low intensity pixels). The result is a binary image where pores are



highlighted in white ('1') and the solid film is black ('0') (Figure 4-2a). Frequently, the threshold procedure will yield false positives; that is, areas of solid film that are highlighted white. To remove these areas, an iterative process of pixel dilation, erosion, opening, and closing is performed [91]. Any remaining false positives are identified manually by comparing the binary image with the original micrograph and removed. Finally, pore statistic calculations are performed and pore sizes are binned into a histogram.

After acquiring a pore size distribution, the histogram was fit using a scaled Weibull probability density function [92] in the form of:

$$y = c * \left(\frac{x}{a}\right)^b * \exp\left(-\left(\frac{x}{a}\right)^b\right),$$

**Equation 4-3**

where  $a$  and  $c$  scale the horizontal and vertical dimensions and  $b$  determines the shape of the curve (Figure 4-2c). Estimating the pore density as a continuous curve allows us to graphically compare sets of distributions on the same plot. It should be noted that due to the nature of pore formation in pnc-Si a sharp pore size cut-off can be defined. Thus, an exponential fit like the Weibull function may be used to characterize the pore size distribution. In contrast, conventional ultrafiltration membranes have a much wider pore size distribution described by log-normal fits [93]. And while polymeric track-etched membranes have the potential for a narrow range of pore sizes, they are plagued by the

presence of multiple pore structures due to limits in manufacturing, which manifest in multi-peak size distributions [39].

#### **4.2.2 Pore size distribution error analysis**

Typically, a single TEM micrograph is used to characterize the pore size distribution across an entire wafer. However, there are inevitably errors associated with analysis using a low sample size. Pore statistics are generated from an  $11\text{ }\mu\text{m} \times 17\text{ }\mu\text{m}$  micrograph. One natural question that should be raised is whether this area is representative of the entire membrane area, which spans tens of thousands  $\mu\text{m}^2$ . Table 4-1 shows the average pore diameter and membrane porosity calculated at 10 different points on a  $200\text{ }\mu\text{m} \times 200\text{ }\mu\text{m}$  pnc-Si membrane.

**Table 4-1.** Table showing average pore diameter and membrane porosity over 10 TEM fields

Avg. diameter (nm)	Porosity (%)
19.6	6.7
19.4	6.6
19.6	7
19.4	6.6
19.6	7
19.7	7.1
19.4	7
19.6	7
19.5	6.8
19.7	6.8

The standard deviation in average pore diameter and membrane porosity is 0.1 nm and 0.2%, respectively. From these results, it is concluded that there is very little variation in morphology within a single membrane window. Thus, statistical analysis of one region of interest will be sufficiently representative of the entire membrane area.

## 4.3 Optical properties

Studies were performed to determine the index of refraction ( $n$ ) and extinction coefficient ( $k$ ) of amorphous and porous nanocrystalline membranes.

### 4.3.1 Spectroscopic ellipsometry

Ellipsometry is a highly sensitive measurement technique that uses polarized light to characterize a thin film (10 nm – 1  $\mu$ m). When an incident beam with a known polarization state (linear in this case) reflects off a thin film, it will interact with the thin film and its polarization state will change (Figure 4-3).

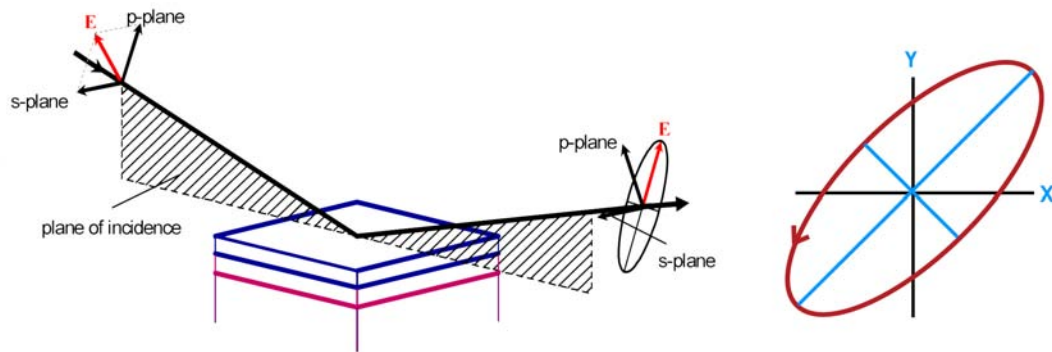


**Figure 4-3.** A light wave will change its polarization state after it reflects off the surface of a thin film. An ellipsometer measures this change and extracts thickness and optical constant information from it. [94]

Elliptically polarized light may be described as a complex ratio of the electric field components [95],

$$\frac{\tilde{E}_x}{\tilde{E}_y} = \frac{E_{x0}}{E_{y0}} e^{i(\delta_x - \delta_y)} = \tan(\Psi) e^{i\Delta}$$

**Equation 4-4**

$$\text{where } \tan(\Psi) = \frac{E_{x0}}{E_{y0}} \text{ and } \Delta = \delta_x - \delta_y.$$

Equation 4-4 can be re-written as the ratio of the complex Fresnel reflection coefficients in the  $s$  and  $p$  planes:

$$\rho = \tan(\Psi) e^{i\Delta} = \frac{\tilde{R}_p}{\tilde{R}_s} = \frac{E_p^{out} / E_p^{in}}{E_s^{out} / E_s^{in}} = \frac{|r_p|}{|r_s|} e^{i\Delta}.$$

**Equation 4-5**

The ellipsometer measures the angles  $\psi$ , a ratio of the magnitudes of the complex reflection coefficients, and  $\Delta$ , the phase change between the reflection coefficient components, directly. The film thickness and its optical constants ( $n, k$ ) can be extracted from these measurements.

Ellipsometric measurements were performed on a variable angle spectroscopic ellipsometer (VASE) manufactured by J. A. Woollam Co., Inc. Measurements were taken in the spectral range of 240 nm to 1700 nm at three different angles. A 75 W Xenon lamp was put through a monochromator for use as the incident beam. A beam

chopper was placed at the monochromator output and ambient light was rejected with synchronous detection techniques. The light was polarized with a calcite Glan-Taylor polarizer. An auto-retarder (compensator) was used to ensure maximum sensitivity in the measurement. Light reflected from the sample is passed through a rotating analyzer and collected by a Si / InGaAs stacked photodiode assembly.

### 4.3.2 Optical constants

The ellipsometer does not measure the optical constants of a thin film directly. Instead, a parametric model from the  $\psi$  and  $\Delta$  measurements is developed and fit thus yielding the film thickness, index of refraction,  $n$ , and extinction coefficient,  $k$ . The refractive index of a material describes how the light changes propagation speed and direction as it enters the material. The extinction coefficient describes how much energy the light loses (i.e. energy absorbed) when it enters the material. Together, these two terms are written as the complex refractive index as a function of wavelength (or energy):

$$\tilde{n}(\lambda) = n(\lambda) + i \cdot k(\lambda).$$

**Equation 4-6**

Analogous to the complex refractive index, the change induced by the incident light wave is described by a material's complex dielectric function:

$$\tilde{\varepsilon}(\lambda) = \varepsilon_1(\lambda) + i \cdot \varepsilon_2(\lambda),$$

**Equation 4-7**

where  $\varepsilon_1$  is the volume polarization term for induced dipoles and  $\varepsilon_2$  is the volume absorption related to carrier generation. These two quantities are analogous via the following equations:

$$n = \sqrt{\frac{\left[ \varepsilon_1 + \sqrt{\varepsilon_1^2 + \varepsilon_2^2} \right]}{2}},$$

**Equation 4-8**

$$k = \sqrt{\frac{\left[ -\varepsilon_1 + \sqrt{\varepsilon_1^2 + \varepsilon_2^2} \right]}{2}}.$$

**Equation 4-9**

### 4.3.3 Silicon dioxide

Ellipsometry was performed on a 20 nm silicon dioxide film sputtered on a bare silicon wafer (Figure 4-4). The index of refraction was measured to be 1.464 at 1.38 eV (900 nm), which is very close to the optical density of a high density thermally grown oxide – 1.462. As expected from a transparent film, the extinction coefficient is zero and there is no absorption in the film.

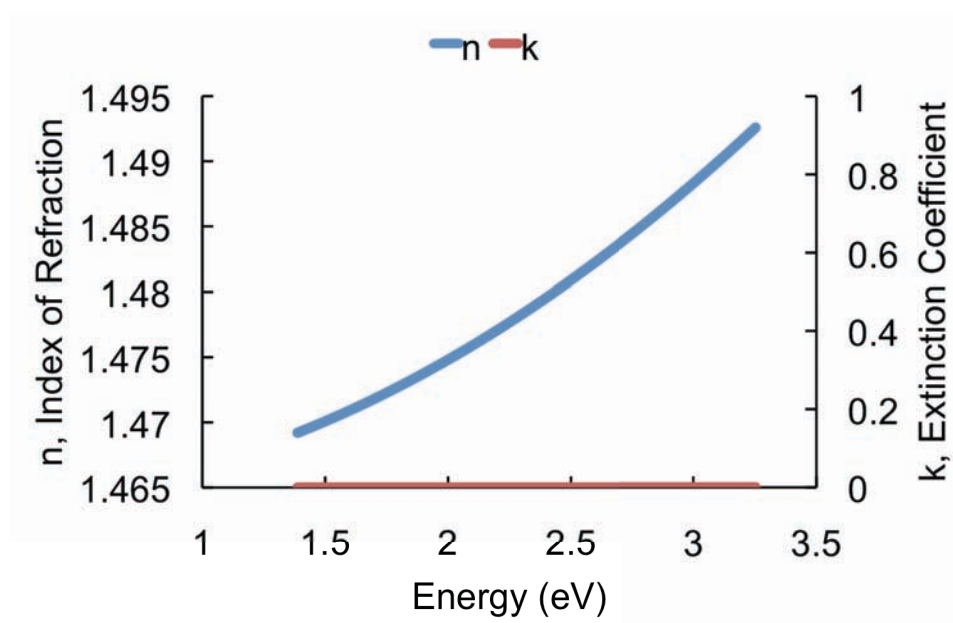


**Figure 4-4.** Index of refraction and extinction coefficient of a sputtered silicon dioxide film.

#### 4.3.4 Nanocrystalline silicon

Ellipsometric measurements were performed on both amorphous and nanocrystalline silicon (nc-Si) films deposited by rf magnetron sputtering. A 20 nm/15 nm/20 nm oxide/a-Si/oxide film stack was deposited on a bare 4-inch silicon substrate. The nanocrystalline film was annealed at 1000 °C at 100 °C/s for 60 seconds. As expected, the index of refraction of the amorphous silicon film is broad and featureless over all measured energies (Figure 4-5, Figure 4-6). In contrast, the index of refraction of the nanocrystalline film shows a slight “bump” at 3.5 eV indicating the film is more absorbing than its amorphous counterpart. This result is supported by the extinction



coefficient measurement, which shows that the nc-Si film has a defined absorption edge at 2.2 eV indicative of a crystallized film [67].

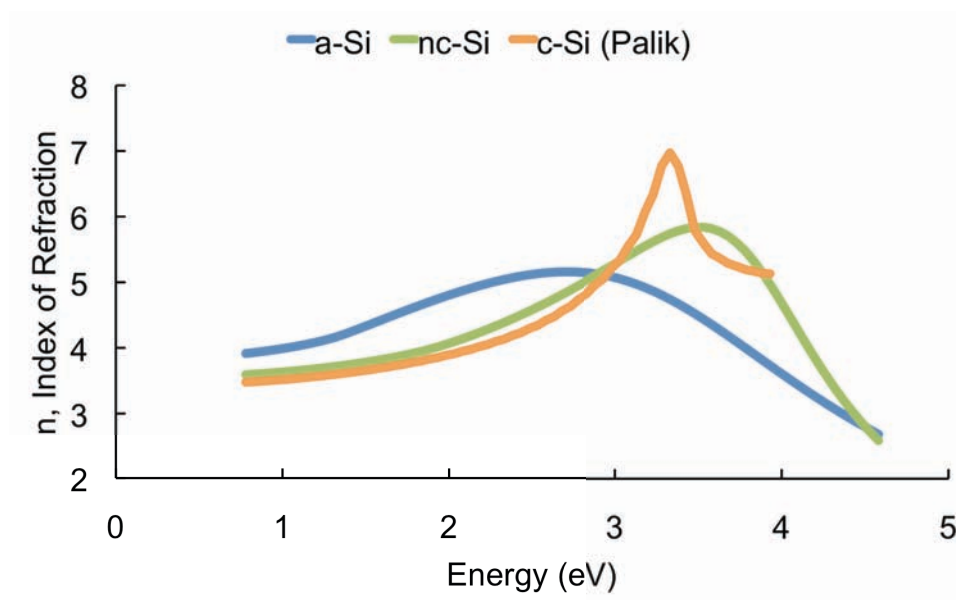


**Figure 4-5.** Comparison of the index of refraction for amorphous silicon, nanocrystalline silicon, and a reference single crystal silicon [96].

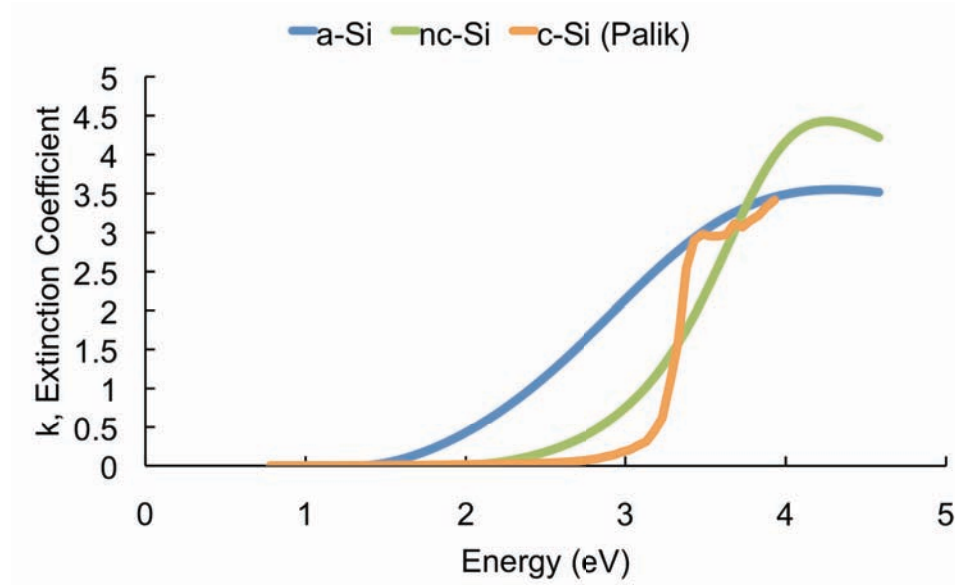


**Figure 4-6.** Comparison of the extinction coefficient for amorphous silicon, nanocrystalline silicon, and a reference single crystal silicon [96].

## 4.4 Surface morphology

Atomic force microscopy (AFM) is a non-destructive method for mapping the topography of a sample with high spatial resolution in the vertical  $z$ -direction. A sharp tip on a cantilever is brought close to the sample and scanned across its surface. The atomic force microscope (MFP-3D-SA, Asylum Research, Santa Barbara, CA) can be operated in three modes: contact, non-contact and tapping mode. The measurements on pnc-Si membranes were carried out in the non-contact mode. In this mode, the tip never touches the sample and it can be imaged without exerting shear forces. The cantilever is oscillated at a particular frequency (near the resonance frequency so that the sensitivity is maximized) and the change in its amplitude measured as it oscillates close to the

sample. Although the cantilever never touches the sample, its oscillation amplitude changes due to attractive van der Waal forces. This change in amplitude is used as a feedback parameter to vertically move the tip as it is laterally scanned across the sample.

An AFM scan of a pnc-Si membrane shows that the silicon film on top of the underlying oxide and bulk silicon support shows a low surface roughness of 2.9 Å (Figure 4-7). The pores in the film were excluded from the RMS roughness value calculation by applying an exclusion mask created using a routine similar to that in the transmission electron microscopy micrograph pore processing. Comparing the crystallized porous film to an as-deposited amorphous silicon film, the RMS roughness increases by three-fold (from 1.0 Å to 2.9 Å). This increase in roughness is due to the volume contraction and conservation of mass of the silicon associated with pore formation.

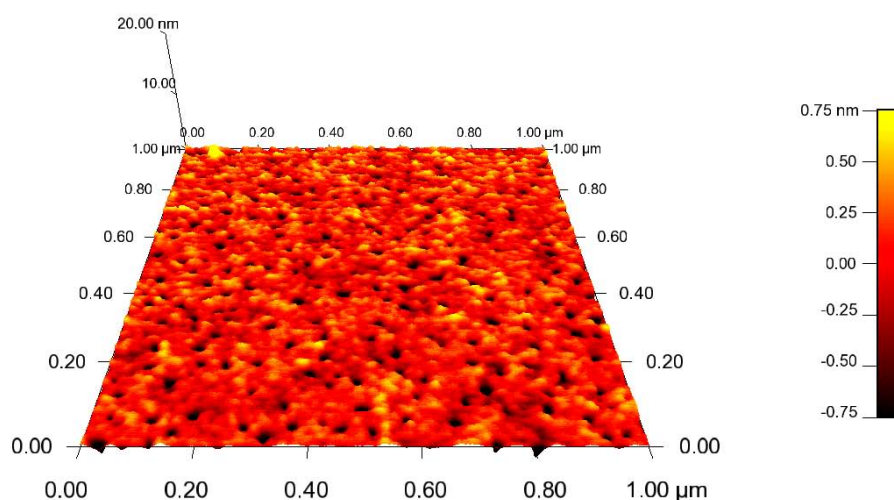


**Figure 4-7.** AFM scan of a pnc-Si film supported by the Si scaffold. Dark spots

indicate the porous regions. RMS roughness of the non-porous background is 2.9 Å.

## 4.5 Mechanical properties

### 4.5.1 Mechanical properties of thin films

The mechanical properties of a material describe the manner in which a material responds to an applied stress. A material, such as pnc-Si, that recovers immediately after an applied force is removed is said to be elastic. Elastic deformation of a material can be characterized by the Young's modulus,  $E$ , and Poisson's ratio,  $\nu$ . These two quantities are related to one another by writing a general form of Hooke's law in three dimensions, assuming the material is isotropic i.e.  $E$  and  $\nu$  are constant in all directions:

$$\varepsilon_x = \frac{1}{E} \left[ \sigma_x - \nu(\sigma_y + \sigma_z) \right],$$

**Equation 4-10**

$$\varepsilon_y = \frac{1}{E} \left[ \sigma_y - \nu(\sigma_x + \sigma_z) \right],$$

**Equation 4-11**

$$\varepsilon_z = \frac{1}{E} \left[ \sigma_z - \nu(\sigma_x + \sigma_y) \right],$$

**Equation 4-12**

where  $\varepsilon_i$  denotes the strain and  $\sigma_i$  the stress in each of the three directions. For thin films i.e. the thickness of the film is  $\ll$  deflection height, it is assumed that the material is under biaxial stress, in which case  $\sigma_x = \sigma_y$  and  $\sigma_z = 0$ . Thus, Equation 4-10 through Equation 4-12 can be simplified to:

$$\sigma_x = \frac{E}{1 - \nu} \varepsilon_x,$$

**Equation 4-13**

where  $M = E/(1 - \nu)$  as the biaxial modulus.

The biaxial modulus is an important factor in determining the induced stress in a thin film anchored to a thick substrate during thermal treatment, such as the rapid thermal process carried out to induce pore formation in pnc-Si. The differential stress can be written as

$$\sigma_x = M_f \Delta T (\alpha_s - \alpha_f),$$

**Equation 4-14**

where  $\alpha_f$  and  $\alpha_s$  are the thermal expansion coefficients of the film and substrate, respectively,  $M_f$  is the film biaxial modulus, and  $\Delta T$  is the induced temperature change [97]. For films that have been thermally treated, the differential stress constitutes the majority of the films residual stress,  $\sigma_0$ , and thus it can be assumed that  $\sigma_0 \approx \sigma_x$ .

### 4.5.2 Pressure-displacement measurements

Porous nanocrystalline silicon membranes have been established as a surprisingly strong ultra-thin material, able to withstand elastic deformation to at least 15 PSI (1 atm) [53]. The fundamental mechanical properties, however, have not yet been investigated. Initial studies into these properties of pnc-Si were carried out using the “bulge test” [98]. This technique has been used previously to investigate thin film membranes suspended over windows of different geometries. In this work, the deflection of a pressurized membrane is recorded by a white-light interferometer (Wyko NT1100, Veeco, Plainview, NY) and the data is fit with the generalized bulge equation using a least-squares algorithm with the Young’s modulus and residual stress as its parameters:

$$p = c_1 \sigma_0 t \frac{h}{a^4} + c_2 M t \frac{h^3}{a^4}.$$

**Equation 4-15**

The  $c_1$  and  $c_2$  coefficients are dependent on the membrane geometry and the film’s Poisson ratio,  $\nu$ ,  $p$  is the pressure applied to the membrane,  $\sigma_0$  is the film’s residual stress,  $t$  is the thickness of the film,  $h$  is the vertical displacement at the center of the membrane,  $2a$  is the length of the square window, and  $M$  is the biaxial modulus,  $E/(1-\nu)$ , for an isotropic film. For a square membrane, Vlassak calculated  $c_1 = 3.393$  and  $c_2 = (0.792 + 0.085 \nu)^{-3}$  using energy minimization techniques to match the free energy of the membrane with the membrane displacement field [98].

A Veeco Wyko NT1100 (Santa Clara, CA) white light interferometer was used to interrogate the change in membrane height under an applied pressure. Generally, an interferometer measures the height of a sample by extracting the phase data from interference fringes caused by the recombination of a sample and reference beam and using the equation:

$$h(x,y) = \frac{\lambda}{4\pi} \phi(x,y),$$

**Equation 4-16**

where  $\lambda$  is the wavelength of the source beam and  $\phi(x,y)$  is the phase data. This is called phase-shifting interferometry (PSI). However, due to limitations in this technique, height differences greater than  $\lambda/4$  can result in measurement errors.

Thus, a technique developed at Veeco called vertical-scanning interferometry (VSI) is employed to overcome these limitations. Instead of measuring the changes of intensity of the interference fringes, VSI looks at the modulation of interference fringes as the interferometric objective translates. Demodulation of the envelope function of the fringe contrast signal at different foci yields the height data. Using the VSI technique, a dynamic range of 2 mm and resolution of 3 nm is achieved.

Figure 4-10 shows a schematic of the experimental setup. A membrane chip is sealed inside a custom made enclosure, which is pressurized with compressed air from one side. A 0-10 PSI gas regulator and manometer is used to control the pressure. A solid silicon chip was sealed inside the enclosure and pressurized in order to confirm there were no gross leaks in the system. The pressure decreased less than 0.5 PSI over

five minutes. Therefore, it can be assumed that there is sufficient accuracy in the pressure measurement over the duration of data acquisition (less than one minute). The interferometric objective is placed directly above the membrane window. Pressure is increased in 0.1 PSI increments as the height data is recorded with sufficient time in between measurements to let transient flow settle into a steady state.

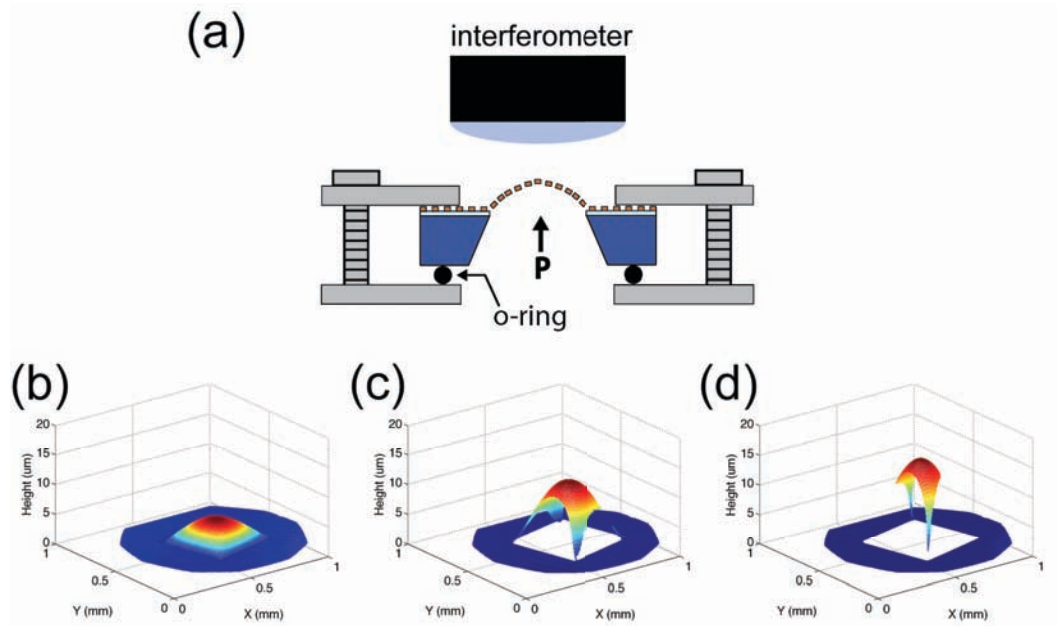


**Figure 4-8.** (a) Membrane deflection experimental setup. A white light interferometer is used to measure the height of a membrane under pressure. (b) – (d) Deflection behavior of a 15 nm thick pnc-Si membrane  $400\ \mu\text{m} \times 400\ \mu\text{m}$  under 0.1, 0.3, and 0.5 PSI of pressure.

Because *porous* films are being studied, the effect of porosity on the Young's modulus and residual stress must be considered. Harrop [99] and Kovács [100] have shown that the Young's modulus of a solid film may be calculated from the perforated



form by multiplying by a correction factor of  $1/(1-P)$ , where  $P$  is the membrane porosity.

That is,

$$E_{solid} = \frac{E_{porous}}{(1 - P)},$$

**Equation 4-17**

where  $E_{solid}$  and  $E_{porous}$  is the Young's modulus of the non-perforated and perforated films, respectively, and  $P$  is the porosity of the perforated film. Similarly, the corrected residual stress of a solid film may be calculated by:

$$\sigma_{0,solid} = \frac{\sigma_{0,porous}}{(1 - P)}$$

**Equation 4-18**

where  $\sigma_{0,solid}$  and  $\sigma_{0,porous}$  is the residual stress of the non-perforated and perforated films, respectively, and  $P$  is the porosity of the perforated film. In order to compare the quantities measured in this work with historical data, only the  $E_{solid}$  and  $\sigma_{0,solid}$  values will be presented.

#### 4.5.2.1 Deflection of porous silicon nitride membranes

In order to verify the accuracy of our experimental setup a series of measurements were performed on porous silicon nitride membranes, which are well characterized in literature [101]. 50 nm thick porous silicon nitride membranes with an active area of 1 mm x 1 mm (SiMPore, West Henrietta, NY) with evenly spaced 2  $\mu\text{m}$  holes and a pitch of 4  $\mu\text{m}$  (20% porosity) were measured in the pressure-displacement setup described in section 4.5.2.

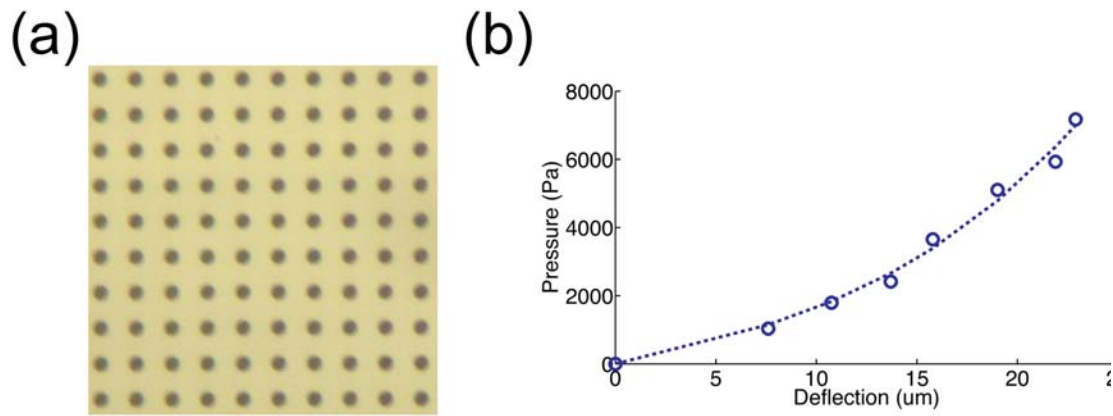


**Figure 4-9.** (a) Bright-field optical image of a 50 nm thick porous silicon nitride membrane. The holes are 3  $\mu\text{m}$  in diameter with a pore pitch of 6  $\mu\text{m}$ . (b) Pressure-displacement behavior of the silicon nitride membrane. The Young's modulus and residual stress was extracted from a least-squares curve fit using Equation 4-15.

Consistent with values reported in literature, a Young's modulus of 208 GPa and residual stress of 200 MPa was calculated using the technique described in the previous section [101].

#### 4.5.2.2 Deflection of pnc-Si membranes

In order to determine the Young's modulus of pnc-Si, a value for Poisson's ratio,  $\nu = 0.22$ , was assumed based on previous studies with polysilicon [102]. Equation 4-15 was fit to an experimental pressure-displacement curve using a least-squares method (Equation 4-11). Three different square membrane geometries were investigated. Figure 4-10 shows the pressure-displacement behavior for the different pnc-Si membranes investigated using the bulge-test. Table 4-2 summarizes the Young's modulus,  $E$ , and residual stress,  $\sigma_0$ , of pnc-Si and other silicon structures.

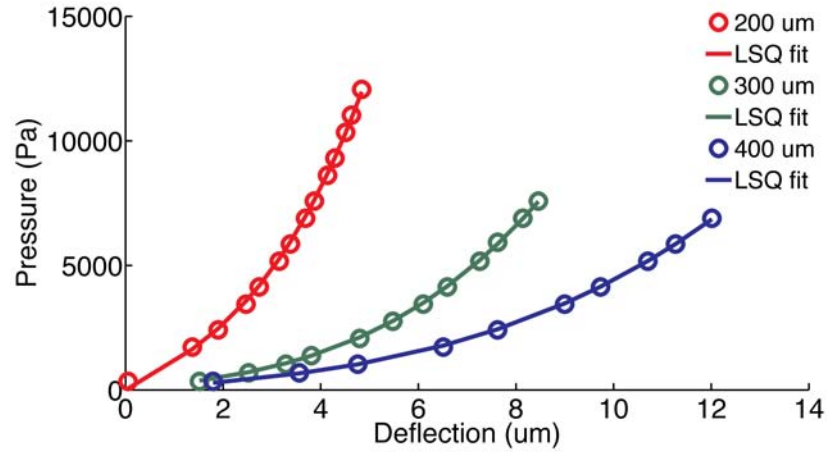


**Figure 4-10.** Pressure-displacement curve for three different pnc-Si membrane geometries. The solid line represents the least-squares fit to the generalized bulge equation. The inset shows a three-dimensional rendering of the membrane under pressure as measured by the white light interferometer.

**Table 4-2.** Table of Young's Modulus and Residual Stress

Material	Young's Modulus ( $E$ )	Residual Stress ( $\sigma_0$ )
Pnc-Si (200 $\mu\text{m}$ )	116 GPa	180 MPa
Pnc-Si (300 $\mu\text{m}$ )	106 GPa	90 MPa
Pnc-Si (400 $\mu\text{m}$ )	110 GPa	110 MPa
LPCVD Polysilicon [102]	$151 \pm 6$ GPa	$-350 \pm 12$ MPa
Porous Silicon (36%) [103]	50 GPa	-
Single Crystal Silicon [104]	$169 \pm 2.5$ GPa	-

From these results, it is determined that pnc-Si has a much lower residual stress than its polysilicon counterpart. This is due to the thermal annealing process, which converts the nanocrystalline film from a compressive to slightly tensile state. The Young's modulus of pnc-Si is also significantly lower than the poly- and mono-crystalline states, implying that this ultra-thin membrane material is extremely flexible.

## **4.6 Conclusions**

In this chapter, basic physical properties of porous nanocrystalline silicon membranes have been presented. By taking advantage of the small thickness, pore morphology can be directly investigated using transmission electron microscopy. It has been shown that the pore properties can be calculated directly from TEM micrographs. The optical properties of pnc-Si have been calculated by spectroscopic ellipsometry and are shown to have absorption features characteristic of a pseudo-crystalline material. Next, AFM was employed to determine that pnc-Si has low surface roughness on the order of a polished silicon wafer. Finally, the fundamental material quantities of Young's modulus and intrinsic stress have been presented. It is shown that pnc-Si is an extremely flexible material with low residual stress values.

## **Chapter 5. Functionalization of porous nanocrystalline silicon membranes**

### **5.1 Rapid thermal carbonization**

#### **5.1.1 Introduction**

In this section, a technique to precisely tune the pore size of pnc-Si membranes using rapid thermal carbonization in a dilute acetylene ( $C_2H_2$ ) atmosphere will be presented [55]. The magnitude of size reduction is controlled by varying the process temperature and time of carbonization. Under certain conditions, the carbon coating displayed atomic ordering indicative of graphene layer formation conformal to the pore walls. It will be shown that carbonized membranes follow theoretical predictions for hydraulic permeability and retain the precise separation capabilities of untreated membranes [54].

Using standard microfabrication techniques, pnc-Si pore sizes can be tuned from being nonporous to having pores greater than 80 nm, however the resolution of control over pore size during manufacturing is limited to  $\pm 5$  nm. In order to optimize the quality of a separation procedure, finer control over pore sizes is desirable. In this study, it is shown that carbonization can be used as a post-production means to tune pore sizes with sub-nanometer precision thus allowing for further optimization of the sieving properties

of the membrane. Under certain conditions, atomic ordering is observed along the pore walls suggesting graphene formation during carbonization. Given the high fluxes of water and gas through carbon nanotube (CNT) membranes, carbonization on pnc-Si may lead to novel silicon-carbon hybrid devices with enhanced transport properties over traditional technologies [27, 28]. Consistent with the prior work involving untreated pnc-Si membranes [54], the hydraulic permeability of a carbonized membrane is shown to follow theoretical predictions. Additionally, the separation of gold nanoparticles before and after carbonization is demonstrated, thus indicating carbonized membranes retain the precise separation characteristics of untreated membranes [54]. Furthermore, carbonized pnc-Si membranes can be used to effectively filter proteins of different sizes. Thus, carbonization of pnc-Si provides an additional path for pore size control without negative impact on the performance of pnc-Si as a size-selective filter. Finally, carbonization will be shown to significantly improve chemical stability in highly alkaline solutions that rapidly etch silicon.

Previous techniques to control the size of nanoporous membranes involve coating pores with polymers [105] or metal [106]. While polymer coatings are relatively easy to deposit, they are unable to withstand high temperatures and harsh chemical environments. Metal coatings are more resilient, but processing can be complicated and the compatibility of these materials with biological applications is limited. Pore modification via rapid thermal carbonization suffers from neither of these drawbacks. Carbonization of PSi has been reported to improve chemical stability [107] in extremely basic environments by displacing Si-H bonds with Si-C. Furthermore, a recent study has shown that thermally carbonized PSi is bio-compatible and non-toxic [108].

Functionalization of the PSi surface has been verified by various methods such as differential scanning calorimetry (DSC) and Fourier transform infrared spectrometry (FTIR) [109] or photoluminescence measurements [110]. Although PSi and pnc-Si are different materials structurally, they both have Si-H terminations that can be replaced by Si-C during carbonization. Thus, it is reasonable to believe that pnc-Si would behave similarly during carbonization and inherit the improvements in stability observed with PSi. In this study, high-resolution transmission electron microscopy (HRTEM) and energy dispersive x-ray spectroscopy (EDX) were used to investigate how carbonization affects these ultrathin porous structures. Pore size distributions were obtained directly from the TEM micrographs using a custom pore recognition script written in MATLAB as previously described in section 4.2 [54].

### 5.1.2 Carbonization in a rapid thermal processor

Carbonization of porous nanocrystalline silicon membranes was carried out in a Surface Science Integration Solaris 150 rapid thermal processor (El Mirage, AZ) inside a silicon carbide-coated graphite susceptor. The rapid thermal processor is capable of reaching temperatures of 1200°C in less than 10 seconds and allows for the introduction of process gases via two mass flow controllers (Figure 5-1). In this study, acetylene ( $C_2H_2$ ) was chosen as the reactive hydrocarbon. This carbonization process was completed in less than 20 minutes as compared to the hours-long procedures using chemical vapor deposition reported in previous studies [107, 110]. A five-minute argon flush was performed before and after every thermal cycle to ensure the quartz chamber remained free of contaminant gases such as oxygen. After treatment, the contact angle of



a carbonized membrane was measured (Figure 5-1(b)). Consistent with prior work, carbonization decreased the contact angle slightly, from  $76^\circ$  to  $60^\circ$ , after treatment [107].

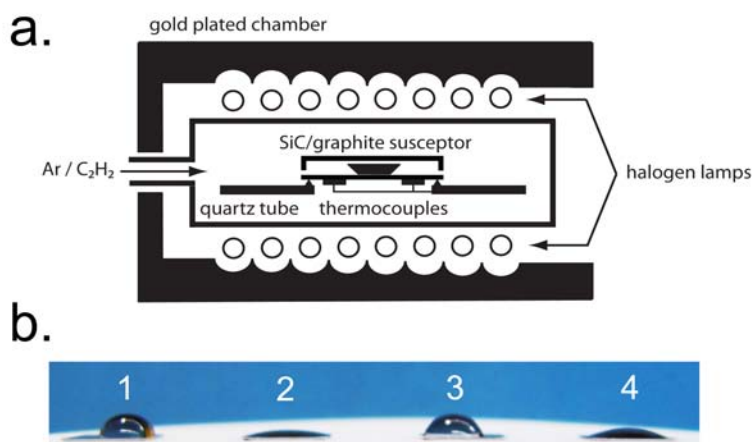


**Figure 5-1.** (a) Schematic of the rapid thermal processing unit used for carbonization. Membrane chips are placed inside a SiC coated graphite susceptor. A mixture of argon and acetylene is introduced into the chamber and heated to high temperatures. Two thermocouples monitor the temperature uniformity of the process. (b) (1) Contact angles of an untreated ( $76^\circ$ ), (2) ozone treated ( $16^\circ$ ), (3) carbonized ( $60^\circ$ ), and (4) carbonized and ozone treated ( $22^\circ$ ) membrane.

Several groups have studied acetylene absorption onto silicon substrates through modeling [111, 112] as well as experimentally [113, 114]. In these studies, it was determined that below  $600^\circ\text{C}$ , acetylene is chemisorbed at the surface. At  $660^\circ\text{C}$ , hydrogen disassociates and leaves the surface in the form of  $\text{H}_2$ . At these elevated temperatures, carbon is free to diffuse into the subsurface and bond with silicon forming a  $\text{Si}_{1-x}\text{C}_x$  compound. At temperatures beyond  $750^\circ\text{C}$  graphitization occurs. Salonen *et al.*

showed experimentally that carbonization was highly temperature dependent [109]. Below 600°C, FTIR measurements showed traces of C-H<sub>x</sub> bonding in porous silicon. Above 600°C, the spectra indicated a transition to a SiC bonding configuration.

### 5.1.3 Temperature dependence

The degree of pore closure from carbonization in pnc-Si is highly temperature dependent (Figure 5-2). Membranes were fabricated identically, as described in Striemer *et al.* [53], and each treated with acetylene at four different temperatures in the rapid thermal processor. To verify that the pore structure is only affected when acetylene is present, a control sample was annealed at 800°C for five minutes in argon only [56]. Electron microscopy and pore histogram analysis was performed on this membrane and the mean diameter did not change by a thermal treatment in argon alone (Figure 5-3). The soak time for all carbonization trials was five minutes and the argon and acetylene flow was fixed at 9 slm and 1 slm, respectively. Below 600°C, no significant deposition of carbon was found along the pore walls. However, between 600°C and 700°C a noticeable carbon coating formed. At 750°C the rate of carbon growth increase nearly seven-fold and the average pore size and porosity of the membrane decreased considerably. At 800°C, the majority of the pores were occluded.

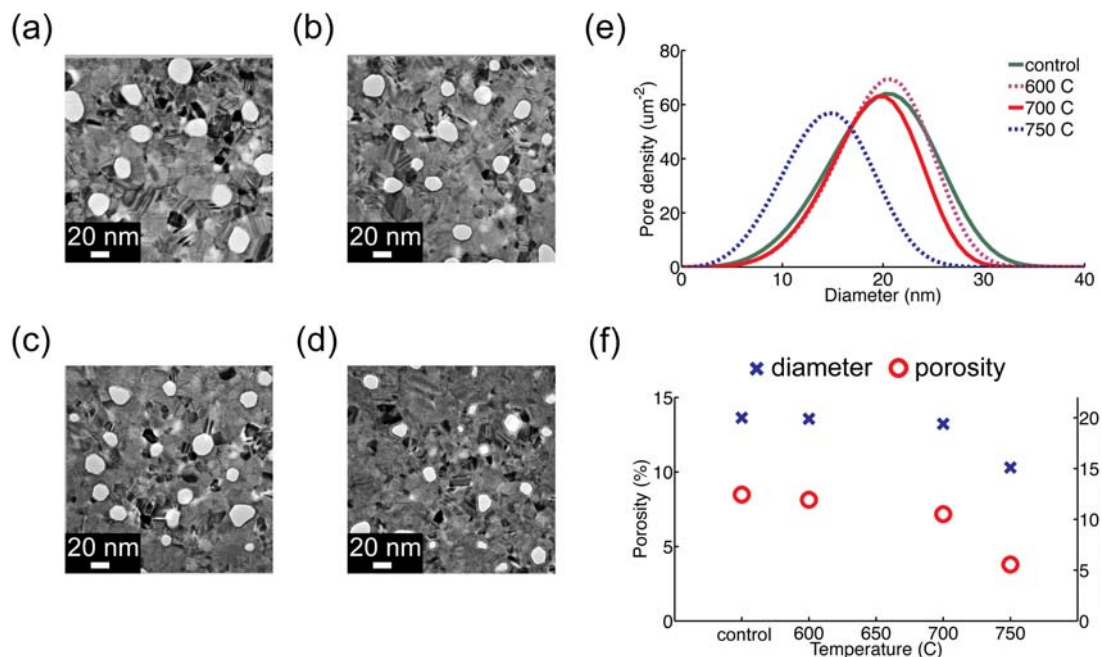


**Figure 5-2.** TEM images of carbonized membranes at different temperatures: (a) untreated, (b) 600°C, (c) 700°C, (d) 750°C. Scale bar is 20 nm. A 10% acetylene in argon mixture was used with a five minute soak time. (e) Pore size distribution as calculated from TEM images (f) Graph showing size (blue 'X') and porosity dependence (red 'O') with soak temperature. The standard deviation of porosity and diameter is 0.25% and 0.5 nm, respectively.

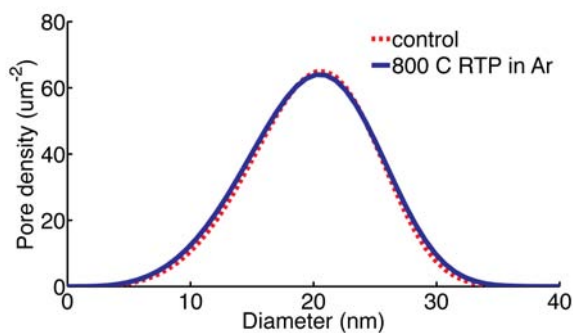


**Figure 5-3.** Pore distribution of a membrane annealed for five minutes at 800°C in 10 slm of Ar. There is no change in pore structure before and after annealing.

### 5.1.4 Time dependence

To investigate the effect of soak time on carbonization of pnc-Si membranes, three identically fabricated membranes were exposed to acetylene for 5, 10, and 15 minutes. The process temperature was fixed at 750°C with an argon to acetylene flow of 9 slm to 1 slm. This temperature was chosen because it guaranteed the decomposition carbon and hydrogen from acetylene. By varying the soak time, pore diameters can be reduced by 5 nm after 5 minutes, 10 nm after 10 minutes, and greater than 15 nm after 15 minutes (Figure 5-4). The growth rate appears to be constant through 10 minutes except at the 15 minute time point where it increases slightly (Figure 5-4(f)). The approximate growth rate was calculated to be 3.1 Å/min by measuring the amount of carbon growth after 10 minutes. These results indicate that after an initial seeding layer, carbon growth is eventually restricted by the mismatch strain due to the silicon and is governed by a new kinetic rate constant [115]. Carbon growth on silicon nanopores also appears to be independent of pore size (Figure 5-5), suggesting that the process is not self-limiting.

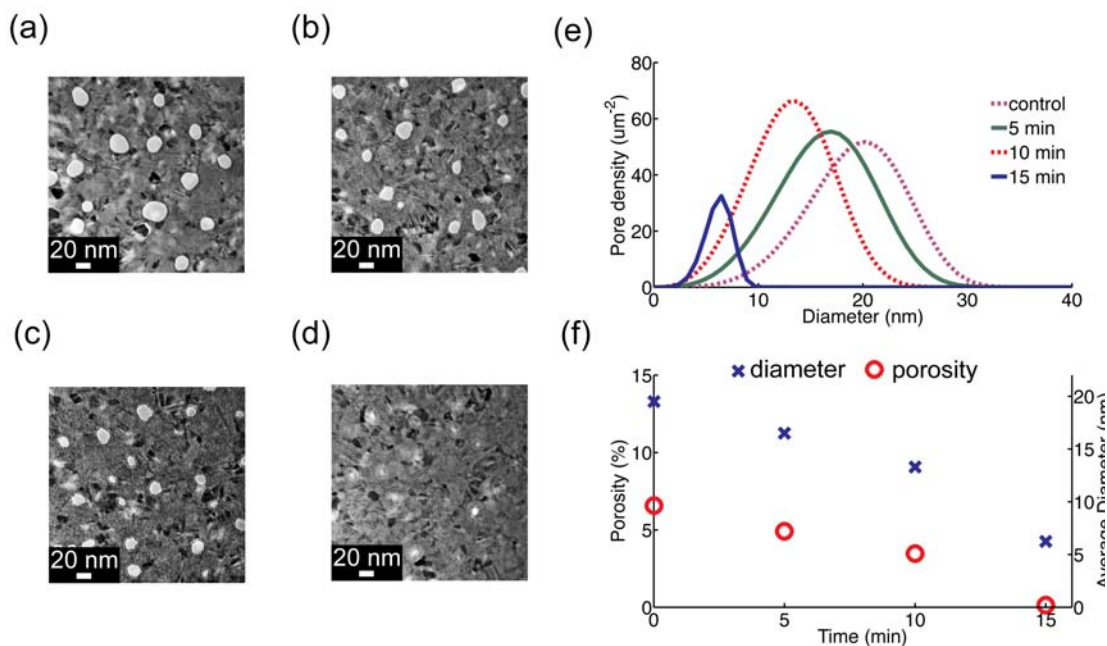


**Figure 5-4.** TEM images of carbonized membranes with 10% of  $\text{C}_2\text{H}_2$  at  $750^\circ\text{C}$  and various soak times: **(a)** untreated, **(b)** 5 minutes, **(c)** 10 minutes. A 15-minute soak time **(d)** occluded the majority of pores. Scale bar is 20 nm. **(e)** Pore size distribution as calculated from TEM images **(f)** Graph showing size (blue 'X') and porosity (red 'O') dependence with treatment time. The standard deviation of porosity and diameter is 0.3% and 0.7 nm, respectively.

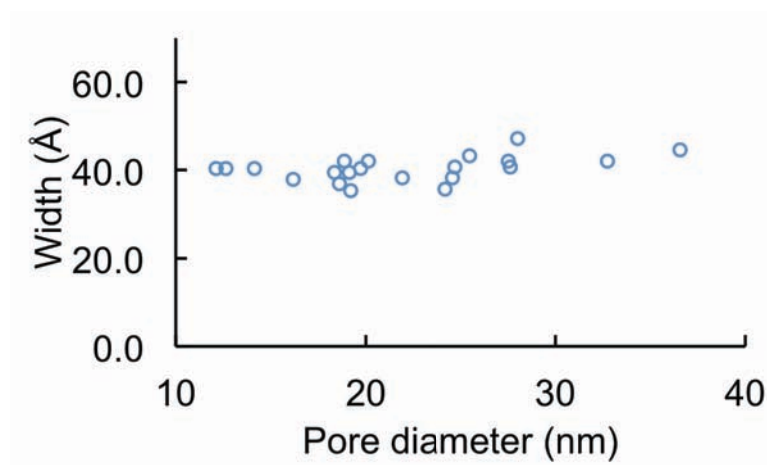


**Figure 5-5.** Width of carbon deposit width versus pore size. The growth rate of carbon is unaffected by pore size.

### 5.1.5 Self-ordering and x-ray spectroscopy

Energy-dispersive x-ray spectroscopy (EDS) was performed on a carbonized pore (750°C for 10 minutes in 10% acetylene) and showed a high density of carbon coating the inner pore wall (Figure 5-6 inset). A closer look at the carbon coating reveals atomic ordering of a few nanometers from the edge of the pore (Figure 5-6). The lattice spacing was measured to be 3.6 Å, consistent with the spacing between graphene layers [116]. It is believed that the first carbon layers adhere to the silicon pore and are stressed due to the lattice mismatch and thus grow as an amorphous  $\text{Si}_{1-x}\text{C}_x$  film. At a critical thickness, the carbon atoms are able to arrange themselves at their characteristic bond length to form ordered layers of graphene. This supports the observation that the growth rate increases with longer carbonization times, possibly due to the transition from  $\text{Si}_{1-x}\text{C}_x$  to graphene formation. These results suggest that pnc-Si may be used as a platform to

create novel hybrid carbon-silicon nanostructures with superior stability, transport and separation properties as compared to existing technologies.

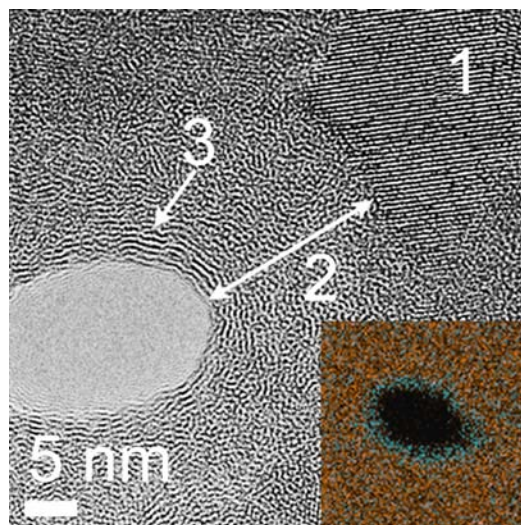


**Figure 5-6.** High-resolution bright field TEM images of a carbonized pore. The inset shows an x-ray energy dispersive x-ray (EDX) scan of a single carbonized pore. The EDX scan highlights areas of Si (red) and C (blue) composition. Label 1 marks a  $\langle 111 \rangle$  oriented Si nanocrystal at the perimeter of the original pore wall. The carbon layer is highlighted by the arrow (2). Atomic ordering can be seen far from the original pore wall consistent with the spacing ( $3.6 \text{ \AA}$ ) between sheets of graphite (3).

### 5.1.6 Chemical stability

As previously demonstrated, carbonization of electrochemically etched porous silicon has improved chemical stability in highly basic etchants such as potassium hydroxide (KOH) [117]. An improvement in pnc-Si membrane stability to harsh alkaline environments after carbonization is observed. Carbonized and untreated samples were soaked in 5% (w/v) KOH (Mallinckrodt Baker, Phillipsburg, NJ) at  $40^\circ\text{C}$  for one hour.

After this time, the untreated membrane had completely dissolved while the carbonized membrane remained intact (Figure 5-7). From these results, it is concluded that carbonization not only coats the inner pore walls of the pnc-Si membrane, but also the planar membrane surface, providing a high quality protective layer for high pH environments experiments and applications. This also confirms that carbonization coats the surface continuously as no areas of chemical attack were present in the carbonized films.

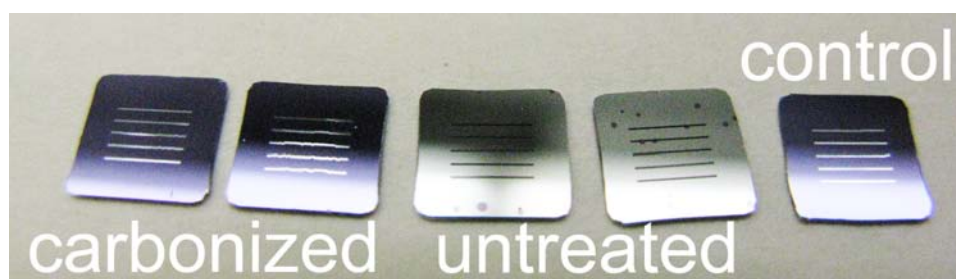


**Figure 5-7.** Carbonized and untreated pnc-Si membranes after 1 hour in 5% KOH at 40°C. The rectangular slits are free-standing pnc-Si. Untreated membranes are discolored indicating the dissolution of the silicon film [56].

### 5.1.7 Hydraulic permeability

A hydraulic permeability study [53, 54] was performed to determine whether carbonization would impact water transport through the membranes. All samples were first ozone treated (Novascan PSD-UVT, Ames, IA) for ten minutes at 120°C in order to create a more hydrophilic surface that facilitated the wetting of pores (Figure 5-8) [53, 54]. It is found that without ozone treatment, hydraulic permeability is hindered due to incomplete wetting of the nanopores. Custom polypropylene vials that could house



ultrathin silicon membranes (SepCon™) were used in water permeability experiments (SiMPore, Inc., West Henrietta, NY). A polydimethylsiloxane (PDMS) Sylgard® 182 elastomer was used to seal the membrane chip to the plastic insert (Dow Corning, Midland, MI). The plastic vial assembly was then loaded into a custom aluminum pressure cell (Figure 5-9). 500 µL of DI water was placed inside the vial and the assembly was sealed with a Viton® gasket. 40 µL of water was placed on the bottom membrane surface (i.e. filtrate side) to initiate wetting of the pores. The vial was pressurized to 3.0 PSI (read using a manometer) for five minutes. Water was collected with an eppendorf tube and the hydraulic permeability was calculated using the expression [54]:

$$\varepsilon = \frac{V}{P \cdot A \cdot t}$$

**Equation 5-1**

where  $\varepsilon$  is the hydraulic permeability,  $V$  is the total volume passed (minus the initial 40 µL used for wetting),  $P$  is the pressure applied,  $A$  is the membrane active area, and  $t$  is the elapsed time.

The Dagan equation [118] for fluid flow through a short pipe was used to predict the permeability of our membranes:

$$Q = \frac{r^3 \Delta P}{\mu \left[ 3 + \frac{8}{\pi} \cdot \frac{l}{r} \right]}$$

Equation 5-2

where  $Q$  is the volumetric flow rate,  $r$  is the pore radius,  $P$  is the pressure drop across the pore,  $\mu$  is the solution viscosity, and  $l$  is the length of the pore. A custom MATLAB script was written to calculate the theoretical permeability using a pore distribution acquired from TEM micrographs [54]. An example of this analysis is shown in Figure 5-10.

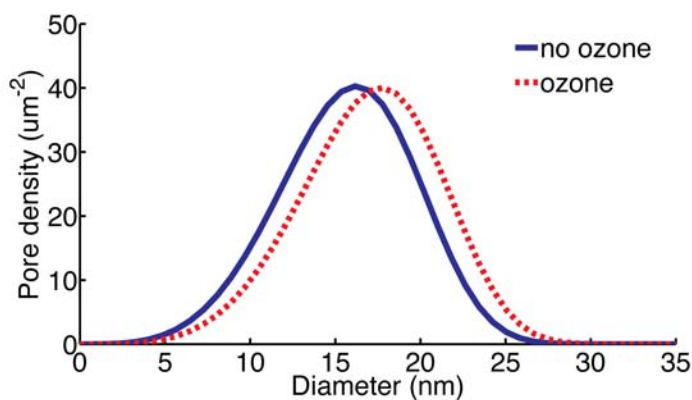


**Figure 5-8.** Pore size distribution of a carbonized membrane before (blue solid) and after (red dashed) ozone treatment. The pores are slightly enlarged after treatment due to the removal of a few carbon layers.

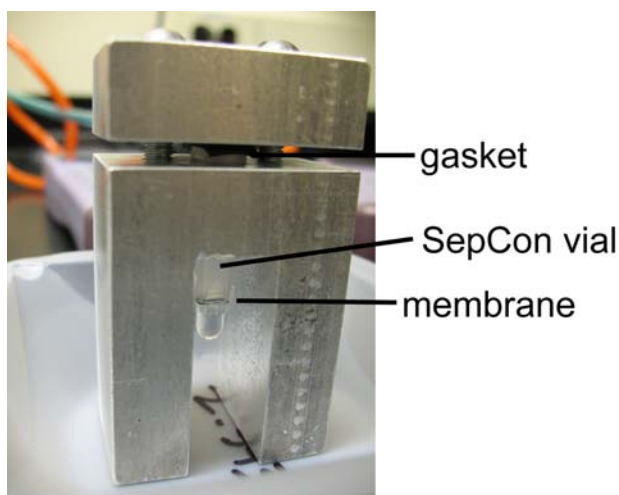


**Figure 5-9.** Aluminum pressure cell used for permeability and filtration experiments. A seal is created by a silicone gasket between the top of the aluminum cell and the plastic SepCon vial. A pnc-Si membrane chip rests at the bottom of the SepCon vial and is sealed with PDMS. Pressure is monitored by a gas manometer attached to the cell inlet.

Three untreated membranes of varying porosities were first tested and compared to the theoretical prediction using the Dagan equation [118] with pore distributions measured by TEM as outlined in Gaborski et al. [54]. A carbonized membrane was then tested and demonstrated permeability consistent with standard theory. In the calculation of theoretical permeability, a slight increase in thickness after carbonization is accounted for due to growth on the planar surface of the membrane. Unlike CNT membranes [27, 28, 119], carbonized pnc-Si does not show an enhancement in water flow (Figure 5-11). Thus, the inherently high permeability of the untreated membranes can only be marginally improved by the very smooth graphene walls from which CNT membranes derive their enhancement from.

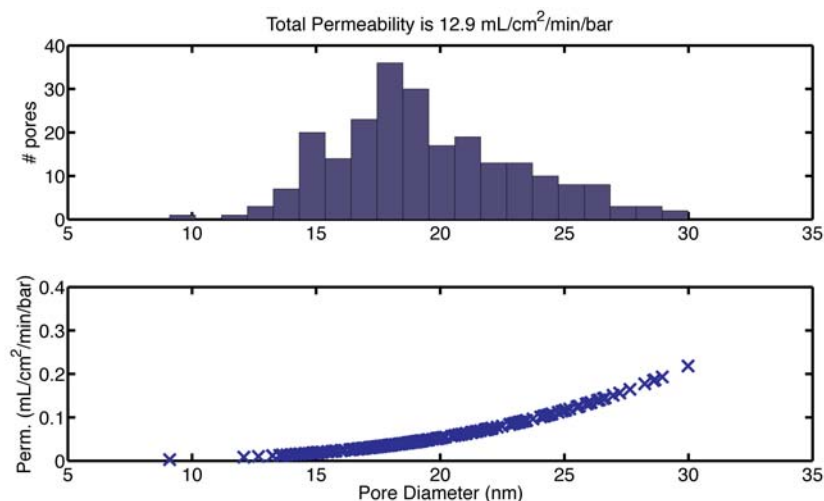


**Figure 5-10.** Calculation of the theoretical hydraulic permeability from the size distribution of an actual membrane using the Dagan equation on a pore-by-pore basis.

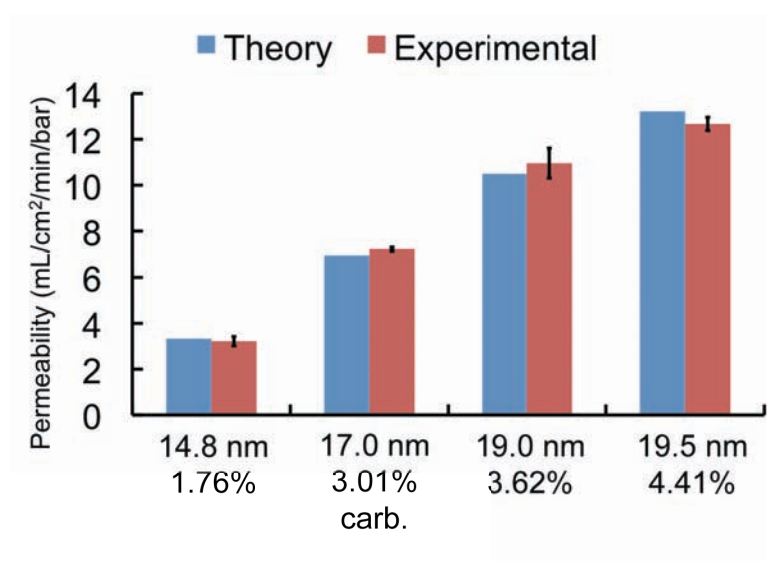


**Figure 5-11.** Hydraulic permeability of untreated and carbonized pnc-Si membranes. The permeability of a carbonized membrane matches the theoretical prediction. The average pore diameter and porosity for each membrane are shown under each bar. The error bars represent the measurement error in flow. It does not include the variability in the pore size calculation from TEM micrographs.

### 5.1.8 Gold nanoparticle filtration

To demonstrate the separation capabilities of carbonized pnc-Si membranes, carbonized and untreated membranes were used to filter differently sized gold colloids as shown previously for untreated membranes [54]. The same pressure cell used in the hydraulic permeability study was utilized for the nanoparticle separation. Stock solutions (0.01% w/v) of gold nanoparticles (British BioCell International, Cardiff, UK) were diluted 1:1 with DI H<sub>2</sub>O. 200  $\mu$ L of diluted gold was placed in assembled plastic inserts with pnc-Si membranes and pressurized to 3 PSI using the pressure cell described in section 5.1.7. Pressure was maintained until approximately one-half of the retentate volume passed through the membrane (typically 5-15 minutes). The retentate and filtrate solutions were recovered and weighed to determine total volume recovery, which was typically 100  $\mu$ L. The retentate solution was pipetted up and down against the membrane five times to maximize recovery of gold that had settled against the membrane. The peak absorbance between 500-550 nm of the retentate and filtrate was measured using a Tecan plate reader (Tecan Group, Männedorf, Switzerland) and compared to stock solution peak values (Figure 5-12). A “blank” scan was taken with distilled water and used to adjust the filtrate readings to account for any discrepancies in absorbance of the plate. Using the volume and concentrations of the retentate and filtrate, percent nanoparticle passage was calculated.

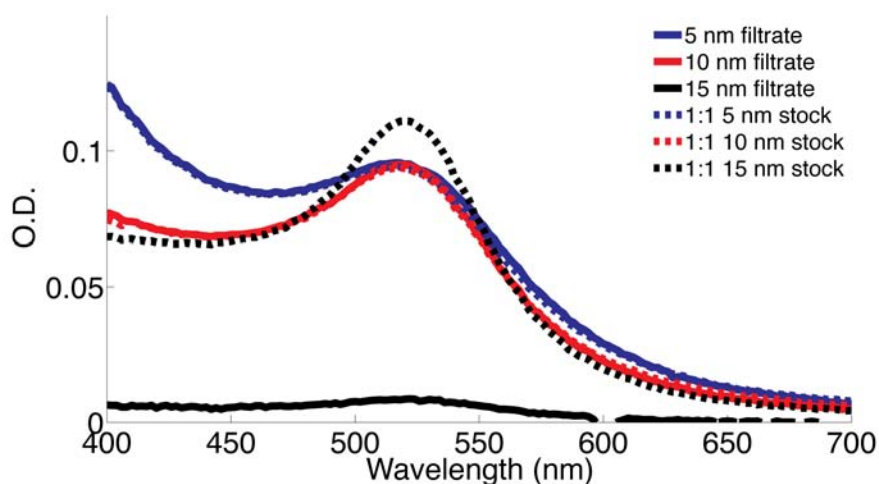


**Figure 5-12.** Raw absorbance scans of filtrate solutions and the 1:1 gold colloid stock dilutions.

As Table 5-1 demonstrates, a carbonized membrane has the ability to separate 6.6 nm from 7.9 nm gold nanoparticles while the untreated membrane passes both the 6.6 nm and 7.9 nm gold but retains 12.7 nm colloids. The sieving coefficients were experimentally calculated by taking the ratio between the filtrate and gold stock concentration. Coating the pore walls with 3 nm of carbon reduced the effective membrane cutoff. The separation was not as sharp as the untreated membrane and may be due to the slight distribution in gold nanoparticle sizes and the non-optimized pore size distribution of the carbonized membrane.

**Table 5-1.** Nanoparticle sieving coefficients ( $C_{\text{filtrate}}/C_0$ ) of an untreated and carbonized membrane

	Avg. gold colloid size measured by TEM		
	6.6 nm	7.9 nm	12.7 nm
<b>untreated</b> <b>avg. dia. 20.7 nm</b>	0.96	0.95	0.08
<b>carbonized</b> <b>avg. dia. 17.0 nm</b>	0.68	0.22	n.d.*

### 5.1.9 Protein filtration

To further demonstrate the potential of carbonized pnc-Si membranes for molecular sieving, an experiment involving three differently sized proteins was performed using a setup similar to that in the gold nanoparticle experiments. Cytochrome c, bovine serum albumin (BSA), and  $\beta$ -galactosidase were purchased from Sigma (St. Louis, MO) and reconstituted in 1x phosphate buffered saline (PBS) at a concentration of 1 mg/mL (w/v). Solutions were spun at 10,000g for 5 minutes to sediment any aggregates or non-dissolved material. The supernatant was recovered and used for the following separation experiments. Concentrations were calculated from fits to standard curves of absorbance at 280 nm (BSA and  $\beta$ -galactosidase) and 410 nm (cytochrome c). The limit of detection was approximately <0.05 mg/mL. Each protein was filtered independently using

---

\* Not detectable. Concentration was less than limit of detection (< 0.05 mg/mL)

identical carbonized membranes so that a sieving coefficient ( $C/C_0$ ) could be calculated using the same method employed in the nanoparticle trials.

Experiments were performed by first placing 200  $\mu\text{L}$  of protein solution in the plastic membrane insert. The bottom side of the membrane was briefly wetted with 1x PBS to initiate flow and then drawn off with a pippeter [54]. The device was pressurized to 3 PSI and experiments were allowed to run until at least 50  $\mu\text{L}$  of filtrate solution could be collected (typically 30 min to 1 hr). The filtrate solution was then measured using the Tecan absorbance scanner. The raw absorbance scans and standard curves are shown in Figure 5-13. A “blank” scan was taken with 1x PBS and used to adjust the filtrate readings to account for any discrepancies in absorbance of the quartz plate.



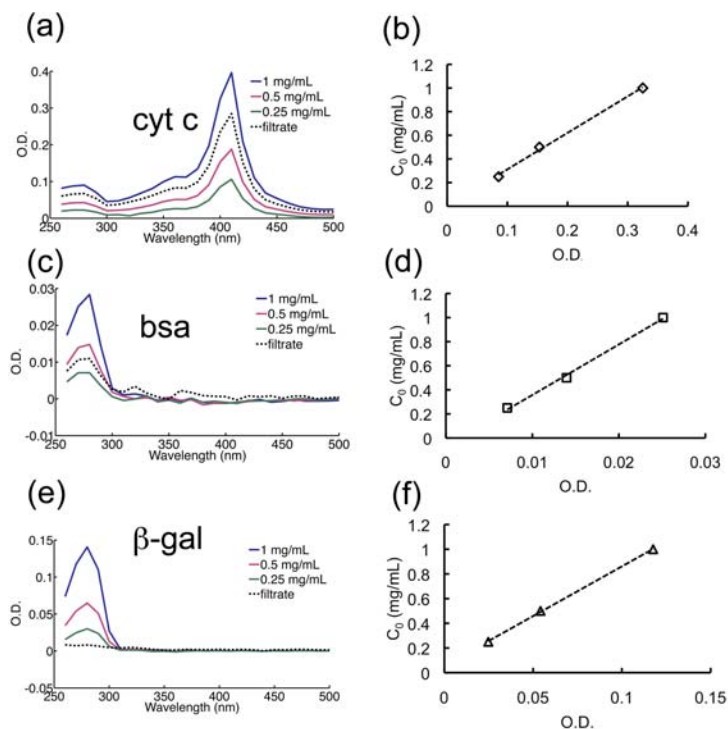


**Figure 5-13.** Raw absorbance data and standard curves. The standard curves were generated by taking the absorbance peak at 280 nm for BSA and β-galactosidase and 410 nm for cytochrome c.

Table 5-2 shows the protein sieving coefficient along with the molecular weight and hydrodynamic size of the proteins as determined by a dynamic light scattering system (Malvern ZetaSizer Nano ZS, Worcestershire, UK) [120]. The results indicate that the smallest protein, cytochrome c passed through relatively unhindered, while albumin transport was hindered, and β-galactosidase was completely held back.

**Table 5-2.** Protein sieving coefficients ( $C_{\text{filtrate}}/C_0$ ) of carbonized membranes with an average diameter of 17.8 nm

Protein	MW	Diameter (nm)	$C_{\text{filtrate}}/C_0$
Cytochrome c	14 kD	$4.2 \pm 1$	0.73
Albumin	67 kD	$11.1 \pm 4$	0.39
$\beta$ -galactosidase	460 kD	$15.5 \pm 4.8$	n.d.*

### 5.1.10 Conclusions

In this section, a novel method for coating silicon nanopores with carbon has been demonstrated. The thickness of the coating can be controlled with sub-nanometer precision by varying soak temperature and soak time. Pore diameters can be reduced by as little as 1 nm to greater than 25 nm for complete occlusion, thus allowing for more careful control over sieving characteristics. Hydraulic permeability studies have shown that carbonized membranes follow theoretical predictions for water transport and retain the nanoparticle separation capabilities of the untreated ultrathin membrane. Additionally, the potential use of carbonized pnc-Si membranes in molecular separations has been shown. These results demonstrate that carbonization is a simple and effective method for significantly improving the chemical stability of ultrathin silicon membranes, enables precise tuning of nanopores, and has potential for use in a wide range of sieving applications.

---

\* Not detectable. Concentration was less than limit of detection (< 0.05 mg/mL)

## 5.2 Atomic layer deposition

### 5.2.1 Introduction

Atomic layer deposition (ALD) is a chemical vapor deposition technique used to very accurately coat surfaces with a uniform thin film. One of the benefits of ALD is that it can coat high aspect ratio features approaching 140:1, making it suitable for functionalization of porous materials [121]. Several researchers have demonstrated that ALD can be successfully employed in modifying the size of porous membranes [106, 121-126]. Figure 5-14 shows a cartoon depicting one cycle of the atomic layer deposition of aluminum oxide. Precursor vapors are introduced into a chamber serially with an evacuation period in between “pulses”. Each pulse saturates the sample surface and reacts with the precursor species to form a single molecular layer of product film. Deposition in this manner allows for precise control over the exact thickness of the film, thus making ALD a very attractive technique for controlling the size of nanopores.

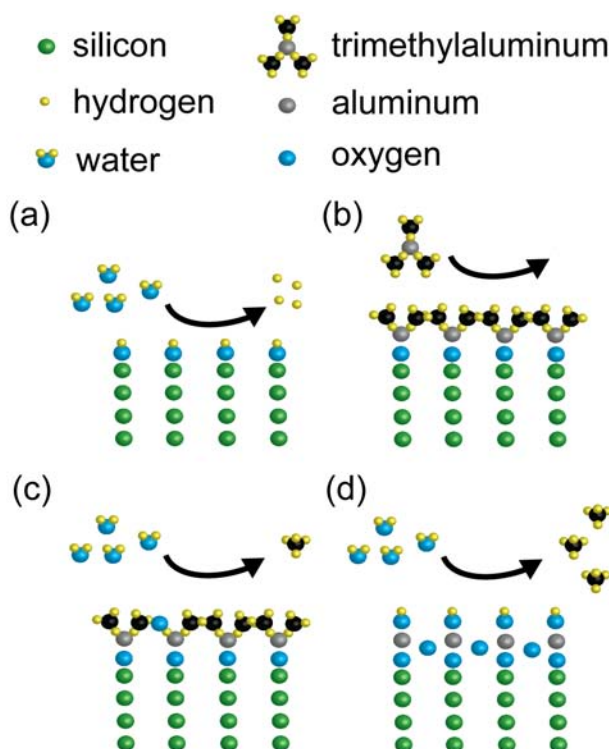


**Figure 5-14.** Cartoon showing one cycle of aluminum oxide growth on silicon by atomic layer deposition. **(a)** Water vapor hydroxylates the silicon surface. **(b)** Trimethylaluminum is introduced and reacts with the surface hydroxyl groups. Unreacted precursor molecules are evacuated from the chamber before a second pulse of water is injected. **(c) - (d)** Water is pulsed and reacts with the surface to form hydroxylated aluminum oxide. Methane is produced as a byproduct gas. Unreacted water and methane is purged before step **(b)** is repeated.

### 5.2.2 Atomic layer deposition of aluminum oxide

Atomic layer deposition of aluminum oxide ( $\text{Al}_2\text{O}_3$ ) was performed in a Cambridge NanoTech Savannah S200 system (Cambridge, MA). The chamber supports wafers up to 8 inches (200 mm), but for experimental purposes individual membrane chips were loaded into the tool. Chips were placed on top of two glass coverslips so that vapor was

accessible to both the top and bottom of the pnc-Si membrane. The chamber was heated to 250°C and pumped to a base pressure of 10 mTorr. 20 sccm of argon was flowed throughout the process to help purge any unreacted precursor. Pulses of water and trimethylaluminum lasting 50 milliseconds were introduced into the chamber with five seconds of purging/evacuation in between each pulse. Each cycle deposited 1.1 Å of material.

### **5.2.3 Pore size control using atomic layer deposition of aluminum oxide**

By taking advantage of the precise control in deposition thickness that ALD provides, pore sizes can be tuned with sub-nanometer precision. A deposition rate of 1.1 Å per cycle was assumed based on calibrations performed by the tool manufacturer. Figure 5-15 shows that pore sizes can be adjusted by simply changing the number of deposition cycles. The pore size histogram confirms that the deposition has shifted the pore diameters by the targeted amount. High-resolution TEM confirms that the aluminum oxide deposition is highly conformal. This form of pore size control will undoubtedly be useful in size-based separations of nanometer-sized objects. Atomic force microscopy performed on a pnc-Si membrane coated with 5 nm of aluminum oxide showed a RMS roughness similar to that of a bare membrane (0.3 nm).

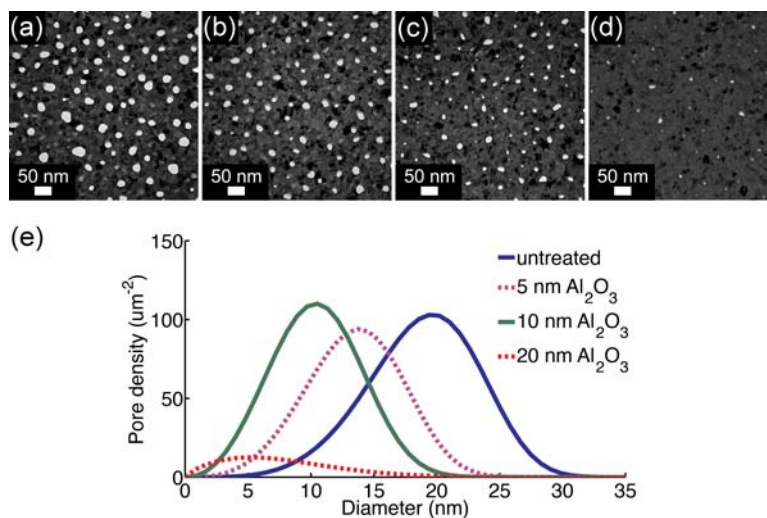


**Figure 5-15.** TEM micrographs of an (a) untreated and (b) – (d) alumina-coated pnc-Si membranes. The treated membranes were coated with (b) 5 nm, (c) 10 nm, and (d) 20 nm of  $\text{Al}_2\text{O}_3$ . (e) The pore size histogram shows that the distribution shifts by the thickness of deposition (multiplied by a factor of two because the coating is conformal along the pore wall).

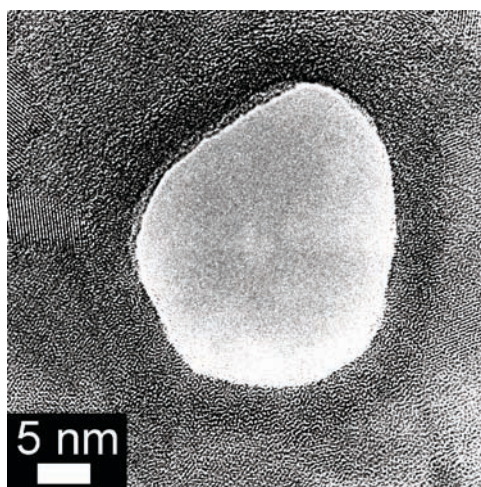


**Figure 5-16.** High-resolution TEM micrograph of an aluminum oxide coated nanopore.

A second consequence of the aluminum oxide treatment is that the membrane surface becomes more hydrophillic, as evidenced by the contact angle measurements shown in Figure 5-18.

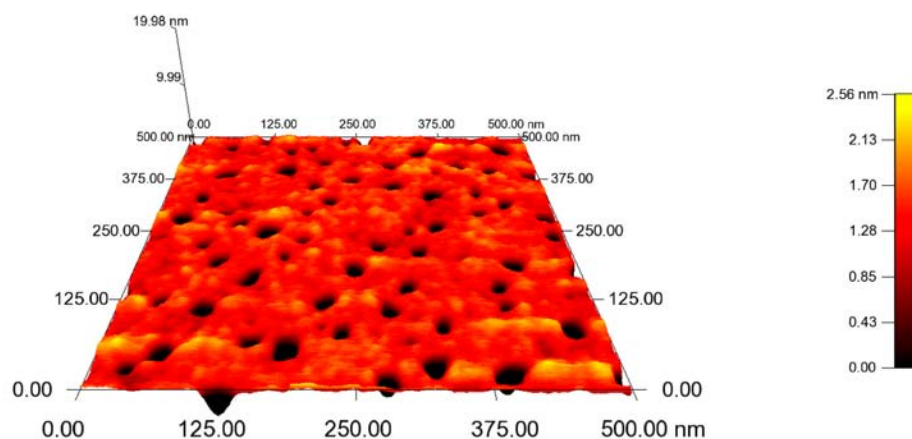


**Figure 5-17.** Atomic force microscopy scan of a pnc-Si membrane coated with 5 nm of aluminum oxide. RMS surface roughness was calculated to be 0.3 nm.

Although the contact angle decreases with the alumina coating, functional testing showed that hydraulic permeabilities were inconsistent and lower than expected. An oxygen plasma treatment was performed to further increase the hydrophilicity (Yield Engineering Systems YES-1224P, Livermore, CA). After treatment, water flow could be established immediately and hydraulic permeabilities consistently matched predicted values.



**Figure 5-18.** Water contact angles of (from left to right) an untreated ( $83^\circ$ ), oxygen plasma treated ( $14^\circ$ ), alumina-coated ( $56^\circ$ ), and alumina and oxygen plasma treated ( $18^\circ$ ) pnc-Si membrane chip.

#### 5.2.4 Gold nanoparticle filtration

An experiment, similar to the one described in section 5.1.8, was performed on alumina-coated membranes. Table 5-3 shows the sieving coefficients of the untreated and alumina-coated pnc-Si membranes to gold nanoparticles of different sizes. The membrane with the largest pore size (untreated) passed the largest nanoparticle, while the membranes coated with 5 nm and 10 nm  $\text{Al}_2\text{O}_3$  rejected the largest and medium nanoparticles, respectively. Although the treated membranes did hold back the larger nanoparticles, it is believed that with more experimentation the sharpness of separation can be improved upon. Electrostatic interactions between the pore wall and nanoparticle should also be considered when designing the pore size distribution for optimal separation performance.



**Table 5-3.** Nanoparticle sieving coefficients ( $C_{\text{filtrate}}/C_0$ ) of an untreated and alumina-coated membranes

	Avg. gold colloid size measured by TEM		
	6.6 nm	7.9 nm	12.7 nm
<b>untreated</b> <b>avg. dia. 24 nm</b>	-	-	0.82
<b>Al<sub>2</sub>O<sub>3</sub> 5 nm</b> <b>avg. dia. 19 nm</b>	-	0.51	0.14
<b>Al<sub>2</sub>O<sub>3</sub> 10 nm</b> <b>avg. dia. 14 nm</b>	0.64	n.d.*	n.d.*

### 5.2.5 Conclusions

In this section, atomic layer deposition of aluminum oxide has been shown to be a simple yet precise method for adjusting the pore sizes of pnc-Si membranes. Gold nanoparticles of different sizes have been successfully filtered using alumina-coated membranes. This simple demonstration of functionality should motivate future studies into other films that may be deposited by atomic layer deposition and provide additional benefits.

---

\* Not detectable. Concentration was less than limit of detection (< 0.05 mg/mL)

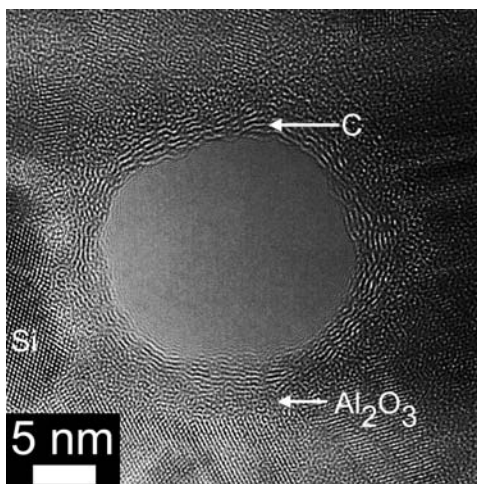
## **5.3 Carbon growth on alumina-coated porous nanocrystalline silicon membranes**

### **5.3.1 Introduction**

In the previous sections, two methods for pore size control and functionalization were presented. Here, a process incorporating both techniques is described.

### **5.3.2 Ordered carbon growth**

Motivated by recent work involving carbon growth on porous anodized aluminum oxide (AAO) templates [127, 128], an experiment was carried out where a pnc-Si membrane was first coated with 1.5 nm of  $\text{Al}_2\text{O}_3$  (using the conditions described in section 5.2.2) followed by a rapid thermal carbonization treatment at 750°C for one minute in 10% acetylene. The hypothesis was that the alumina coating on pnc-Si would create a surface similar to AAO and ordered carbon growth would initiate.



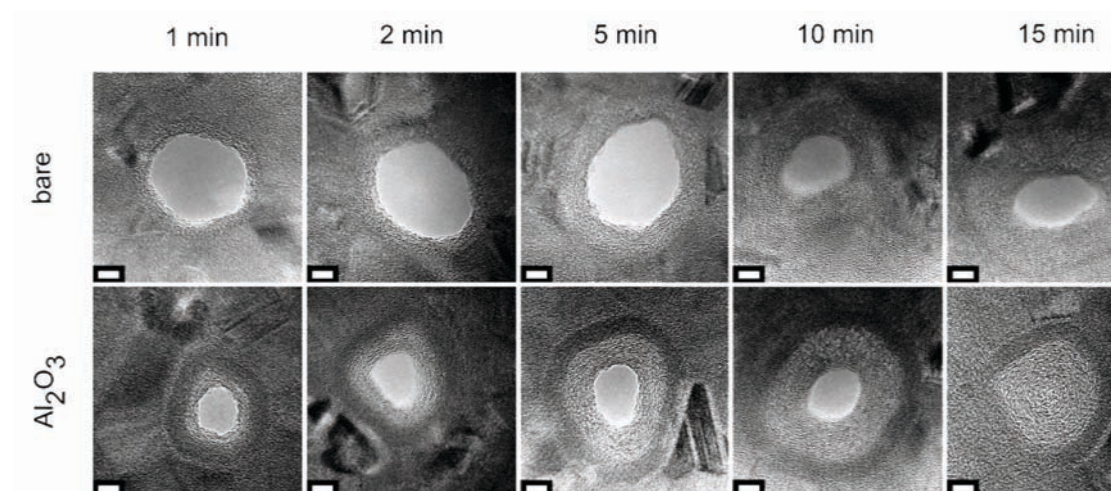
**Figure 5-19.** High-resolution TEM micrograph of a pnc-Si nanopore coated with aluminum oxide and graphene.

Figure 5-19 shows a pnc-Si membrane pore coated with a thin layer of alumina followed by ordered carbon. Unlike carbonization of bare pnc-Si, ordered carbon growth appears to start immediately at the alumina interface. This is not surprising since AAO has been well established as a template for carbon nanotube synthesis. This type of hybrid nanoporous membrane may have potential as a highly permeable membrane due to the material thinness as well as the ultra-smooth carbon wall.

### 5.3.3 Pore size dependent carbon growth on alumina-coated porous nanocrystalline silicon membranes

In order to calculate the rate of carbon growth on aluminum oxide coated pnc-Si membranes, carbonization was performed for five different time periods on membranes coated with 2.5 nm of aluminum oxide. The carbonization temperature was fixed at 750°C with the acetylene and argon flow rate set to 1 and 9 lpm, respectively.

Carbonization on uncoated membranes was performed side-by-side to serve as a point of comparison.



**Figure 5-20.** High-resolution TEM micrograph of uncoated and alumina-coated membranes carbonized for different time periods. The scale bars are 5 nm

Figure 5-20 shows a series of high-resolution TEM micrographs of the uncoated and alumina-coated membranes that have been carbonized for different time periods. One structural difference that becomes apparent is that the carbon layer is much more ordered on the alumina surface. That is, continuous rings of carbon are observed on the alumina-coated pore whereas only local ordering is achieved on the bare silicon pore. The spacing between the carbon rings was measured to be consistent with the distance between sheets of graphene.

The rate of carbon growth on both the bare and alumina surfaces was calculated by measuring the thickness of the carbon wall that had developed after the carbonization treatment.

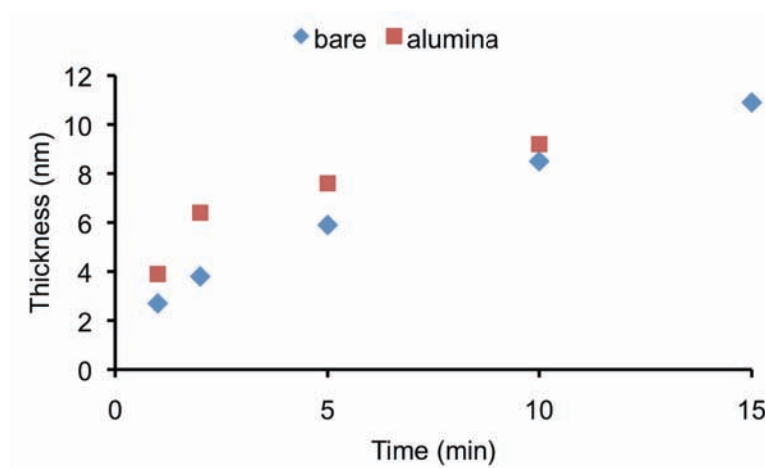


**Figure 5-21.** The thickness of carbon deposited on a bare silicon and alumina surface after carbonization versus process time. The 15-minute time point on the alumina surface could not be calculated since all the pores had been occluded after treatment.

Figure 5-21 shows a plot of the thickness of carbon along a bare and alumina-coated pore wall after carbonization for several time periods. Carbon growth on a bare Si pore wall is linear through 15 minutes, whereas carbon growth on an aluminum oxide surface appears to be logarithmic. This would indicate that carbonization on an alumina surface is growth limited and is dependent on the pore size. Another way of interpreting this data is that as the radius of curvature increases, i.e. the pore size decreases, the amount of energy needed to form ordered rings of carbon increases. Thus, the growth rate must decrease for smaller pore sizes.

The non-linear growth rate of carbon on alumina-coated pores can be exploited in the design of sharper cut-off membranes. Because larger pores occlude at a higher rate, the tail of a pore size distribution will become increasingly narrow with longer treatment times. In Figure 5-22, the pore size distributions after carbonization on a bare and

alumina-coated pnc-Si membrane are shown. Only the “right-half” of the distribution is shown to highlight the change in cut-off sharpness after carbonization on an alumina surface. The distributions were fit with a Gaussian tail using a least-squares algorithm in MATLAB.

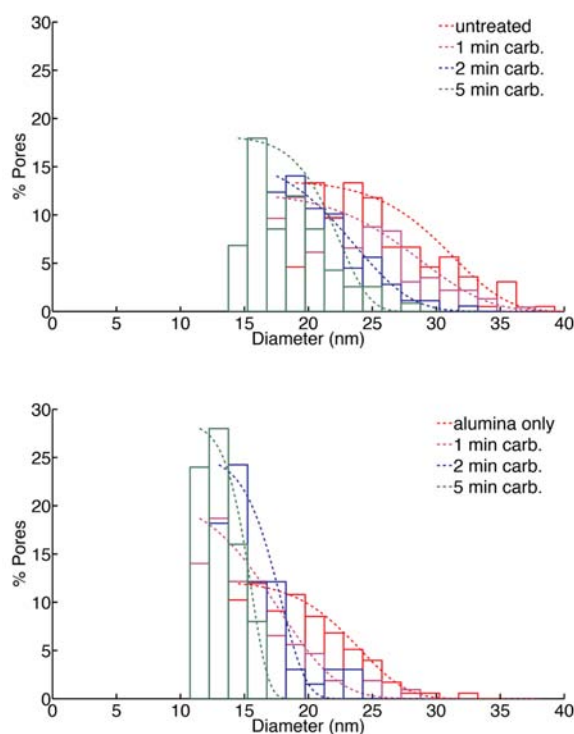


**Figure 5-22.** Pore size distributions after carbonization on a bare (top) and alumina-coated (bottom) membrane. The data is presented as a percent of total pore population. A Gaussian fit was applied to the histograms in order to visualize the increase in pore size cut-off sharpness in the carbonized alumina-coated membrane.

Comparing the distribution of a carbonized bare and alumina-coated membrane, a clear difference in growth modes is observed. This is reflected by the dramatic change in the shape of the pore size distribution. The cut-off sharpness increases with longer

carbonization times on the alumina-coated membrane, whereas carbonization on a bare membrane simply shifts the entire distribution to smaller pore sizes.

### **5.3.4 Conclusions**

In this section, a method for increasing the cut-off sharpness of a porous nanocrystalline silicon membrane was presented using atomic layer deposition of aluminum oxide followed by rapid thermal carbonization. This is achieved by taking advantage of the non-linear growth rate of ordered carbon on an alumina pore. This technique should have widespread applicability in the design of a highly accurate nano-sieve.

## Chapter 6. Future directions

### 6.1 Crystallization and pore formation

In section 2.8, it was established that pore formation occurs during the solid phase crystallization of amorphous silicon and that many factors contribute to the ultimate morphology of these nano-membranes. However, the physical parameters that determine the ultimate pore morphology have not been determined. Our experience has shown that the initial stress state, density of the amorphous silicon layer, and degree of crystallization greatly affects the nanostructure of pnc-Si. Higher temperature thermal treatments will yield larger pores. But in order to form a physical model of void formation in the nanocrystalline films, sophisticated characterization techniques must be employed to investigate the stresses in the deposited films and the degree of crystallization after thermal annealing.

The use of the bulge test, as demonstrated in section 4.5.1, to quantify the stresses and strain in films deposited under different conditions will be presented. The strain state of a particular membrane can be controlled by varying deposition conditions like substrate bias and temperature, or different methods of deposition such as direct or reactive sputtering of oxide. Furthermore, the investigation of different silicon dopants may prove useful in uncovering how these nano-voids form. Using the stress-strain data, a correlation between different initial stress states in the membrane can be made with



pore morphology. This will provide valuable information into further controlling the pore formation mechanism.

Small angle x-ray scattering (SAXS) spectroscopy is a technique that has been employed to investigate the crystalline fraction of nanocrystalline silicon [129]. This method directs a highly uniform beam of monochromatic x-ray at small angles ( $0.1 - 10^\circ$  from perpendicular) at a sample. A detector behind the sample measures the scattering intensity of the beam. By using this technique, a correlation can be made between varying crystalline volumes and membrane morphology, which will give further insight into the relationship between crystallization and void formation.

In section 3.5 the importance of point defects in relation to silicon nanocrystal and pore growth was discussed. At this point in time, no direct quantification into the density of point defects in the starting amorphous silicon has been made. A technique such as electron paramagnetic resonance (EPR) may be employed in the study of defects. The hypothesis is that a certain threshold level of defects must be achieved in the deposited amorphous silicon before crystallization and pore formation can proceed. However, a high density of defects may have a negative impact on pore nucleation and growth.

## **6.2 Porous nanocrystalline silicon for use in fuel cells**

Fuel cells have generated a significant amount of attention from the scientific and industrial community due to their high-energy conversion efficiency. A large portion of this interest is directed at improving the materials used to construct fuel cells [130, 131]. Figure 6-1 shows a typical electrochemical reaction as well as the major components in a

fuel cell. A good fuel cell should have an ion exchange membrane that possesses high ionic conductivity, stability in oxidizing and reducing environments, low fuel crossover, sufficient mechanical strength, and be easy to manufacture.

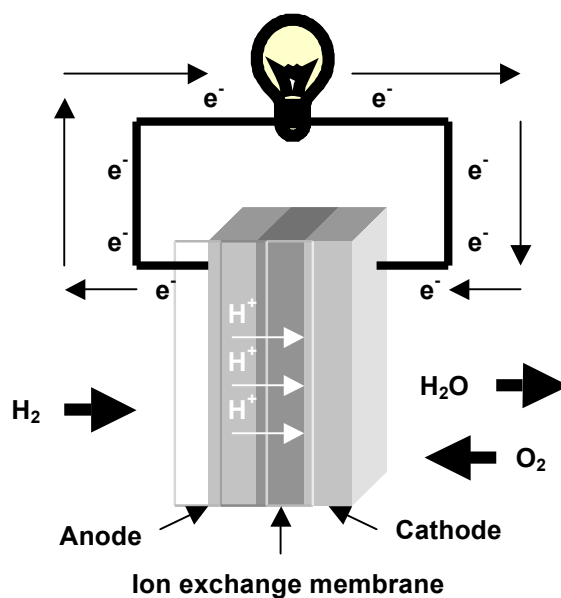


**Figure 6-1.** Simplified hydrogen fuel cell structure. Oxidation occurs at the anode and creates protons, which are permeable through the ionic membrane. Electrons travel through an electronic conductor to generate current through a load. Reduction occurs at the cathode where hydrogen ions, electrons, and oxygen form water.

The current standard in polymer exchange membranes is Nafion by DuPont, a commercially available perfluorinated electrolyte (membrane). The use of functionalized porous silicon (p-Si) as an ionic membrane has also been investigated [20]. Silicon has the benefit of being compatible with solid-state technologies. It is intrinsically scalable, allowing integration into microelectronic devices and larger-scale applications using stacked-cell configurations. The difference between pnc-Si membranes and those made

of p-Si or polymers is the thickness of material. Pnc-Si can be made to be one hundred times thinner thus enhancing transport efficiency.

Molecular hydrogen does not exist by itself naturally and it is necessary to separate it from other gaseous compounds (oftentimes carbon dioxide) before being used as a renewable source of fuel. Current separation techniques employ the use of polymer, metallic/alloy, and silica/zeolite membranes [132]. One disadvantage of polymeric membranes is their temperature sensitivity. In many industrial applications, hydrogen is extracted by steam reforming of hydrocarbons followed by a process to isolate the molecular  $H_2$  from  $CO_2$ . Due to the high operating temperature involved, polymeric membranes cannot be used. Pnc-Si membranes, however, have shown stability at elevated temperatures. While metallic membranes show almost perfect selectivity, they rely on complex manufacturing techniques where thin metallic films must be deposited on an underlying microsieve support [133]. Silica membranes also suffer from this reliance on intermediate support layers which extends membrane thickness to tens of microns [134]. For many of the same reasons pnc-Si would offer advantages over existing fuel cell membranes, non-porous nanocrystalline silicon membranes could provide improved performance in the separation of hydrogen.

One major drawback of both polymeric and p-Si based membranes is the physical thickness of the membrane. Porous silicon membranes are typically  $40\ \mu m$  -  $70\ \mu m$  thick and Nafion  $20\ \mu m$  –  $200\ \mu m$  thick. Porous nanocrystalline silicon is a novel material that is nanometers thick. By decreasing the thickness of a proton exchange membrane, the distance ions travel from anode to cathode is reduced therefore enhancing proton conductivity.

There are two sources of loss in a fuel cell system due to charge transport. The first concerns electrons traveling through a conductor. Typically, the resistance encountered by the electron is small compared to ionic resistance i.e. hydrogen transport through an ionic membrane. The voltage loss,  $\eta_{ohmic}$ , is due to an area-specific/normalized resistance (ASR) and related to the load current density,  $j$ .

$$\eta_{ohmic} = j \times ASR$$

**Equation 6-1**

The ASR is directly proportional to the thickness of the membrane material,  $L$ , and inversely proportional to the conductivity of the ionic species,  $\sigma$ .

$$ASR \propto \frac{L}{\sigma}$$

**Equation 6-2**

The conductivity of a membrane is proportional to concentration and the diffusivity of the carrier through a membrane. Reducing the thickness of a membrane along with chemical functionalization of the surface will decrease the ASR. In fact, pnc-Si membranes have shown rates that approach free diffusion in the case of dye transport. Thus, from Equation 6-1 and Equation 6-2 it is evident that decreasing the thickness of

an ion exchange membrane will reduce the ohmic voltage loss and increase the fuel cell operating voltage (Figure 6-2) and output power density.

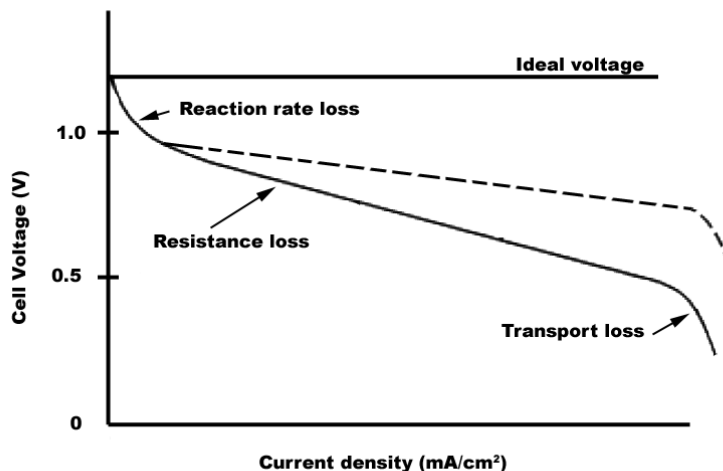


**Figure 6-2.** A typical fuel cell current-voltage characteristic curve [135]. The linear region in the middle of the curve is due to resistive losses. By decreasing the resistance an increase in operating voltage is achieved as demonstrated by the dashed line.

In order for pnc-Si to become a practical proton exchange membrane, fuel crossover must be low i.e. the membrane must be impermeable to the fuel. Because many common fuels are small molecules e.g. methanol, they will readily diffuse across a “porous” membrane. However, it may be possible to design a nanocrystalline membrane that allows for ion transport along grain boundaries and interstitial sites, while holding back the fuel.

### 6.3 Multi-stage microfluidic separation systems

The separation of biomolecules for analysis is a common procedure in biology. For example, separation methods are commonly employed in the study of glycosylation, a post-translational protein modification that affects the structural and chemical stability of the biomolecule. Understanding this process is of great importance in the development of protein drugs. Common methods for studying glycosylation involve the digestion of proteins by endoproteases, separation of protein fragments and glycans by chromatography, and downstream analysis by mass spectroscopy [136]. This process is long and oftentimes state-of-the-art size exclusion chromatography (SEC) is unable to separate these complex carbohydrate mixtures [137], thus making analysis difficult due to limits in resolution. Chromatography also has the disadvantage of requiring large sample volumes and suffers from high losses due to non-specific adsorption [138]. This problem is magnified by the fact that glycopeptides constitute only a small fraction of total peptide mixture. Another method for analysis is by gel electrophoresis, typically SDS-PAGE. However, complete separation of glycoforms is difficult due to the heterogeneous glycosylation pattern [139]. Additionally, the need for a low volume and high-throughput analytical device is desirable in early-stage protein drug development.

Porous nanocrystalline silicon (pnc-Si) integrated in a cross-flow microfluidic device is a perfect candidate for efficient isolation of biomolecules that can be extracted downstream for detection and characterization (Figure 6-3). This method would enable the study of biomolecules previously inhibited by the limitations in time and analysis sensitivity. The hypothesis is that implementing this device for pre-filtering before mass

spectroscopy will *greatly improve the resolution, sensitivity, and speed of existing state-of-the-art techniques for detection at low volumes.*

Miniaturized bio-analytical devices have benefited greatly from the advancement of microfluidic technologies. These devices have several advantages over their bench-top counterparts including smaller dead volume and sample consumption, shorter analysis time, lower cost, greater portability, and improved separation resolution for complex mixtures [140]. Several studies have already reported integration of polymeric or track-etched membranes for size separation of analytes into microfluidic platforms [141, 142]. Pnc-Si offers several advantages over these existing materials.

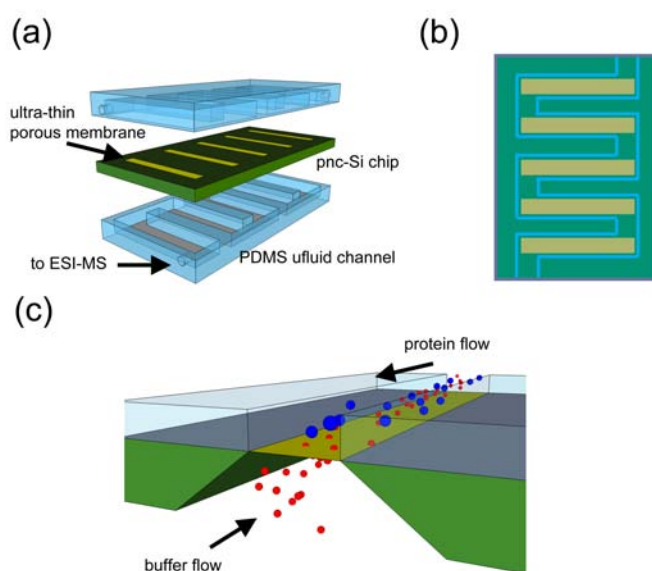


**Figure 6-3.** (a) Proposed microfluidic protein separation device. A pnc-Si membrane chip is sandwiched and sealed in between two PDMS serpentine channel pieces. Inlet and outlet ports provide access to the pumping mechanism and fluid reservoir (not shown). (b) Top-down view showing alignment of the fluidic channel with the membrane area (c) A cross-sectional schematic showing separation in a cross-flow configuration.

First, pnc-Si is an ultra-thin (15 nm) and robust material shown to have high transport rates. This is in comparison to the relatively thick polymeric and track-etched membranes ( $> 1 \mu\text{m}$ ) that are commonly used today. Integrating pnc-Si membranes for protein separation will greatly decrease the analysis time, the majority of which is due to the diffusion of analyte across the size-selective permeable membrane. Second, pore size distributions can be precisely controlled, either during manufacturing or post-production by surface modification methods [55] thus allowing for precise and lossless separation of the species under study. The third advantage is that analyte loss due to the adsorption to internal membrane surfaces is minimized due to the low internal surface area of pnc-Si membranes. Fourth, pnc-Si can take advantage of the wide variety of silanization chemistries available for further functionalization. And fifth, silicon has been shown to be compatible with common microfluidic device materials such as poly(dimethylsiloxane) (PDMS) [143, 144] and SU-8 [145].

Future studies may include a multi-stage device in which membranes with different size cut-offs will be placed on top of each other separated by fluidic channels (Figure 6-4). This will enable “binning” of different sized species, which can then be extracted for downstream analysis. This device structure was previously impossible due to the low



transport rates of polymer membranes since analysis times would be increasingly prohibitive with each stage of separation. With pnc-Si, record diffusion rates are achieved across the membranes enabling the multi-stage format to be realized. Additionally, because of its sharp separation capability with minimal loss, membranes with a difference in cutoffs between 5 and 10 nm will efficiently isolate glycopeptides from non-glycosylated peptides (5 – 10 nm in hydrodynamic size) and allow for the analysis of each species independently. This device will enable the study of composition *and* structure of complex proteins that were prohibitively difficult to analyze with previous techniques.

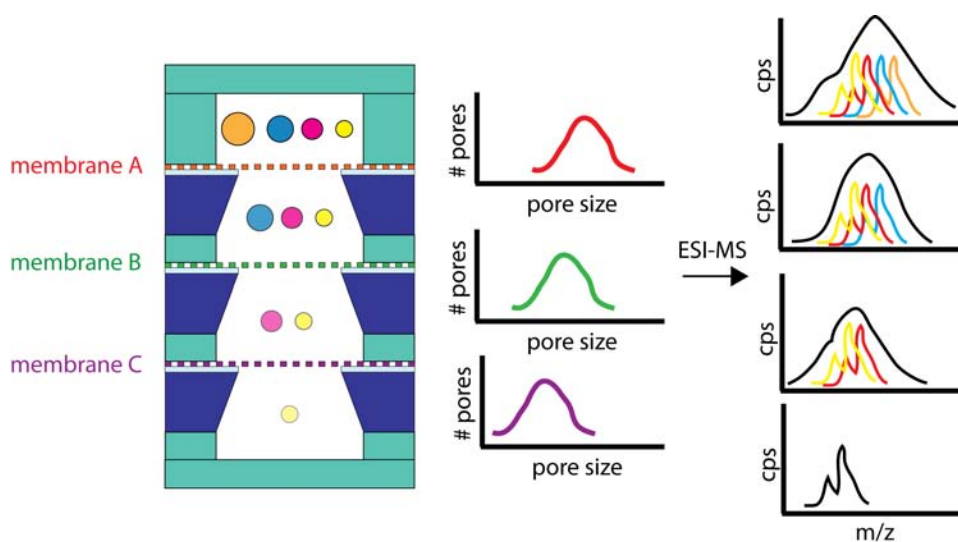


**Figure 6-4.** This cartoon demonstrates the benefit of a multi-stage membrane scheme (left). A complex mixture is introduced in the top stage. Membrane A passes all species except for the largest. There is a slight loss of concentration in the membrane A filtrate due to diffusion limits. With each successive stage, larger species are retained while the smallest pass through. Membrane distributions (center) will be chosen for optimal transmission/retention. Each channel will be fed to a mass spectrometer for analysis. The ability to isolate a small species not resolvable in the unfiltered channel is demonstrated (right).

## 6.4 Conclusions

Porous nanocrystalline silicon membranes are an enabling technology. This chapter has highlighted only a few applications in which this pnc-Si can be used towards. As our understanding of this material increases, it is reasonable to believe that the possibilities will continue to grow.

## References

- [1] National Nanotechnology Initiative. "What is Nanotechnology?". Available: <http://www.nano.gov/html/facts/whatIsNano.html>
- [2] The Project on Emerging Nanotechnologies. "Nanotechnology Consumer Products Inventory". Available: <http://www.nanotechproject.org/inventories/consumer/>
- [3] B. Caughey and P. T. Lansbury, "Protofibrils, Pores, Fibrills, and Neurodegeneration: Separating the Responsible Protein Aggregates from The Innocent Bystanders," *Annu. Rev. Neurosci.*, vol. 26, pp. 267-298, 2003.
- [4] A. Saxena, *et al.*, "Membrane-based techniques for the separation and purification of proteins: An overview," *Adv. Colloid Interfac.*, vol. 145, pp. 1-22, 2009.
- [5] S. Loh, *et al.*, "Interplay among membrane properties, protein properties and operating conditions on protein fouling during normal-flow microfiltration," *J. Membrane Sci.*, vol. 332, pp. 93-103, 2009.
- [6] J. Fu, *et al.*, "Artificial molecular sieves and filters: a new paradigm for biomolecule separation," *Trends Biotechnol.*, vol. 26, pp. 311-320, 2008.
- [7] R. van Reis and A. Zydney, "Bioprocess membrane technology," *J. Membrane Sci.*, vol. 297, pp. 16-50, 2007.
- [8] S. Rao and A. L. Zydney, "Controlling protein transport in ultrafiltration using small charged ligands," *Biotechnol. Bioeng.*, vol. 91, pp. 733-742, 2005.
- [9] J. Fu, *et al.*, "Nanofilter array chip for fast gel-free biomolecule separation," *Appl. Phys. Lett.*, vol. 87, p. 263902, 2005.

- [10] S. Song, *et al.*, "Microchip Dialysis of Proteins Using in Situ Photopatterned Nanoporous Polymer Membranes," *Anal. Chem.*, vol. 76, pp. 2367-2373, 2004.
- [11] Z. Chen, *et al.*, "DNA translocation through an array of kinked nanopores," *Nat. Mater.*, vol. 9, pp. 667-675, 2010.
- [12] S. M. Iqbal, *et al.*, "Solid-state nanopore channels with DNA selectivity," *Nat. Nano.*, vol. 2, pp. 243-248, 2007.
- [13] M. E. Gracheva, *et al.*, "Simulation of the electric response of DNA translocation through a semiconductor nanopore-capacitor," *Nanotechnology*, vol. 17, p. 622, 2006.
- [14] A. J. Storm, *et al.*, "Translocation of double-strand DNA through a silicon oxide nanopore," *Phys. Rev. E*, vol. 71, p. 10, May 2005.
- [15] J. Nakane, *et al.*, "A Nanosensor for Transmembrane Capture and Identification of Single Nucleic Acid Molecules," *Biophys. J.*, vol. 87, pp. 615-621, July 1, 2004 2004.
- [16] A. Aksimentiev, *et al.*, "Microscopic Kinetics of DNA Translocation through Synthetic Nanopores," *Biophys. J.*, vol. 87, pp. 2086-2097, September 1, 2004 2004.
- [17] C. Kuan-Lun, *et al.*, "A nanoporous silicon membrane electrode assembly for on-chip micro fuel cell applications," *J. Microelectromech. S.*, vol. 15, pp. 671-677, 2006.
- [18] T. Pichonat and B. Gauthier-Manuel, "Development of porous silicon-based miniature fuel cells," *J. Micromech. Microeng.*, vol. 15, pp. S179-S184, 2005.
- [19] C. W. Moore, *et al.*, "Microfabricated Fuel Cells with Thin-Film Silicon Dioxide Proton Exchange Membranes," *J. Electrochem. Soc.*, vol. 152, pp. A1606-A1612, 2005.

- [20] T. Pichonat, *et al.*, "A new proton-conducting porous silicon membrane for small fuel cells," *Chem. Eng. J.*, vol. 101, pp. 107-111, 2004.
- [21] E. Peled, *et al.*, "A Direct Methanol Fuel Cell Based on a Novel Low-Cost Nanoporous Proton-Conducting Membrane," *Electrochem. Solid St.*, vol. 3, pp. 525-528, 2000.
- [22] H. D. Tong, *et al.*, "Silicon Nitride Nanosieve Membrane," *Nano Lett.*, vol. 4, pp. 283-287, 2004.
- [23] A. J. Storm, *et al.*, "Fabrication of solid-state nanopores with single-nanometre precision," *Nat. Mater.*, vol. 2, pp. 537-40., Aug 2003.
- [24] W. Lee, *et al.*, "Fast fabrication of long-range ordered porous alumina membranes by hard anodization," *Nat. Mater.*, vol. 5, p. 7, 2006.
- [25] W. H. Fissell, *et al.*, "High-performance silicon nanopore hemofiltration membranes," *J. Membrane Sci.*, vol. 326, pp. 58-63, 2009.
- [26] N. Halonen, *et al.*, "Three-Dimensional Carbon Nanotube Scaffolds as Particulate Filters and Catalyst Support Membranes," *ACS Nano*, vol. 4, pp. 2003-2008, 2010.
- [27] M. Yu, *et al.*, "High Density, Vertically-Aligned Carbon Nanotube Membranes," *Nano Lett.*, vol. 9, pp. 225-229, 2009.
- [28] J. K. Holt, *et al.*, "Fast Mass Transport Through Sub-2-Nanometer Carbon Nanotubes," *Science*, vol. 312, pp. 1034-1037, May 19, 2006 2006.
- [29] M. Majumder, *et al.*, "Nanoscale hydrodynamics: Enhanced flow in carbon nanotubes," *Nature*, vol. 438, pp. 44-44, 2005.
- [30] B. J. Hinds, *et al.*, "Aligned Multiwalled Carbon Nanotube Membranes," *Science*, vol. 303, pp. 62-65, January 2, 2004 2004.

- [31] E. Ferain and R. Legras, "Pore shape control in nanoporous particle track etched membrane," *Nucl. Instrum. Meth. B*, vol. 174, pp. 116-122, 2001.
- [32] B. D. Mitchell and W. M. Deen, "Effect of concentration on the rejection coefficients of rigid macromolecules in track-etch membranes," *J. Colloid In. Sci.*, vol. 113, pp. 132-142, 1986.
- [33] Z. Siwy, *et al.*, "Ion transport through asymmetric nanopores prepared by ion track etching," *Nucl. Instrum. Meth. B*, vol. 208, pp. 143-148, 2003.
- [34] F. Martin, *et al.*, "Tailoring width of microfabricated nanochannels to solute size can be used to control diffusion kinetics," *J. Control. Rel.*, vol. 102, pp. 123-133, 2005.
- [35] P. Y. Apel, *et al.*, "Structure of polycarbonate track-etch membranes: Origin of the "paradoxical" pore shape," *J. Membrane Sci.*, vol. 282, pp. 393-400, 2006.
- [36] Whatman. *Track Etched Membranes*. Available: <http://www.whatman.com/PRODTrackEtchedMembranes.aspx>
- [37] Sterilitech. *Polycarbonate Membranes*. Available: <http://www.sterlitech.com/37625/Polycarbonate-Membranes-PCTE.html>
- [38] W. S. Opong and A. L. Zydney, "Diffusive and convective protein transport through asymmetric membranes," *AIChE J.*, vol. 37, pp. 1497-1510, 1991.
- [39] J. I. Calvo, *et al.*, "Pore Size Distributions in Microporous Membranes: I. Surface Study of Track-Etched Filters by Image Analysis," *J. Colloid In. Sci.*, vol. 175, pp. 138-150, 1995.
- [40] N. Li, *et al.*, "Conical Nanopore Membranes. Preparation and Transport Properties," *Anal. Chem.*, vol. 76, pp. 2025-2030, 2004.
- [41] C.-C. Chang, *et al.*, "A New Lower Limit for the Ultimate Breaking Strain of Carbon Nanotubes," *ACS Nano*, In Press.

- [42] Z. K. Tang, *et al.*, "Superconductivity in 4 Angstrom Single-Walled Carbon Nanotubes," *Science*, vol. 292, pp. 2462-2465, 2001.
- [43] G. Hummer, *et al.*, "Water conduction through the hydrophobic channel of a carbon nanotube," *Nature*, vol. 414, pp. 188-190, 2001.
- [44] S. Kuiper, *et al.*, "Development and applications of very high flux microfiltration membranes," *J. Membrane Sci.*, vol. 150, pp. 1-8, 1998.
- [45] T. Pichonat and B. Gauthier-Manuel, "A new process for the manufacturing of reproducible mesoporous silicon membranes," *J. Membrane Sci.*, vol. 280, pp. 494-500, 2006.
- [46] C. T. Black, *et al.*, "Highly porous silicon membrane fabrication using polymer self-assembly," in *J. Vacuum Sci. Technol. B*, 2006, pp. 3188-3191.
- [47] C. J. M. van Rijn and M. C. Elwenspoek, "Microfiltration membrane sieve with silicon micromachining for industrial and biomedical applications," in *Micro Electro Mechanical Systems, 1995, MEMS '95, Proceedings. IEEE*, 1995, p. 83.
- [48] C. Dekker, "Solid-state nanopores," *Nat. Nano.*, vol. 2, pp. 209-215, 2007.
- [49] I. Vlassiouk, *et al.*, "Direct Detection and Separation of DNA Using Nanoporous Alumina Filters," *Langmuir*, vol. 20, pp. 9913-9915, 2004.
- [50] H. B. George, *et al.*, "Ion-sculpting of nanopores in amorphous metals, semiconductors, and insulators," *Appl. Phys. Lett.*, vol. 96, p. 263111, 2010.
- [51] W. H. Fissell, *et al.*, "Differentiated Growth of Human Renal Tubule Cells on Thin-Film and Nanostructured Materials," *ASAIO J.*, vol. 52, pp. 221-227, 2006.
- [52] C. C. Striemer, "Applications of Silicon Nanostructures Compatible with Existing Manufacturing Technology," Ph.D. Thesis, Electrical and Computer Engineering, University of Rochester, Rochester, 2004.

- [53] C. C. Striemer, *et al.*, "Charge- and size-based separation of macromolecules using ultrathin silicon membranes," *Nature*, vol. 445, pp. 749-753, 2007.
- [54] T. R. Gaborski, *et al.*, "High Performance Separation of Nanoparticles with Ultrathin Porous Nanocrystalline Silicon (pnc-Si) Membranes," *ACS Nano*, vol. 4, pp. 6973-6981, 2010.
- [55] D. Z. Fang, *et al.*, "Pore Size Control of Ultrathin Silicon Membranes by Rapid Thermal Carbonization," *Nano Lett.*, vol. 10, pp. 3904-3908, 2010.
- [56] A. A. Agrawal, *et al.*, "Porous nanocrystalline silicon membranes as highly permeable and molecularly thin substrates for cell culture," *Biomaterials*, vol. 31, pp. 5408-5417, 2010.
- [57] Y. Gupta, *et al.*, "Enhanced permeability of polyaniline based nano-membranes for gas separation," *J. Membrane Sci.*, vol. 282, pp. 60-70, 2006.
- [58] R. Ishimatsu, *et al.*, "Ion-Selective Permeability of an Ultrathin Nanoporous Silicon Membrane as Probed by Scanning Electrochemical Microscopy Using Micropipet-Supported ITIES Tips," *Anal. Chem.*, vol. 82, pp. 7127-7134, 2010.
- [59] E. Kim, *et al.*, "A Structure-Permeability Relationship of Ultrathin Nanoporous Silicon Membrane: A Comparison with the Nuclear Envelope," *J. Am. Chem. Soc.*, vol. 130, pp. 4230-4231, 2008.
- [60] A. Conlisk, *et al.*, "Biomolecular Transport Through Hemofiltration Membranes," *Ann. Biomed. Eng.*, vol. 37, pp. 722-736, 2009.
- [61] W. Kern, *Handbook of Semiconductor Wafer Cleaning Technology*. Park Ridge: Noyes Publications, 1993.
- [62] L. Tonks and I. Langmuir, "A General Theory of the Plasma of an Arc," *Phys. Rev.*, vol. 34, p. 876, 1929.



- [63] B. Garrido, *et al.*, "Structural, optical, and electrical properties of nanocrystalline silicon films deposited by hydrogen plasma sputtering," *J. Vac. Sci. Technol. B*, vol. 16, pp. 1851-1859, 1998.
- [64] D. L. Young, *et al.*, "Nanostructure evolution in hydrogenated amorphous silicon during hydrogen effusion and crystallization," *Appl. Phys. Lett.*, vol. 90, p. 081923, 2007.
- [65] R. T. Howe and R. S. Muller, "Stress in polycrystalline and amorphous silicon thin films," *J. Appl. Phys.*, vol. 54, pp. 4674-4675, 1983.
- [66] X. Zhang, *et al.*, "Rapid thermal annealing of polysilicon thin films," *Sensor Actuat. A-Phys.*, vol. 7, pp. 356-364, 1998.
- [67] R. Kakkad, *et al.*, "Crystallized Si films by low-temperature rapid thermal annealing of amorphous silicon," *J. Appl. Phys.*, vol. 65, pp. 2069-2072, 1989.
- [68] P. J. Timans, "Rapid thermal processing technology for the 21st century," *Mat. Sci. Semicon. Proc.*, vol. 1, pp. 169-179, 1998.
- [69] A. Reisman, *et al.*, "The Controlled Etching of Silicon in Catalyzed Ethylenediamine-Pyrocatechol-Water Solutions," *J. Electrochem. Soc.*, vol. 126, pp. 1406-1415, 1979.
- [70] D. Z. Fang, *et al.*, "Methods for controlling the pore properties of ultra-thin nanocrystalline silicon membranes," *J. Phys. Condens. Mat.*, vol. 22, 2010.
- [71] S. Hazra, *et al.*, "Fine crystalline grain model for the determination of the morphology of ultrathin amorphous silicon films," *Appl. Phys. Lett.*, vol. 80, pp. 1159-1161, 2002.
- [72] M. Zacharias, *et al.*, "Thermal crystallization of amorphous Si/SiO<sub>2</sub> superlattices," *Appl. Phys. Lett.*, vol. 74, pp. 2614-2616, 1999.

- [73] P. Petroff, *et al.*, "Microstructure, growth, resistivity, and stresses in thin tungsten films deposited by rf sputtering," *J. Appl. Phys.*, vol. 44, pp. 2545-2554, 1973.
- [74] J. A. Thornton, "High Rate Thick Film Growth," *Annu. Rev. Mater. Sci.*, vol. 7, pp. 239-260, 1977.
- [75] S. Roorda, *et al.*, "Structural relaxation and defect annihilation in pure amorphous silicon," *Phys. Rev. B*, vol. 44, p. 3702, 1991.
- [76] M. K. Hatalis and D. W. Greve, "Large grain polycrystalline silicon by low-temperature annealing of low-pressure chemical vapor deposited amorphous silicon films," *J. Appl. Phys.*, vol. 63, pp. 2260-2266, 1988.
- [77] B.-S. So, *et al.*, "Crystallization of Amorphous Silicon Thin Films Using Self-Limiting ALD of Nickel Oxide," *Electrochem. Solid St.*, vol. 10, pp. J61-J64, 2007.
- [78] J. E. Gerbi and J. R. Abelson, "Low temperature magnetron sputter deposition of polycrystalline silicon thin films using high flux ion bombardment," *J. Appl. Phys.*, vol. 101, p. 063508, 2007.
- [79] G. Huang, *et al.*, "Crystallization of amorphous silicon thin films: The effect of rapid thermal processing pretreatment," *Vacuum*, vol. 80, pp. 415-420, 2006.
- [80] C. Spinella, *et al.*, "Crystal grain nucleation in amorphous silicon," *J. Appl. Phys.*, vol. 84, pp. 5383-5414, 1998.
- [81] R. Drosd and J. Washburn, "Some observations on the amorphous to crystalline transformation in silicon," *J. Appl. Phys.*, vol. 53, pp. 397-403, 1982.
- [82] A. Sekiguchi, *et al.*, "Void formation by thermal stress concentration at twin interfaces in Cu thin films," *Appl. Phys. Lett.*, vol. 79, pp. 1264-1266, 2001.

- [83] K. Zellama, *et al.*, "Crystallization in amorphous silicon," *J. Appl. Phys.*, vol. 50, pp. 6995-7000, 1979.
- [84] R. Sinclair, *et al.*, "Direct observation of crystallization in silicon by in situ high-resolution electron microscopy," *Ultramicroscopy*, vol. 51, pp. 41-45, 1993.
- [85] M. Suzuki, *et al.*, "Effects of rf-Bias on Properties of Sputtered Silicon Films," *Jpn. J. Appl. Phys.*, vol. 20, p. 3, 1981.
- [86] P. Revesz, *et al.*, "Epitaxial regrowth of Ar-implanted amorphous silicon," *J. Appl. Phys.*, vol. 49, pp. 5199-5206, 1978.
- [87] D. T. Danielson, *et al.*, "Surface-energy-driven dewetting theory of silicon-on-insulator agglomeration," *J. Appl. Phys.*, vol. 100, p. 083507, 2006.
- [88] L. Karlsson, *et al.*, "The influence of thermal annealing on residual stresses and mechanical properties of arc-evaporated  $\text{TiC}_x\text{N}_{1-x}$  ( $x=0, 0.15$  and  $0.45$ ) thin films," *Acta Mater.*, vol. 50, pp. 5103-5114, 2002.
- [89] K.-C. Chen, *et al.*, "Observation of Atomic Diffusion at Twin-Modified Grain Boundaries in Copper," *Science*, vol. 321, pp. 1066-1069, August 22, 2008.
- [90] S. Hazra, *et al.*, "Stress as a governing parameter to control the crystallization of amorphous silicon films by thermal annealing," *Appl. Phys. Lett.*, vol. 80, pp. 4115-4117, 2002.
- [91] R. v. d. Boomgaard and R. v. Balen, "Methods for fast morphological image transforms using bitmapped binary images," *CVGIP: Graph. Models Image Process.*, vol. 54, pp. 252-258, 1992.
- [92] J. F. Lawless, *Statistical Models and Methods for Lifetime Data*, 2nd ed.: John Wiley & Sons, Inc., 2002.

- [93] A. Mehta and A. L. Zydney, "Permeability and selectivity analysis for ultrafiltration membranes," *J. Membrane Sci.*, vol. 249, pp. 245-249, 2005.
- [94] J. A. Woollam, "Introduction to Ellipsometry," 2007 Cornell University Short Course.
- [95] C. M. Herzinger, *et al.*, "Ellipsometric determination of optical constants for silicon and thermally grown silicon dioxide via a multi-sample, multi-wavelength, multi-angle investigation," *J. Appl. Phys.*, vol. 83, pp. 3323-3336, 1998.
- [96] H. Piller, *Handbook of Optical Constants of Solids*. Orlando: Academic Press, 1985.
- [97] F. Spaepen and A. L. Shull, "Mechanical properties of thin films and multilayers," *Curr. Opin. Solid St. M.*, vol. 1, pp. 679-683, 1996.
- [98] J. J. Vlassak and W. D. Nix, "A new bulge test technique for the determination of Young's modulus and Poisson's ratio of thin films," *J. Mater. Res.*, vol. 7, p. 3242, 1992.
- [99] J. Harrop and R. M. Abdul-Karim, "Stresses and deflections in circular plates with square pitch perforations," *Nucl. Eng. Des.*, vol. 6, pp. 431-439, 1967.
- [100] A. Kovács, *et al.*, "Mechanical investigation of perforated and porous membranes for micro- and nanofilter applications," *Sensor Actuat. B-Chem.*, vol. 127, pp. 120-125, 2007.
- [101] C. van Rijn, *et al.*, "Deflection and maximum load of microfiltration membrane sieves made with silicon micromachining," *J. Microelectromech. S.*, vol. 6, pp. 48-54, 1997.
- [102] D. Maier-Schneider, *et al.*, "Variations in Young's modulus and intrinsic stress of LPCVD-polysilicon due to high-temperature annealing," *J. Micromech. Microeng.*, p. 121, 1995.

- [103] D. Bellet, *et al.*, "Nanoindentation investigation of the Young's modulus of porous silicon," *J. Appl. Phys.*, vol. 80, pp. 3772-3776, 1996.
- [104] T. Yi, *et al.*, "Microscale material testing of single crystalline silicon: process effects on surface morphology and tensile strength," *Sensor. Actuat. A-Phys*, vol. 83, pp. 172-178, 2000.
- [105] E. N. Savariar, *et al.*, "Molecular discrimination inside polymer nanotubules," *Nat. Nano.*, vol. 3, pp. 112-117, 2008.
- [106] P. Chen, *et al.*, "Atomic Layer Deposition to Fine-Tune the Surface Properties and Diameters of Fabricated Nanopores," *Nano Lett.*, vol. 4, pp. 1333-1337, 2004.
- [107] J. Salonen, *et al.*, "Stabilization of porous silicon surface by thermal decomposition of acetylene," *Appl. Surf. Sci.*, vol. 225, pp. 389-394, 2004.
- [108] L. M. Bimbo, *et al.*, "Biocompatibility of Thermally Hydrocarbonized Porous Silicon Nanoparticles and their Biodistribution in Rats," *ACS Nano*, vol. 4, pp. 3023-3032, 2010.
- [109] J. Salonen, *et al.*, "Thermal carbonization of porous silicon surface by acetylene," *J. Appl. Phys.*, vol. 91, pp. 456-461, 2002.
- [110] S. T. Lakshmikumar and P. K. Singh, "Formation of carbonized porous silicon surfaces by thermal and optically induced reaction with acetylene," *J. Appl. Phys.*, vol. 92, pp. 3413-3415, 2002.
- [111] O. Pulci, *et al.*, "Ab-initio study of the adsorption of acetylene on Si(001) surface," *Phys. Status Solidi C*, vol. 0, pp. 2997-3001, 2003.
- [112] A. M. Mazzone, "Acetylene adsorption on Si(100): A study of the role of surface steps," *Surf. Sci.*, vol. 601, pp. 218-226, 2007.
- [113] V. De Renzi, *et al.*, "Temperature dependence of acetylene adsorption and reaction on Si(1 1 1)-(7×7)," *Appl. Surf. Sci.*, vol. 184, pp. 90-95, 2001.

- [114] G. Dufour, *et al.*, "SiC formation by reaction of Si(001) with acetylene: Electronic structure and growth mode," *Phys. Rev. B*, vol. 56, p. 4266, 1997.
- [115] V. Cimalla, *et al.*, "Growth of thin  $\beta$ -SiC layers by carbonization of Si surfaces by rapid thermal processing," *Mater. Sci. Eng. B*, vol. 29, pp. 170-175, 1995.
- [116] G. Bacon, "The interlayer spacing of graphite," *Acta Crystallogr.*, vol. 4, pp. 558-561, 1951.
- [117] J. Salonen, *et al.*, "Stability Studies of Thermally-Carbonized Porous Silicon," in *Materials Research Society*, Boston, 2001, p. F14.19.
- [118] Z. Dagan, *et al.*, "An infinite-series solution for the creeping motion through an orifice of finite length," *J. Fluidic Mech. Digital Archive*, vol. 115, pp. 505-523, 1982.
- [119] M. Whitby, *et al.*, "Enhanced Fluid Flow through Nanoscale Carbon Pipes," *Nano Lett.*, vol. 8, pp. 2632-2637, 2008.
- [120] J. L. Snyder, *et al.*, "A theoretical and experimental analysis of molecular separations by diffusion through ultrathin nanoporous membranes," *J. Membrane Sci.*, In Press.
- [121] C. Dücsö, *et al.*, "Deposition of Tin Oxide into Porous Silicon by Atomic Layer Epitaxy," *J. Electrochem. Soc.*, vol. 143, p. 5, 1996.
- [122] M. A. Cameron, *et al.*, "Atomic Layer Deposition of  $\text{SiO}_2$  and  $\text{TiO}_2$  in Alumina Tubular Membranes: Pore Reduction and Effect of Surface Species on Gas Transport," *Langmuir*, vol. 16, pp. 7435-7444, 2000.
- [123] J. W. Elam, *et al.*, "Conformal Coating on Ultrahigh-Aspect-Ratio Nanopores of Anodic Alumina by Atomic Layer Deposition," *Chem. Mater.*, vol. 15, pp. 3507-3517, 2003.

- [124] A. W. Ott, *et al.*, "Modification of Porous Alumina Membranes Using  $\text{Al}_2\text{O}_3$  Atomic Layer Controlled Deposition," *Chem. Mater.*, vol. 9, pp. 707-714, 1997.
- [125] M. Utriainen, *et al.*, "Porous silicon host matrix for deposition by atomic layer epitaxy," *Thin Solid Films*, vol. 297, pp. 39-42, 1997.
- [126] G. Xiong, *et al.*, "Effect of Atomic Layer Deposition Coatings on the Surface Structure of Anodic Aluminum Oxide Membranes," *J. Phys. Chem. B*, vol. 109, pp. 14059-14063, 2005.
- [127] S.-H. Jeong, *et al.*, "Carbon nanotubes based on anodic aluminum oxide nano-template," *Carbon*, vol. 42, pp. 2073-2080, 2004.
- [128] J. S. Lee, *et al.*, "Growth of Carbon Nanotubes on Anodic Aluminum Oxide Templates: Fabrication of a Tube-in-Tube and Linearly Joined Tube," *Chem. Mater.*, vol. 13, pp. 2387-2391, 2001.
- [129] D. Gracin, *et al.*, "Study of amorphous nanocrystalline thin silicon films by grazing-incidence small-angle X-ray scattering," *J. Appl. Cryst.*, vol. 40, pp. s373-s376, 2007.
- [130] B. C. H. Steele and A. Heinzl, "Materials for fuel-cell technologies," *Nature*, vol. 414, pp. 345-352, 2001.
- [131] R. F. Service, "Shrinking Fuel Cells Promise Power in Your Pocket," *Science*, vol. 296, pp. 1222-1224, May 17, 2002.
- [132] T. M. Nenoff, "Membranes for hydrogen purification: an important step toward a hydrogen-based economy," *MRS Bull.*, vol. 31, 2006.
- [133] H. D. Tong, *et al.*, "Microsieve supporting palladium-silver alloy membrane and application to hydrogen separation," *J. Microelectromech. S.*, vol. 14, pp. 113-124, 2005.

- [134] J. Dong, *et al.*, "Microporous inorganic membranes for high temperature hydrogen purification," *J. Appl. Phys.*, vol. 104, pp. 121301-17, 2008.
- [135] R. O'Hayre, *et al.*, *Fuel Cell Fundamentals*: Wiley, 2005.
- [136] J. Stadlmann, *et al.*, "Analysis of immunoglobulin glycosylation by LC-ESI-MS of glycopeptides and oligosaccharides," *Proteomics*, vol. 8, pp. 2858-2871, 2008.
- [137] Y. Mechref and M. V. Novotny, "Structural Investigations of Glycoconjugates at High Sensitivity," *Chem Rev.*, vol. 102, pp. 321-370, 2002.
- [138] K. Stulik, *et al.*, "Some potentialities and drawbacks of contemporary size-exclusion chromatography," *J. Biochem. Biophys. Methods*, vol. 56, pp. 1-14, 2003.
- [139] H. Geyer and R. Geyer, "Strategies for analysis of glycoprotein glycosylation," *BBA-Proteins Proteom*, vol. 1764, pp. 1853-1869, 2006.
- [140] P.-C. Wang, *et al.*, "Integration of polymeric membranes with microfluidic networks for bioanalytical applications," *Electrophoresis*, vol. 22, pp. 3857-3867, 2001.
- [141] Y. Jiang, *et al.*, "Integrated Plastic Microfluidic Devices with ESI-MS for Drug Screening and Residue Analysis," *Anal. Chem.*, vol. 73, pp. 2048-2053, 2001.
- [142] T. Kuo, *et al.*, "Gateable Nanofluidic Interconnects for Multilayered Microfluidic Separation Systems," *Anal. Chem.*, vol. 75, pp. 1861-1867, 2003.
- [143] J. C. McDonald and G. M. Whitesides, "Poly(dimethylsiloxane) as a Material for Fabricating Microfluidic Devices," *Acc. Chem. Res.*, vol. 35, pp. 491-499, 2002.
- [144] R. Pantoja, *et al.*, "Silicon chip-based patch-clamp electrodes integrated with PDMS microfluidics," *Biosens. Bioelectron.*, vol. 20, pp. 509-517, 2004.



- [145] S. Park, *et al.*, "On-chip coupling of electrochemical pumps and an SU-8 tip for electrospray ionization mass spectrometry," *Biomed. Microdevices*, vol. 10, p. 891, 2008.